



저작자표시-비영리-변경금지 2.0 대한민국

이용자는 아래의 조건을 따르는 경우에 한하여 자유롭게

- 이 저작물을 복제, 배포, 전송, 전시, 공연 및 방송할 수 있습니다.

다음과 같은 조건을 따라야 합니다:



저작자표시. 귀하는 원저작자를 표시하여야 합니다.



비영리. 귀하는 이 저작물을 영리 목적으로 이용할 수 없습니다.



변경금지. 귀하는 이 저작물을 개작, 변형 또는 가공할 수 없습니다.

- 귀하는, 이 저작물의 재이용이나 배포의 경우, 이 저작물에 적용된 이용허락조건을 명확하게 나타내어야 합니다.
- 저작권자로부터 별도의 허가를 받으면 이러한 조건들은 적용되지 않습니다.

저작권법에 따른 이용자의 권리는 위의 내용에 의하여 영향을 받지 않습니다.

이것은 [이용허락규약\(Legal Code\)](#)을 이해하기 쉽게 요약한 것입니다.

[Disclaimer](#)

Ph.D. DISSERTATION

**Study on the device performance and
photo-bias stability for the solution processed
Zn-Sn-O field effect transistors**

by

Yoon Jang Kim

August 2014

**Department of Materials Science and Engineering
College of Engineering
Seoul National University**

**Study on the device performance and
photo-bias stability for the solution processed
Zn-Sn-O field effect transistors**

Advisor : Prof. Hyeong Joon Kim

**By
Yoon Jang Kim**

**A thesis submitted to the Graduate Faculty of Seoul National
University in partial fulfillment of the requirements for the
Degree of Doctor of Philosophy
Department of Materials Science and Engineering**

August 2014

**Approved
by**

Chairman of Advisory Committee : Cheol Seong Hwang

Vice-chairman of Advisory Committee : Hyeong Joon Kim

Advisory Committee : Ho Won Jang

Advisory Committee : Myung Soo Huh

Advisory Committee : Jae Kyeong Jeong

Abstract

Zinc-based oxide thin film transistors (TFTs) have attracted considerable attention as a switching device for active matrix (AM) liquid crystal displays (LCDs) and organic light-emitting diodes (OLEDs) owing to their high mobility, good transparency to visible light, and low temperature capability compared to amorphous Si TFTs. Recently, the solution process has emerged as a viable alternative to the vacuum based process due to its process simplicity, low cost, and potentially high throughput. However, the device reliability under the gate bias stress and light stress still remains a critical issue for the implementation of oxide TFTs to the commercial electronic products and very little is known about the effect of annealing temperature and Sn content on the photo-bias stability of solution processed zinc-tin oxide (ZTO) TFTs.

This dissertation discusses the effect of annealing temperature and Sn concentration on the various physical properties of the solution processed ZTO films, as well as the accompanying transport properties and photo-bias instability of solution-processed ZTO TFTs.

At first, high performance zinc-tin oxide TFTs was fabricated using solution process. The density and purity of the resulting ZTO channel layer increased with increasing annealing temperature, whereas the oxygen vacancy defect density

decreased. As a result, the device performance of solution processed ZTO TFTs was improved at higher annealing temperature. The instability of V_{th} values of the ZTO TFTs under NBS and NBIS condition was suppressed with increasing annealing temperature. To better understand the charge trapping mechanism, the dynamics of V_{th} shift with NBS and NBIS time for all ZTO TFTs was analyzed on the basis of the stretched exponential relaxation. The negative V_{th} shift for each transistor was accelerated under NBIS conditions compared to NBS, which resulted in a higher dispersion parameter and smaller relaxation time for NBIS degradation. The relaxation time for NBS and NBIS instability increased with increasing annealing temperature, which is discussed on the basis of the transition mechanism of oxygen vacancy defects. This suggests that the purification and densification of the solution-processed ZTO channel layer are critical factors for high performance oxide TFTs with excellent photo-bias stability.

The structural, chemical and electrical properties of solution-processed $(\text{Zn},\text{Sn})\text{O}_3$ (ZTO) films with various $\text{Sn}/[\text{Zn}+\text{Sn}]$ ratios for potential applications to large-area flat panel displays were investigated. ZTO films with a Zn-rich composition had a polycrystalline wurtzite structure, and the excess Sn was found to be a shallow donor. On the other hand, the Sn-rich ZTO films exhibited a rutile structure, where the Zn atom was speculated to replace the Sn site, thereby acting as an acceptor. In the intermediate composition regions ($\text{Sn}/[\text{Zn}+\text{Sn}]$ ratio from 0.28 to

0.48), the ZTO films had an amorphous structure, even after annealing at 450 °C.

Finally, the electrical transport properties and photo-bias stability of ZTO TFTs were also examined according to the Sn/[Zn+Sn] ratio. The optimal transport property of ZTO TFTs was observed for the device with an amorphous structure at a Sn/[Zn+Sn] ratio of 0.48. In contrast, the device performance for the ZTO TFTs with either a higher or lower Sn-concentration suffered from low mobility and a high off-state current, respectively. The photo-electrical stress measurements showed that the photo-bias stability of the ZTO TFTs was improved substantially when the ZTO semiconducting films had a lower oxygen vacancy concentration and an amorphous structure. This suggests that the migration of photo-induced V_{O}^{2+} defects are also critical factors for determining the photo-bias stability of ZTO TFTs, and the amorphous phase with optimal Sn-concentration is desirable for securing the photo-bias stability of ZTO TFTs.

Keywords : Solution process, Zinc Tin Oxide (ZTO), thin film transistors (TFTs), annealing temperature, cation composition, photo-bias stability, Negative bias illumination stability (NBIS)

Student ID : 2010-30959

Yoon Jang Kim

Table of Contents

Abstract	i
Table of Contents	iv
List of Tables	vii
List of Figures	viii
1. Introduction	1
1.1 Overview.....	1
2. Literature Review	7
2.1 Thin film transistors.....	7
2.1.1 Device structure.....	7
2.1.2 Operation of thin film transistors.....	10
2.1.3 Thin film transistor characterization.....	13
2.2 Solution process.....	17
2.2.1 Sol-Gel process.....	17
2.2.2 Thin-film deposition methods.....	21
2.3 Metal oxide semiconductor.....	25
2.3.1 Electronic structure and conduction mechanism.....	25
2.3.2 Amorphous oxide thin film transistor.....	32

2.3.3 Solution processed amorphous oxide thin film transistor.....	40
2.4 Instability of oxide thin film transistor.....	47
2.4.1 Positive bias stress.....	47
2.4.2 Negative bias stress.....	52
3. Experiments and Analyses.....	60
3.1 Experimental procedure.....	60
3.2 Analysis methods.....	62
3.3 Electrical and reliability measurements.....	64
4. Results and Discussions.....	66
4.1 The effect of the annealing temperature on the device performance and photo-bias stability.....	66
4.1.1 Introduction.....	66
4.1.2 Experimental procedure.....	69
4.1.3 Structural and chemical properties of ZTO thin films.....	70
4.1.4 Electrical properties of ZTO TFTs.....	83
4.1.5 NBS and NBIS instability of ZTO TFTs	87
4.1.6 Summary.....	98

4.2 The impact of the cation composition on the electrical performance and photo-bias stability.....	100
4.2.1 Introduction.....	100
4.2.2 Experimental procedure	104
4.2.3 Structural and chemical properties of ZTO thin films.....	105
4.2.4 Electrical properties of ZTO TFTs.....	114
4.2.5 NBIS instability of ZTO TFTs.....	124
4.2.6 Summary.....	131
5. Conclusions.....	133
Bibliography.....	136
List of publications.....	148
Abstract (in Korean)	152
Acknowledgement (감사의 글).....	155

List of Tables

Table 1.1 Typical properties of various *n*-type transparent oxide films.

Table 4.1. Roughness, density, thickness and cation composition of a-ZTO thin films as a function of the annealing temperature.

Table 4.2. XPS O 1s result for the annealed ZTO thin films.

Table 4.3. Comparison of the device parameters including μ_{FE} , SS , V_{th} , $I_{on/off}$, $D_{it,max}$, and $N_{ss,max}$ of the various ZTO TFTs.

Table 4.4. Comparison of the relaxation time (τ) and dispersion parameter (β) at room temperature for the various ZTO TFTs.

Table 4.5. O 1s peaks deconvoluted from the XP spectra of the various ZTO films with different Sn fractions.

Table 4.6. Device parameters including μ_{FE} , SS , V_{th} , I_{on}/I_{off} , $D_{it,max}$, $N_{ss,max}$ and ΔV_{th} of the various ZTO TFTs.

List of Figures

Fig. 2.1. Schematics of the most conventional TFT structures.

Fig. 2.2. Energy band diagrams as viewed through the gate for several biasing conditions: (a) equilibrium, (b) depletion ($V_{GS} < 0$ V), and (c) accumulation ($V_{GS} > 0$ V).

Fig. 2.3. Typical a) output and b) transfer characteristics of a n-type oxide TFT.

Fig. 2.4. Schematic diagram of (a) spin, (b) dip, and (c) spray coating.

Fig. 2.5. Schematic electronic structures of silicon and ionic oxide semiconductors. Bandgap formation mechanisms in (a) covalent and (b,c) ionic semiconductors.

Fig. 2.6. Schematic orbital structure of the conduction-band minimum in Si and in an ionic oxide semiconductor.

Fig. 2.7. Temperature dependences of Hall mobility, (μ_{Hall}) and carrier concentration, (N_c) for a-IGZO.

Fig. 2.8. Schematic illustration of conduction and electronic structure around conduction band edge. An arrow is an electron conduction path. (left bottom) potential distribution cross-section. E_{th} and E_F denote threshold energy at above which carrier moves freely and Fermi level, respectively. (Right) Density of state.

Fig. 2.9. (a) The crystal structure of c-Zn₂SnO₄. The amorphous structure of (b) a-SZTO and (c) a-ZTO.

Fig. 2.10. Device structure of colloidal-based ZnO TFT.

Fig. 2.11. Displayed image of 2.2 inch QQVGA mono AMOLED and panel specification.

Fig. 2.12. Linear transfer I_{DS} - V_{GS} curve of a-IGZO TFTs as a function of stress time (t_{ST}). The inset shows the bias-stress-induced shift of $\log(I_{DS})$ - V_{GS} curve. The sweep was done at V_{DS} = 0.5 V in both curves.

Fig. 2.13. (a) Schematic showing the electric-field-induced adsorption of oxygen molecules from the ambient atmosphere under the application of PGVS. (b) Schematic showing the electric-field-induced desorption of water molecules into the ambient atmosphere under positive V_{GS} stress.

Fig. 2.14. Changes in the I_D - V_G characteristics of ZnO TFTs (a) under dark PBS conditions, (b) PBIS conditions with a photo-intensity of 1.0 mW/cm², (c) dark NBS condition, and (d) NBIS condition with photo-intensity of 1 mW/cm².

Fig. 2.15. Plausible energy band diagram of the MIS structure under (a) PBIS and (b) NBIS conditions.

Fig. 2.16. Schematic band diagram, which is based on trapping or/and injection of a photo induced hole carrier.

Fig. 2.17. The creation $V_{O^{2+}}$ state and involved n-type doping mechanism.

Fig. 2.18. Schematic energy band diagram showing the photodesorption of oxygen molecules into the ambient atmosphere for the unpassivated device under the application of NBS.

Fig. 3.1. Flow chart of solution processed ZTO thin film and TFT.

Fig. 3.2. Schematic diagram of the illumination system.

Fig. 4.1. TGA of the ZTO precursor solution at $5\text{ }^{\circ}\text{C min}^{-1}$ heating rate in air.

Fig. 4.2. XRD patterns of the ZTO thin films annealed at various Temperatures.

Fig. 4.3. High resolution TEM images of ZTO thin films annealed at (a) 300 and (b) $600\text{ }^{\circ}\text{C}$.

Fig. 4.4. AFM images of the ZTO annealed at (a) 300, (b) 400, (c) 500, and (d) $600\text{ }^{\circ}\text{C}$.

Fig. 4.5. XRR data for the ZTO films prepared at various annealing temperatures.

Fig. 4.6. O $1s$ XPS spectra of the ZTO films annealed at (a) 300, (b) 400, (c) 500, and (d) $600\text{ }^{\circ}\text{C}$.

Fig. 4.7. Cl $2p$ XPS spectra of the ZTO films at various annealing temperatures.

Fig. 4.8. Representative transfer characteristics of the ZTO TFTs annealed at various temperatures.

Fig. 4.9. Evolution of the transfer characteristics of ZTO annealed at (a) 300, (b) 400, (c) 500, and (d) $600\text{ }^{\circ}\text{C}$ as a function of the dark NBS time.

Fig. 4.10. Dark NBS time dependence of ΔV_{th} for the various ZTO TFTs. The measured data was fitted to a stretched-exponential equation with fitting parameter of τ and β .

Fig. 4.11. Evolution of the transfer characteristics of ZTO annealed at (a) 300, (b) 400, (c) 500, and (d) 600 °C as a function of the NBIS time.

Fig. 4.12. NBIS time dependence of ΔV_{th} for the various ZTO TFTs.

Fig. 4.13. XRD patterns of the ZTO thin films as a function of the incorporated Sn-concentration.

Fig. 4.14. (Upper panels) Cross-section TEM images of ZTO thin films with a Sn/[Zn+Sn] ratio of (a) 0.16, (b) 0.48 and (c) 0.77. Selected area diffraction pattern of each film is inserted in the inset in Fig. 4.14. (Lower panels) High resolution image of ZTO films with a Sn/[Zn+Sn] of (d) 0.16, (e) 0.48 and (f) 0.77.

Fig. 4.15. O $1s$ XP spectra and their deconvolution results of the ZTO films with a Sn/[Zn+Sn] ratio of (a) 0.16, (b) 0.28, (c) 0.39, (d) 0.48, (e) 0.59 and (f) 0.66. Inset in (a) shows the variation of V_O peak ratio as a function of Sn/[Zn+Sn].

Fig. 4.16. The variation of V_O peak ratio as a function of Sn/[Zn+Sn].

Fig. 4.17. Variation of the carrier density for the ZTO films as a function of the Sn-concentration.

Fig. 4.18. Representative transfer characteristics of the ZTO TFTs for the different Sn-concentrations.

Fig. 4.19. Output characteristics of the ZTO TFTs at a Sn/[Zn+Sn] ratio of (a) 0.16, (b) 0.28, (c) 0.39, (d) 0.48, (e) 0.59 and (f) 0.66.

Fig. 4.20. Evolution of the transfer characteristics of ZTO TFTs with a Sn/[Zn+Sn] ratio of (a) 0.16, (b) 0.28, (c) 0.39, (d) 0.48, (e) 0.59 and (f) 0.66 as a function of the NBIS time.

Fig. 4.21. Variation in V_{th} as a function of the NBIS time and (h) as a function of the incorporated Sn-concentration.

Fig. 4.22. Variation in V_{th} as a function of the incorporated Sn-concentration.

1. Introduction

1.1. Overview

Thin film transistors (TFTs) have been used as switching device in display technologies such as liquid crystal displays (LCDs) and organic light emitting diodes (OLEDs). For example, the brightness of screen or monitor is controlled by TFTs in unit pixel of display devices. Since the mass production of LCDs started in early 1990, the flat-panel display technology has been developed significantly and continued its rapid growth. The coming of huge success of these technologies was attributed to the introduction of hydrogenated amorphous silicon (a-Si:H). The a-Si:H was the most compatible material for the application of TFTs as switching devices due to the low-cost process, excellent uniformity in large area, and high I_{on}/I_{off} ratios of 10^6 . On the other hand, a-Si:H possess critical issues, such as low carrier mobility $\sim 1 \text{ cm}^2/\text{Vs}$, its relatively poor stability under bias stressing, and light sensitivity, which hinder to drive the next generation high performance LCDs and OLEDs backplanes with a large size, high resolution, and high frame rate. Polycrystalline silicon (poly-Si) also has been used as the channel material of backplane TFTs in LCDs and OLEDs. The poly-Si TFTs exhibited orders of magnitude larger mobilities than that of a-Si:H TFTs, which allowed their

application not only as switching devices but also as driver circuitry. However, p-Si TFTs require high temperature fabrication process and expensive crystallization methods, such as excimer laser annealing (ELA). The p-Si TFTs also suffer from the uniformity of device performance due to the grain boundary effects. Therefore, the lack of uniformity in large area and expensive processing cost are not suitable for applications with large size and flexibility. The low performance of a-Si:H TFTs and the high manufacturing costs of p-Si TFTs make it difficult to satisfy the requirement of display industry.

In this regard, amorphous oxide TFTs provide as viable alternative for the high performance display devices because of its high mobility, low temperature capability, good transparency to visible light, and relatively low fabrication cost. In 2004, Nomura *et al.* fabricated a new class of amorphous oxide semiconductors based on InGaZnO (IGZO) [1]. The a-IGZO TFTs exhibited high mobilities of $8.3 \text{ cm}^2/\text{Vs}$, threshold voltage of 1-2 V and I_{on}/I_{off} ratio of 10^3 even though a-IGZO films were deposited at room temperature. Since the publication by Nomura *et al.*, amorphous multi-component oxide TFTs have been investigated intensively as channel layer in TFTs, such as ZnSnO [2], InZnO [3], and InZnSnO [4]. Amorphous multi-component oxides composed of heavy metal cations with $(n-1)d^{10}ns^0$ ($n \geq 4$) electronic configuration. The spatial spreads of the vacant s-orbitals of cations are so large that they overlap with each other, creating a continuous

carrier conduction path. Since the s-orbitals are isotropic in shape, the magnitude of the overlap is insensitive to the bond angles, which is the origin of having high mobility even in amorphous phase [5]. As the result, amorphous oxide semiconductor are considered much more favorable for high-end display devices than other competitor materials. The typical properties of various transparent oxide films were listed in Table 1.1 [6].

Although several proto type display devices with a-IGZO TFTs are presented and close to commercialization due to its high mobility, low temperature operation, and good transparency, several concerns are appeared. In and Ga are one of the scarce and expensive material in the earth crust and the resulting high price is an obstacle to its widespread utilization in mass-produced printed electronics [7]. In this respect, ZnSnO (ZTO) has been researched intensively as a desirable active layer owing to its elemental abundance and low cost.

There has also been interest in novel deposition approaches for large area thin film semiconductor devices. Most amorphous oxide semiconductor is fabricated by vacuum based techniques, such as rf sputter, pulsed laser deposition (PLD), and atomic layer deposition (ALD). However, the operation and maintenance of physical vacuum based techniques is generally expensive, and these systems have some inherent disadvantages. In other ward, as displays increase in size, a possible upscaling of those chambers, to process larger substrates, becomes increasingly

expensive. This leads to the developing of new and inexpensive technologies and solution process can be a viable alternative to fabricate TFTs in order to achieve low-cost production for large area. In addition, direct-writing capabilities of the solution process enables the realization of the low-cost printed electronics for flexible displays.

In this dissertation, high performance solution-processed ZTO TFTs were fabricated using carbon-free ZnCl_2 and SnCl_2 precursors. The effect of the annealing temperature on the device performance, dark negative bias stress (NBS), and negative bias illumination stress (NBIS) instability was examined based on the structural and chemical characterization of the ZTO films. The relaxation time of V_{th} shift for various ZTO TFTs under NBS and NBIS conditions were also extracted by fitting to a stretched exponential equation, which was found to be strongly dependent on the structural and chemical properties of the soluble-processed ZTO films.

In addition, the effects of the Sn-concentration on the various physical properties of the ZTO films, as well as the accompanying transport properties and photo-bias instability of solution-processed ZTO TFTs were examined. The structural and chemical properties of ZTO films were strongly dependent on the Sn-concentration. The ZTO films with Zn-rich and Sn-rich compositions crystallized with the wurtzite and rutile structures, respectively, after annealing at 450 °C for 1

hr in air, whereas the ZTO films with a Sn/Zn ratio ~ 1 maintained the amorphous structure. The Sn in a ZTO film with a Zn-rich composition was identified as a carrier generator (donor center). In contrast, the Zn atoms in the rutile-structured ZTO films with a Sn-rich composition work as an acceptor center. The optimal photo-bias stability of the ZTO TFTs was determined from the microstructure of the ZTO film rather than from the chemical defects of ZTO films.

The organization of this dissertation is as follows. Chapter 2 gives the description of thin film TFT structure, operation and characterization. The basic theory and deposition methodology of solution process are introduced. The pertinent literature related to metal oxide semiconductors including electronic structure and conduction mechanism is reviewed. The basic mechanism of positive bias stress and negative bias stress is discussed. Chapter 3 provides a description of solution process, analysis method employed in this thesis. Chapter 4 presents the effect of the annealing temperature on the device performance and photo-bias instability based on the structural and chemical characterization of the ZTO films. And the effects of the Sn-concentration on the various physical properties of the ZTO films, transport properties and photo-bias instability of solution-processed ZTO TFTs were examined. Finally, Chapter 5 provides the conclusion of this thesis.

Table 1.1 Typical properties of various *n*-type transparent oxide films.

Mat.	E_g^{opt} (eV)	T (%)	μ_{Hall} (cm ² /Vs)	N_d (cm ⁻³)	ρ (Ω cm)
CdO	2.2-2.6	75	220	10 ¹⁹ - 10 ²¹	2×10 ⁻³
Cd ₂ SnO ₄	2.9-3.1	90	35-60	~7×10 ²¹	~2×10 ⁻⁴
In ₂ O ₃	3.7	80-90	10-40	≤ 10 ²¹	≥ 10 ⁻⁴
InGaO ₃	3.3	90	10	10 ²⁰	2.5×10 ⁻³
InGaZnO ₄	3.5	80-90	24	~10 ²⁰	2×10 ⁻³
SnO ₂	3.6	80-90	5-30	≤ 10 ²⁰	≥ 10 ⁻³
ZnO	3.2-3.3	80-90	5-50	≤ 10 ²¹	≥ 10 ⁻⁴
Zn ₂ In ₂ O ₅	2.9	80	12-20	~5×10 ²⁰	4×10 ⁻³
ZnSnO ₃	3.5	80	7-12	10 ²⁰	5×10 ⁻³
Zn ₂ SnO ₄	3.3-3.9	90	12-26	6×10 ¹⁸	~5×10 ⁻²

※ E_g^{opt} : optical band-gap, χ : electron affinity, μ_{Hall} : Hall mobility, N_d : carrier concentration, ρ : resistivity

2. Literature Review

2.1. Thin film transistor

2.1.1. Device structure

Thin film transistor basically consists of gate electrode, a dielectric layer, semiconductor layer, and source-drain (S/D) layer. Figure 2.1. shows the basic four type structure of the thin film transistor. The structure of thin film transistor can be classified with top-gate and bottom-gate structure according to the relative position of the gate electrode. In the bottom-gate TFT structure, the gate electrode is positioned on the substrate. The gate insulator and semiconductor layer are placed sequentially on the gate. In contrast, the top-gate TFT structure has gate layer on the top of structure and the gate insulator and semiconductor layer are placed beneath the gate layer. Depending on the position of S/D, the structure can be categorized as staggered or co-planner. In staggered structure, the source-drain are placed on opposite of the semiconductor. On the other hand, the co-planner TFT structure has the source-drain on the same side of the semiconductor. A staggered structure TFT with bottom-gate usually have easier processing and enhanced electrical properties especially for a-Si:H TFT device. The bottom gate also plays to

screen a light from the back light unit. Because a-Si:H is sensitive to the lights, this configuration is widely used for the fabrication of TFTs with a-Si:H as a channel layer in the display device. In contrast, a coplanar top-gate structure is generally fabricated for poly-Si TFTs. The poly-Si TFTs should be crystallized using following process at high temperature. The co-planner top-gate configuration can be shield the degradation of device properties resulted from the crystallization process [8].

In this study, the bottom gate structure was used for fabrication of solution processed Zinc Tin oxide TFTs. Because a spin coating method is adapted to fabricate ZTO channel layer, the S/D layer can hinder the fabrication of thin film layer.

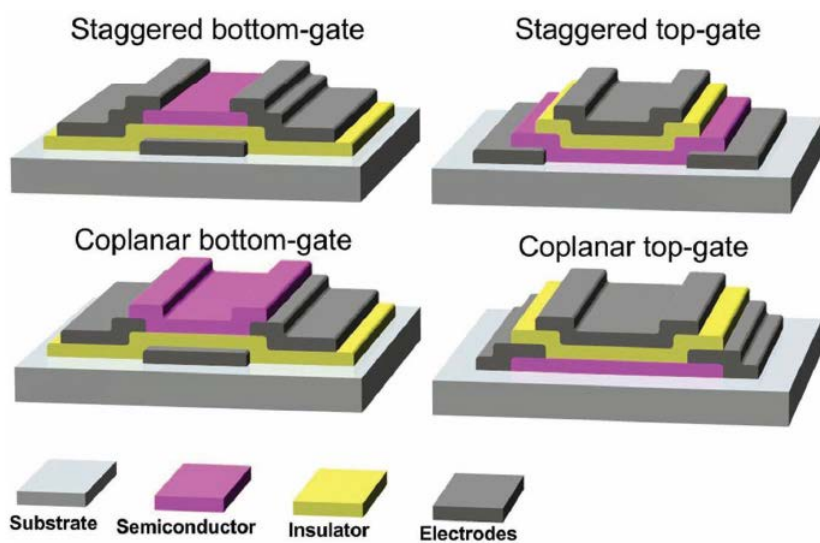


Fig. 2.1. Schematics of the most conventional TFT structures [8].

2.1.2 Operation of thin-film transistors

The ZTO TFTs is ideal n-type mode device, which means an electron accumulation layer is formed by appropriate bias. Figure 2.2 shows energy band diagrams of accumulation-mode TFT [9]. The energy band diagrams are represented as a change of field of gate voltage and charge carriers at the interface of the channel and insulator layer.

1) Equilibrium Mode

Figure 2.2 (a) shows the device at equilibrium. In equilibrium mode, the gate and S/D is applied to 0 V. When gate voltage of 0 V is applied, the conductance of the semiconductor is significantly low. There is no flow of charges through the channel layer because of no difference of the Fermi level (E_F) between the semiconductor and metal.

2) Depletion Mode

When a negative bias ($V_{GS} < 0$) is applied to the gate (Figure 2.2 (b)), E_F in the metal is raised compared to E_F in semiconductor leading the band to band upwards. The concentration of electron is decreased and a depletion region is created in the vicinity of semiconductor/insulator interface. This is called the depletion mode. As

the negative gate bias increases, the semiconductor surface can bend up more causing the increase of hole concentration at the surface. However, the transport of holes is negligible due to a huge sub-gap density of states ($10^{20}/\text{cm}^3$) near the valence band of Zinc based oxide film [10].

3) Accumulation Mode

When a positive bias ($V_{GS} > 0$) is applied to the gate (Figure 2.3 (c)), E_F in the metal is lowered compared to E_F in semiconductor and cause the band to band downwards. The negatively charged electrons are drawn towards the semiconductor/ insulator interface and accumulated at the semiconductor/ insulator interface resulted in the increase of electron concentration and formation of the channel layer near the semiconductor/insulator interface. This is the accumulation mode of the n-type TFT. If the drain to source voltage (V_{DS}) is increased from 0 V, electrons are injected from the source electrode into the channel and current increase linearly with increase.

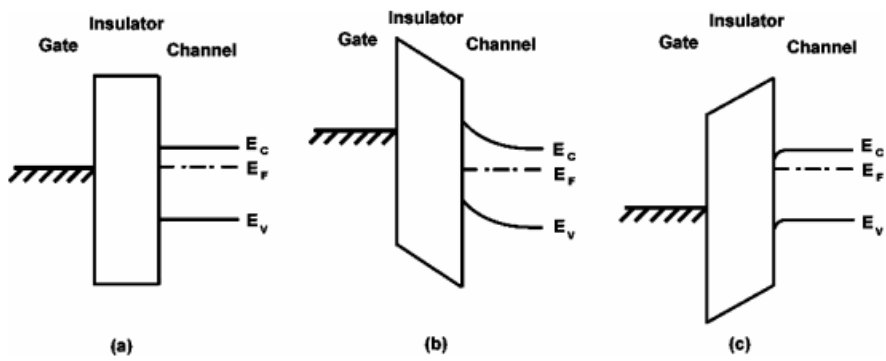


Fig. 2.2. Energy band diagrams as viewed through the gate for several biasing conditions: (a) equilibrium, (b) depletion ($V_{GS} < 0$ V), and (c) accumulation ($V_{GS} > 0$ V) [9].

2.1.3 Thin film transistor characterization

The analysis of TFTs devices characterization typically is carried out by using MOSFET drain current equations. Several of the TFT parameters including drain current on/off ratio, channel mobility (μ), turn-on voltage (V_{ON}) and threshold voltage (V_{th}), subthreshold swing (S) can be obtained by log I_{DS} - V_{GS} .

1) Channel mobility (μ)

The channel mobility is the key parameter which represents the characteristics of device performance. It can be defined the average mobility of carrier transport in a channel layer and affected by several scattering mechanisms, such as lattice vibrations, ionized impurities, grain boundaries and other structural defects [11]. The most commonly used method for determining the channel mobility is MOSFET drain current equations.

The equations for drain current in the linear regions is given as,

$$I_{D,linear} = \frac{W}{L} \mu_{eff} C_{ox} (V_G - V_T) V_{DS} \quad \text{at } V_D < V_G - V_T \quad (\text{Eq. 2.1})$$

$$g_m = \left. \frac{\partial I_{DS}}{\partial V_{GS}} \right|_{V_{DS}=const.} = \frac{W}{L} \mu_{eff} C_{ox} V_{DS} \quad (\text{Eq. 2.2})$$

The field effect mobility (μ_{FE} or μ_{eff}) is then given by,

$$\mu_{eff} = \frac{Lg_m}{WC_{ox}V_{DS}} \quad (\text{Eq. 2.3})$$

The equations for the drain current in saturation regions is given as,

$$I_{D,sat} = \frac{W\mu_{eff}C_{ox}}{2L}(V_G - V_T)^2 \quad \text{at } V_D > V_G - V_T \quad (\text{Eq. 2.4})$$

Saturation mobility (μ_{SAT}) is extracted using following equation,

$$\mu_{sat} = \frac{2Lm^2}{WC_{ox}} \quad \text{at } m : \text{slope } \sqrt{I_{D,sat}} - (V_G - V_T) \quad (\text{Eq. 2.5})$$

Where L is the channel length, W is the width, and C_{ox} is the gate capacitance per unit area.

2) subthreshold swing (SS)

The subthreshold swing, SS are estimated from a log plot of the transfer characteristics. SS is the inverse of the maximum slope in the transfer characteristics. A small value of SS is desirable because it shows how fast TFTs

turn on from off state.

$$S = \frac{1}{\text{slope}} = \frac{V_2 - V_1}{\log(I_{DS2} - I_{DS1})} \quad (\text{Eq. 2.6})$$

3) Drain current I_{on}/I_{off} ratio

This is a parameter for switching device and defined as the ratio between the highest measured current to the lowest measured current. Figure 2.3 shows the transfer and output characteristics of ZTO based-TFTs using in this study.

4) Turn-on voltage (V_{ON}) and threshold voltage (V_{th})

Turn-on voltage and threshold voltage (V_{th}) has different physical meaning and which can be defined using several methodologies [12]. In this study, V_{on}/V_{th} were defined as the gate voltage which induces a drain current of $L/W \times 10$ nA at $V_{DS} = 10.1$ V [13]. The extraction of V_{on}/V_{th} in this way is frequently used because the analog driver in the actual unit pixel of AMOLED panel is loaded between 1 μ A and 1 nA. Here, the roughly 1 μ A and 1 nA are needed to embody the full-on and black gray scale for AMOLED devices, respectively. Although this type of V_{th} definition does not have a unique physical meaning, the gate voltage to induce a drain current of 10 nA can be a very useful guideline for the panel design as well as the process control.

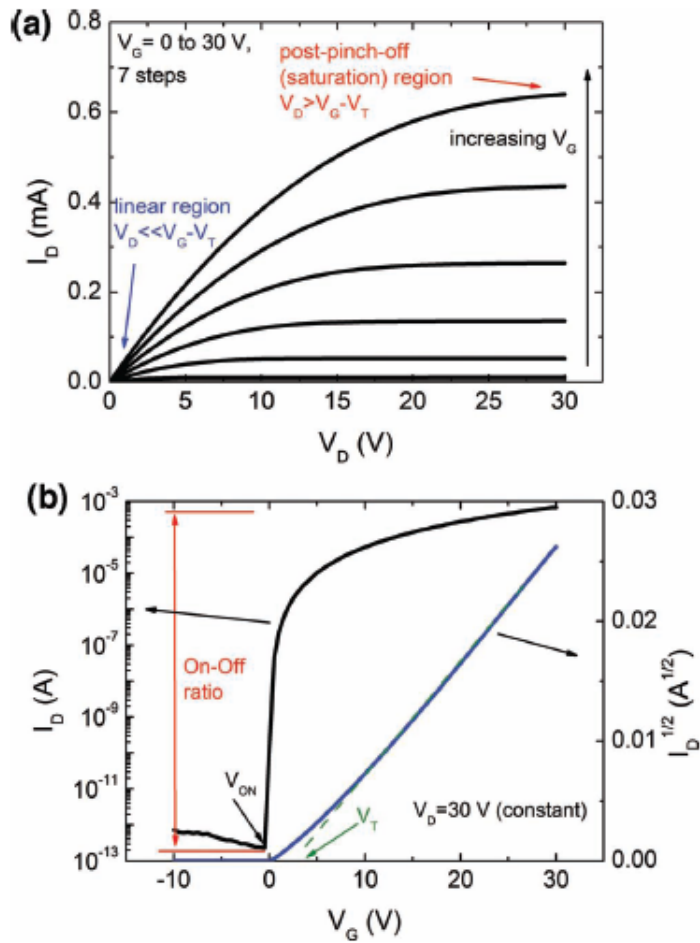


Fig. 2.3. Typical a) output and b) transfer characteristics of a n-type oxide TFT [8].

2.2. Solution process

2.2.1. Sol-Gel process

2.2.1.1. Hydrolysis

Sol-gel chemistry is based on inorganic polymerization reactions. Sol-gel processing involves the use of molecular precursors, mainly alkoxides as starting materials. In general, the alkoxides are dissolved in alcohol and hydrolyzed with H₂O in presence of an acid or basic catalyst [14]. The reaction is called hydrolysis, because a hydroxyl ion becomes attached to the metal atom, written as follows [15]:



Metal alkoxides are in general very reactive due to the presence of highly electronegative OR groups (hard- π donors) that stabilize metal in its highest oxidation state and render metal very susceptible to nucleophilic attack. The lower electronegativity of transition metals causes them to be more electrophilic and thus less stable toward hydrolysis, condensation and other nucleophilic reactions. Controlling the conditions can be difficult but successful control of the reaction

conditions has the potential to produce materials of consistent size, shape and structure [15]. The nucleophilic substitution reaction that occurs during hydrolysis can be described as follows [16]:

1. Nucleophilic addition of the H_2O onto the positively charged metal atom.
2. Proton transfer, within the transition state from the entering molecule to the leaving alkoxy group.

2.2.1.2. Condensation

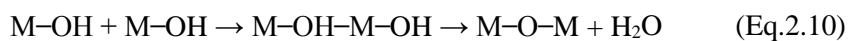
Condensation reactions involving the hydroxyl ligands produce polymers composed of M-O-M or M-OH-M bonds plus, in most cases, the by-products water or alcohol [17]. Condensation is also a complex process and can occur as soon as hydroxo groups are generated. Depending on experimental conditions, three competitive mechanisms have to be considered namely: alcoxolation, oxolation and olation [18].

1) Alcoxolation is a reaction by which a bridging oxo group is formed through the elimination of an alcohol molecule. The mechanism is basically the same as for hydrolysis with M replacing H in the entering group



Consequently, the thermodynamics and kinetics of this reaction are governed by the same parameters as for hydrolysis.

2) Oxolation leads to the formation of oxo bridge M-O-M between two metal cation M. Such a condensation process is observed when no aquo ligand is available in the coordination sphere of the metal, followed the same mechanism as alcoxolation, but the R group of the leaving species is a proton



The leaving group is thus a water molecule.

3) Olation can occur when the full coordination of the metal atom is not satisfied in the alkoxide (N-z~O). In this case bridging hydroxo groups can be formed through the elimination of a solvent molecule. This latter can be either H₂O or ROH depending on the water concentration in the medium.

A macromolecular oxide network is then obtained through hydrolysis and condensation reactions. These reactions play a significant role in the final gel molecular structure. The kind and amount of catalyst used, the amount of water and the nature of solvent have an influence on the hydrolysis to condensation ratio and thereby determine the properties of the resulting sol-gel product [14].

2.2.2. Thin Film Deposition Methods

2.2.2.1. Spin coating

Spin coating is another cheap and fast method to produce homogeneous layers. Spin coating has been used to deposit ultrathin and extremely flat films on flat substrates for several decades. Various materials, including resin, epoxy, polymers, and sol-gel stock solutions, have been successfully coated on several different materials, metal, glass, ceramic, plastic, paper, and semiconductor substrates.

The theory behind this coating technique involves the equilibrium between the centrifugal forces created by the rapid spinning and the viscous forces determined by the viscosity of the liquid. The film thickness can be varied by controlling the spin speed and time, as well as the viscosity of the solution. The spin coating process can be divided into the four stages : deposition, spin up, spin off, and evaporation as showed in Figure 2.4 (a).

An excess amount of the dispersion is placed on the substrate, which is then rotated at high speed in order to spread the fluid by centrifugal force. The film thickness can be adjusted by varying the rotation speed, the rotation time, and the solid concentration of the dispersion. Unlike dip-coating, only one side of the substrate is coated by spin-coating.

The film thicknesses (t) is inversely proportional to the square root of spin speed (ω : angular velocity).

$$S = \frac{1}{\sqrt{\omega}} \quad (\text{Eq. 2.11})$$

The major advantages of spin coating are robustness, reproducibility, uniformity, simplicity, tunable film thicknesses, easy to apply to different substrate materials, and low cost process [19].

The main disadvantage of this method compared to dip-coating is that certain amount of raw material is wasted by spinning out of the substrate. Similar to dip-coating, post-heat treatment is necessary.

2.2.2.2. Dip coating

Dip coating technique can be described as a process where the substrate to be coated is immersed in a dispersion and then withdrawn with a well-defined withdrawal speed. The stages of dip-coating process are shown in Figure 2.4 (b). The coating thickness is mainly defined by the withdrawal speed, the solid content and the viscosity and evaporability of the solvent. The faster withdrawal speed, higher solid concentration and higher solvent evaporability result in thicker films.

The main advantages of dip-coating are: i) this method is cheap and easy to set up, ii) complicated shapes can be coated, and iii) no waste of raw material. However, the disadvantages are: i) the whole substrate is coated but only one side is necessary for most of applications, and ii) post-heat treatment is usually necessary to sinter the particles, especially for conducting films.

2.2.2.3. Spray coating

Spray coating is mainly used for its ability to coat nonplanar structure like steps, trenches, and stacks on semiconductor chips. In this process, very fine droplets are formed from the coating solution using atomizers or nebulizers as shown in Fig. 2.4 (c). Compared with spin and dip coating, the solution viscosity has to be greatly reduced to facilitate the nebulization process to form fine droplets. These fine droplets are then carried into the coating chamber with a carrier gas and deposited on the substrate by gravity or with an electrostatic field, where the negatively charged droplets are attracted to the electrically grounded substrate. The advantages of electrostatic spray coating over traditional gravitational spray coating are high deposition rates and low material loss.

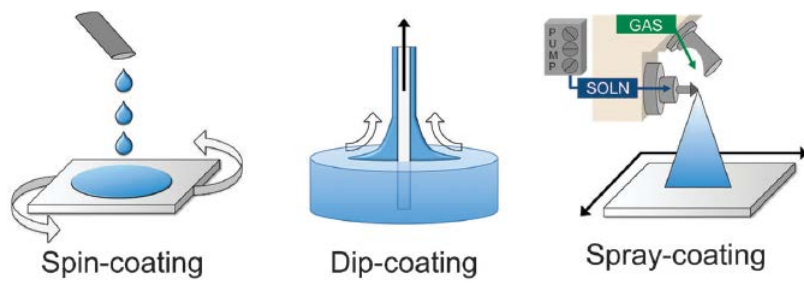


Fig. 2.4. Schematic diagram of (a) spin, (b) dip, and (c) spray coating [20].

2.3. Metal oxide semiconductor

2.3.1. Electronic structure and conduction mechanism of amorphous oxide semiconductor

2.3.1.1. Electronic structure

The electronic structure in amorphous oxide semiconductors is quite different from that in Si-based semiconductors. The properties of amorphous silicon are usually inferior to single crystalline silicon. For example, the mobility of a-Si:H is less than $2 \text{ cm}^2/\text{Vs}$ while that of c-Si is $\sim 1500 \text{ cm}^2/\text{Vs}$. In silicon, the conduction band minimum (CBM) and valence band maximum (VBM) are made of anti-bonding ($sp^3\sigma^*$) and bonding ($sp^3\sigma$) states of Si hybridized orbitals, and its band gap is formed by the energy splitting of the $\sigma^*-\sigma$ level (Figure 2.5 (a)) [21]. On the other hands, the amorphous oxide semiconductors have strong ionicity and charge transfer occurs from heavy metal ion to oxygen atoms (Figure 2.5 (b)). When a metal ions and oxygen ions comes close, charge transfer occurs due to largely different electron affinity. This can be explained by the Madelung potential. The Madelung potential which is the difference of negative electrostatic potential of the cations and the positive electrostatic potential of the anions stabilizes the ionized

states. Therefore, the conduction band minimum (CBM) is comprised of unoccupied the s orbitals of cations and the valence band maximum (VBM) is occupied O 2p orbitals shown by Figure 2.5(c). The CBM consists of spherically spread s orbitals of the heavy metal cations and their overlaps with the neighboring metal s orbitals are not affected largely by the disordered local structure [1]. As a result of this, the electron transport is not influenced and the amorphous oxide semiconductor has higher mobility than amorphous Si. Figure 2.2 shows the schematic orbital drawing for carrier transport path for Si-based and metal oxide semiconductors. In the amorphous structure, the strained chemical bonds of sp^3 or p orbitals form deep and high density of localized states beneath CBM and above VBM (Figure 2.6 (a)). Therefore, these localized states hinder the transport of electron hopping and resulted in lower device performance than c-Si semiconductor. On the other hands, in metal oxide semiconductor, large sized s-orbital of metal ion are overlapped directly between an adjacent atoms leading the current path of electron carrier as shown Figure 2.6 (b).

2.3.1.2. Conduction mechanism

Nomura et al. found that the hall mobility (μ_e) increases with increasing carrier density (N_e) for all the IGZO films including crystalline film [22, 23]. This trend is

opposite to that of simple crystalline semiconductors which exhibit the decrease of μ_e due to impurity scattering. Figure 2.3 shows the temperature dependence of hall mobility and carrier density in a-IGZO film. The mobility shows thermally-activated behavior at $10^{17} < N_e$ while carrier concentration does not. In addition, $T^{-1/4}$ temperature dependence of the conductivity was reported and a percolation model is employed for electron transport in IGZO. According to this model, the distribution of potential barriers is existed around the conduction band edge due to a random distribution of Ga^{+3} and Zn^{+2} ions in amorphous semiconductors as shown figure 2.4. When the Fermi level is below the threshold energy, electron conduction is dominated by the percolation mechanism leading the flow of the electrons through the percolation path between potential energy barriers as shown in figure 2.4. Therefore, $T^{-1/4}$ temperature dependence of the conductivity can be observed. On the other hand, as the Fermi level is raised above the threshold energy, the carrier density is already degenerated and the electron transport is dominated by degenerated conduction.

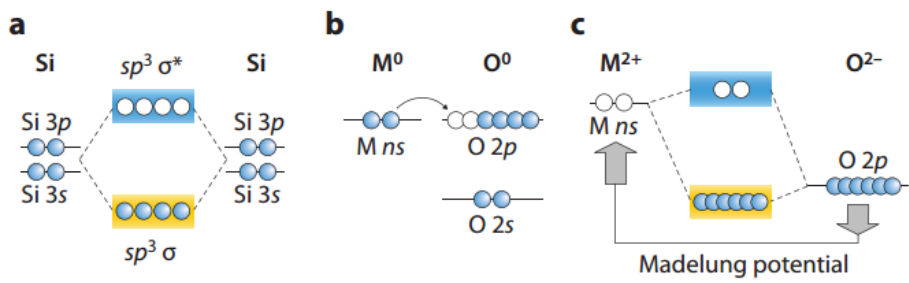


Fig. 2.5. Schematic electronic structures of silicon and ionic oxide semiconductors.

Bandgap formation mechanisms in (a) covalent and (b,c) ionic semiconductors [21].

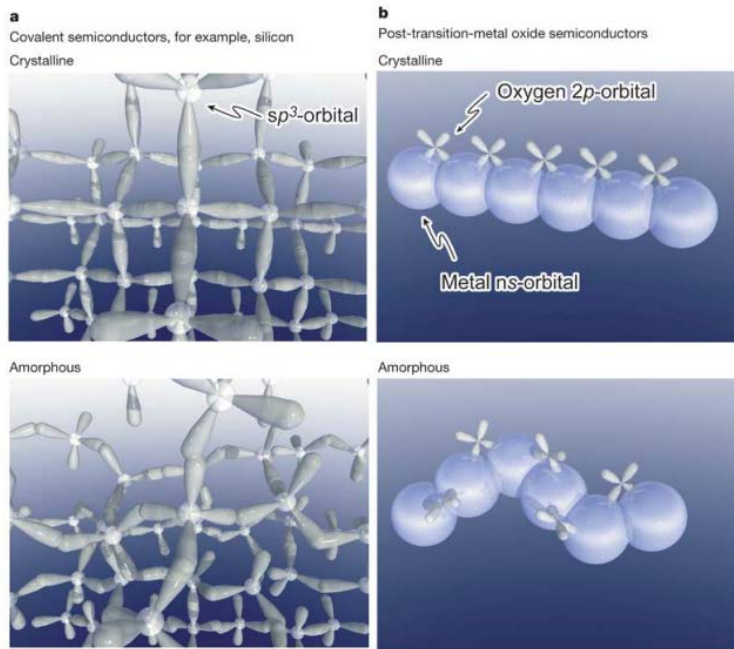


Fig. 2.6. Schematic orbital structure of the conduction-band minimum in Si and in an ionic oxide semiconductor [1].

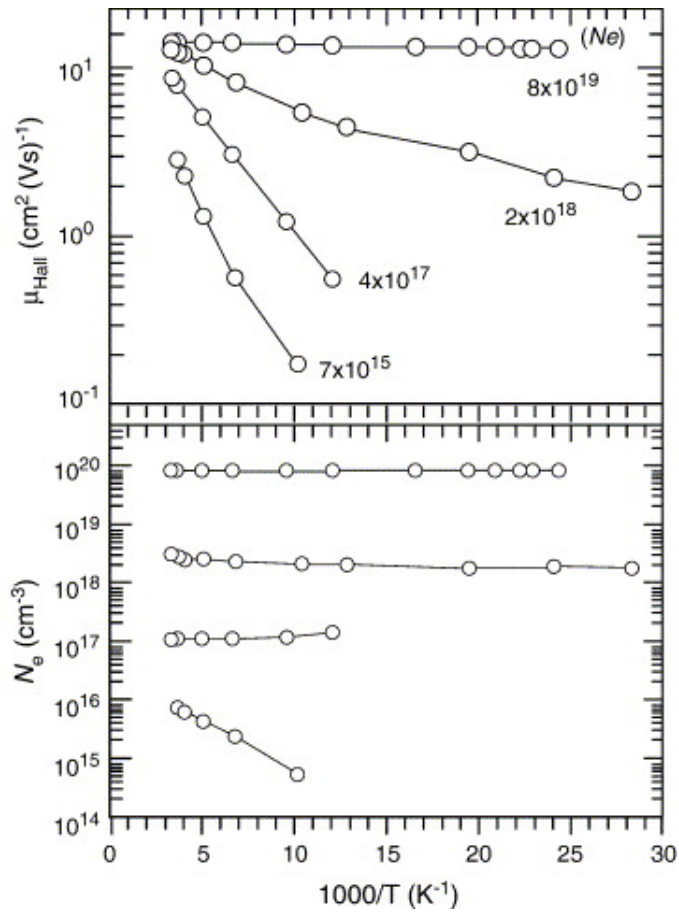


Fig. 2.7. Temperature dependences of Hall mobility, (μ_{Hall}) and carrier concentration, (N_e) for a-IGZO [23].

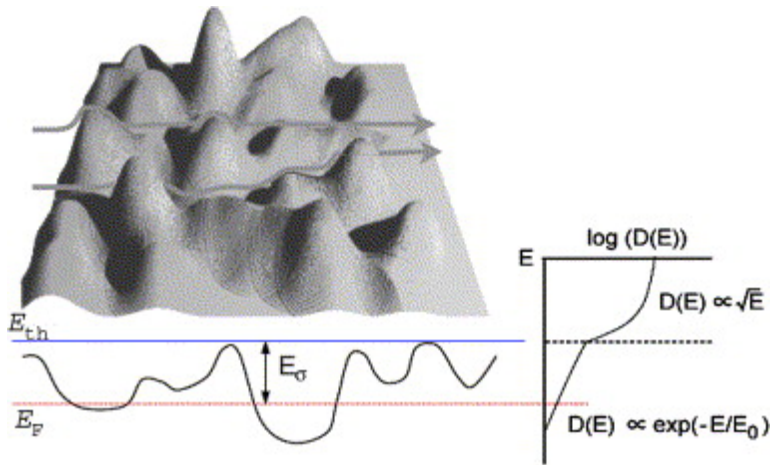


Fig. 2.8. Schematic illustration of conduction and electronic structure around conduction band edge. An arrow is an electron conduction path. (left bottom) potential distribution cross-section. E_{th} and E_F denote threshold energy at above which carrier moves freely and Fermi level, respectively. (Right) Density of state [5].

2.3.2. Amorphous oxide thin film transistor

2.3.2.1. Single component oxide TFTs : ZnO, SnO₂, In₂O

Transparent conductive oxide (TCOs) such as ZnO, SnO₂, and In₂O₃ exhibits very unique characteristics which are both high optical transparence in the visible range and high electrical conductance. TCOs are widely used in electronic as well as optoelectronic devices.

In 2003, the first reports on zinc oxide (ZnO) as channel material for TFT applications were demonstrated by Masuda *et al.* [24], Hoffman *et al.* [25] and Garcia *et al.* [26]. Masuda *et al.* demonstrated bottom-gate ZnO TFTs using pulsed laser deposition (PLD). The ZnO layer was deposited at 450 °C with a double layer consisting of SiO₂ and SiN_x as the gate insulator. The ZnO TFTs exhibited I_{on}/I_{off} ratio of 10^5 , V_{th} of 2.5 V and μ_{eff} of 0.03 cm²/Vs. Hoffman *et al.* also reported ZnO-based transparent TFTs using ion beam sputtering. The resistivity of ZnO channel layer was increased with increasing annealing temperature from 600 – 800 °C. The n-type enhancement-mode behavior with I_{on}/I_{off} ratio of $\sim 10^7$ was achieved. Garcia *et al.* fabricated ZnO TFTs by RF magnetron sputtering on Si substrates at room temperature. Their result showed the ZnO TFTs with high transparency in the visible, excellent transistor characteristics, and low-temperature processing can be

achieved.

Fortunato *et al.* also demonstrated the possibility of producing fully transparent high-quality ZnO-based TFTs with RF sputtering at room temperature [27]. Their ZnO TFTs exhibited high saturation mobility of ~ 20 V, V_{th} of 21V and I_{on}/I_{off} of $\sim 2 \times 10^5$.

Although In_2O_3 is an n-type semiconductor, it is not commonly used as the TFT semiconductor layer due to the difficulty in controlling carrier concentrations in the channel. However, In_2O_3 have attractive characteristics such as a wide-bandgap (3.6–3.75 eV), appreciable single-crystal mobility ($160 \text{ cm}^2/\text{Vs}$), and high film transparency in the visible region ($> 90 \%$). Wang *et al.* fabricated inorganic-organic hybrid In_2O_3 based TFTs by ion-assisted deposition process [28]. They altered the O_2 partial pressure and ion beam power to control the carrier concentration to 10^{17} - 10^{20} cm^{-3} in In_2O_3 films. The fabricated inorganic-organic hybrid In_2O_3 exhibit excellent operating characteristics with large field-effect mobility of $> 120 \text{ cm}^2/\text{Vs}$, I_{on}/I_{off} ratio of $\sim 10^5$, and near-zero threshold voltages.

There are two type of Tin oxide semiconductor: n-type (SnO_2) and p-type (SnO). Presley *et al.* demonstrated transparent SnO_2 TFTs with Maximum field-effect mobility of $2.0 \text{ cm}^2/\text{Vs}$ [29]. SnO_2 film as a channel layer was deposited by RF magnetron sputtering and annealed in O_2 at $600 \text{ }^\circ\text{C}$. The very thin channel layer (10–20 nm) is employed to control the V_{th} of TFTs.

2.3.2.2. In incorporated multi component oxide TFTs

The single component oxide material can be easily crystallized during the deposition process, leading to the formation of grain boundary defects. The existence of grain boundaries causes a non-uniformity problem. This means they are not appropriate as a channel material of the TFTs due to non-uniformity.

In 2004, Nomura et al. first demonstrated transparent and flexible amorphous IGZO (*a*-IGZO) TFTs (InGaZnO_4) [1]. The *a*-IGZO channel layer was deposited by PLD at room temperature and using a Y_2O_3 gate insulator on 200 μm -thick polyethylene terephthalate substrates. The TFTs exhibited a mobility of 6-8 cm^2/Vs , V_{th} of 1.6 V, and I_{on}/I_{off} ratio of $\sim 10^3$, respectively. They found that the incorporated Ga^{3+} ions decrease the carrier concentration due to the strong bind with oxygen ion. Since the publication of this report, various multi component oxide TFTs have been intensively investigated.

Yabuta *et al.* reported further improved device performance of amorphous IGZO-based (InGaZnO_4) TFTs. The amorphous IGZO was fabricated by RF sputtering without intentional substrate heating. The channel mobility, V_T , and I_{on}/I_{off} are 12 cm^2/Vs , 1 V, and 10^8 , respectively [30].

The compositional optimization of cation in IGZO channel is reported by Iwasaki *et al.* They fabricated IGZO channel using rf co-sputtering from three

ceramic targets of In_2O_3 , Ga_2O_3 , and ZnO . They found that the mobility is largely influenced by the In composition and Ga addition suppress carrier generation induced by In addition. The best TFT performance was obtained with a compositional ratio of In : Ga : Zn = 37 : 13 : 50 with saturation mobility of 12 cm^2/Vs , a V_{th} of 3 V, and an I_{on}/I_{off} of $\sim 7 \times 10^7$ [31].

Dehuff *et al.* reported high mobility, *n*-type transparent thin-film transistors (TTFTs) with a zinc indium oxide (ZIO) channel layer by rf sputtering [32]. The ZIO films annealed at 300 – 500 °C were amorphous, while annealed at 600 °C was polycrystalline. The ZIO TTFTs are highly transparent with ~ 85 % optical transmission in the visible portion. ZIO TTFTs annealed at 600 °C have excellent channel mobilities of 45–55 cm^2/Vs , drain current on-to-off ratios of $\sim 10^6$, and inverse subthreshold slopes of ~ 0.8 V/decade. On the other hand, ZIO TTFTs annealed at 300 °C exhibit less device performance with drain-current saturation, peak incremental channel mobilities of 10–30 cm^2/Vs , drain current on-to-off ratios of $\sim 10^6$, and inverse subthreshold slopes of ~ 0.3 V/decade.

Fortunato *et al.* demonstrated transparent IZO TFTs with the use of amorphous binary In_2O_3 - ZnO oxides as channel layer [33]. IZO TFTs deposited at room temperature by rf sputtering. The IZO TFTs showed saturation mobility higher than 100 cm^2/Vs , which is at least two orders of magnitude higher than that of conventional amorphous Si TFTs. The threshold voltage, subthreshold slope, and

on-off current ratio were 6 V, 0.8 V/decade, and 10^7 , respectively.

Because a-IGZO exhibited the potential for high mobility, excellent uniformity in the device parameters, and good scalability to a large substrate size, several prototype displays based on a-IGZO TFTs have already been demonstrated, including 12.1 inch WXGA AMOLEDs [13], 15 inch XGA AMLCDs [34], and 6.5 inch flexible AMOLEDs [35].

2.3.2.3. Zinc tin oxide TFTs

Although several proto type display devices with a-IGZO TFTs are presented and close to commercialization due to its high mobility, low temperature operation, and good transparency, several concerns are appeared. In and Ga are one of the scarce and expensive material in the earth crust and the resulting high price is an obstacle to its widespread utilization in mass-produced printed electronics [7]. In this respect, ZnSnO (ZTO) has been researched recently as a desirable active layer owing to its elemental abundance and low cost.

ZTO possesses several different phases, depending on the stoichiometry and pressure. The perovskite (ZnSnO_3) phases are dominant at 600 °C and better to detect the gas [36]. Although both inverse-spinel and perovskite phases are thought to be almost equally stable, the inverse-spinel structure may be more

thermodynamically stable than the perovskite counterpart since the ceramic ZnSnO_3 powder was reported to be decomposed to Zn_2SnO_4 and SnO_2 when calcined at a temperature higher than $700\text{ }^\circ\text{C}$.

The bandgap is reported to be $\sim 3.35\text{ eV}$ for Zn_2SnO_4 [37] and $\sim 3.5\text{ eV}$ for ZnSnO_3 [38]. The bandgap of ZTO can increase with increasing free electron density due to the Burstein-Moss effect, or can decrease due to the existence of band tail states [37]. The conduction band minima of amorphous and crystalline ZnSnO_3 mainly consisted of Sn 5s state, while a higher non-uniform localization of these states was observed in the amorphous phase compared with the crystalline counterpart [39].

Kang et al. reported the microscopic properties of oxygen vacancy in the amorphous Zn_2SnO_4 through the first-principles calculation [40]. Figure 2.9. show the crystal structure of c- Zn_2SnO_4 and a- Zn_2SnO_4 . They found the oxygen vacancy ($\text{V}_{(\text{O})}$) is found to play a shallow donor as sources of *n*-type conductivity in the a-ZTO.

In 2005, Chiang et al. firstly demonstrated amorphous zinc tin oxide (ZTO) TFTs with bottom-gate structure [2]. The channel layer was deposited on a heavily doped Si wafer as a substrate and thermally grown SiO_2 (100nm) as a gate insulator by rf magnetron sputtering. The ZTO film was amorphous phase even after annealing at $650\text{ }^\circ\text{C}$. The best TFT performance was obtained with a ZTO TFTs

annealed at 600 °C with μ_{eff} of 20-50 cm²/Vs, a V_{th} of -5-5 V, and an I_{on}/I_{off} of $\sim 10^7$.

Jackson *et al.* fabricated the flexible ZTO TFTs on flexible polyimide substrates by sputter deposition [41]. The flexible ZTO TFTs exhibited high channel mobilities of 14 cm²/Vs, I_{on}/I_{off} ratios of 10^6 , subthreshold voltage slopes of 1.6 V/decade, turn-on voltages of -17 V. They also found that the ITO as S/D electrode provides a low contact resistance for ZTO TFTs and the ZTO can be a promising channel material for the fabrication of high performance TFTs on flexible substrates.

Hong et al. developed a novel deposition method involved sequential radio-frequency sputter deposition to obtain a multi-component oxide thin film [42]. This materials development methodology is demonstrated through the realization of high-performance TFTs with channel layers composed of zinc oxide/tin oxide, and tin oxide/indium oxide. The post-deposition anneal induces inter diffusion and remixing of the binary oxide constituents, resulting in the formation of a ternary oxide.

Hoffman reported the effects of zinc tin oxide composition (Zn:Sn ratio) and post-deposition anneal temperature on electrical performance [43]. The channel mobility reaches a broad peak for intermediate compositions and anneal temperatures, while turn-on voltage decreases with increasing anneal temperature and decreasing Zn:Sn ratio. These results suggested the potential of zinc tin oxide as a candidate TFT channel layer material.

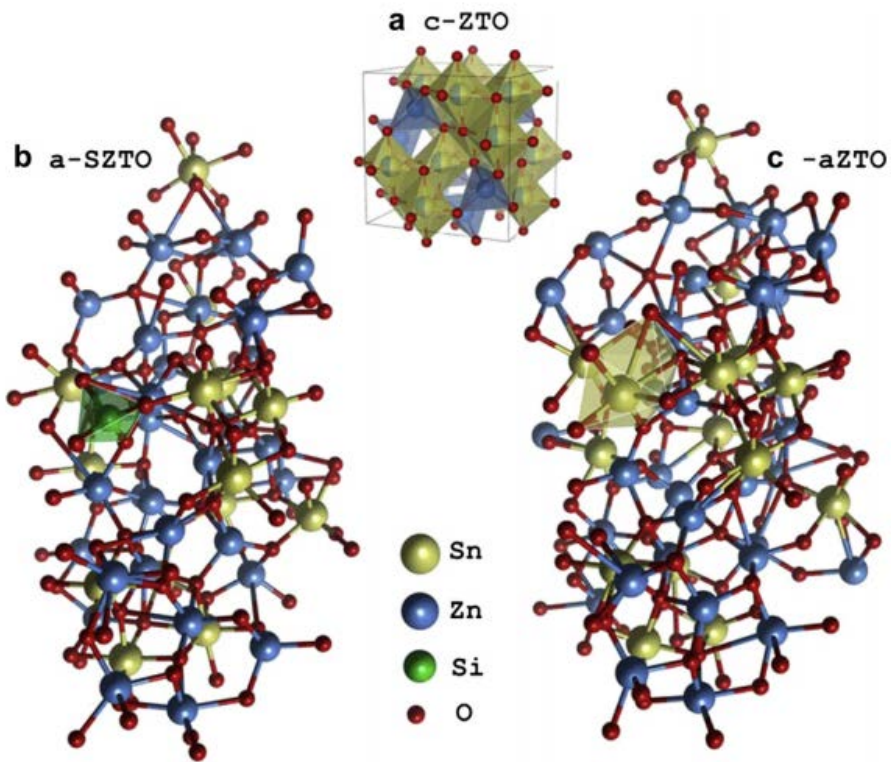


Fig. 2.9. (a) The crystal structure of $c\text{-Zn}_2\text{SnO}_4$. The amorphous structure of (b) a-SZTO and (c) a-ZTO [40].

2.3.3. Solution Processed Amorphous Oxide Thin Film Transistor

The aforementioned oxide thin film transistors were fabricated by the vacuum based deposition method such as magnetron sputtering, pulsed laser deposition (PLD), chemical vapor deposition (CVD), and atomic layer deposition (ALD). However, vacuum-based processes are expected to be unsuitable for very large flat panel displays due to the high manufacturing cost. The solution-processed formation of the oxide layer is a viable alternative because of its process simplicity, low cost, and high throughput.

A glass is commonly used as a substrate in most display devices so that process temperature should be considered carefully. On the other hand, the solution processed oxide semiconductors normally require annealing at high temperatures ~ 400–500 °C to improve the device performance. The residual impurities can cause the serious degradation of device performance and stability. The low-temperature solution-processed oxide TFTs is approached by various annealing technology such as high pressure oxygen annealing or ultraviolet photo-annealing.

However, the device performance and stability of the oxide TFTs annealed at low temperature is still inferior to that of the oxide TFTs fabricated at high temperature. In addition, solution processed oxide TFTs still have relative low carrier mobility and high instability compared to that by vacuum process.

Nevertheless, solution based oxide TFTs have been intensively investigated for realizing flexible and printed electronic device with large area.

2.3.3.1. Colloidal -based oxide TFTs

The properties of nano particles are easily manipulated in a thermodynamically or kinetically controlled manner, and nano particles are converted to a granular film by chemically/thermally induced structural transformations.

Sun et al. fabricated colloidal zinc oxide (ZnO) TFTs by controlling the shape of the nanocrystals from spheres to rods [44]. The electrical properties of ZnO films were improved with increasing particle size and self-alignment of the nanorods along the substrate. TFT devices with 65-nm-long and 10-nm-wide nanorods were deposited by spin coating at 230 °C as shown Figure 2.10. The ZTO TFTs exhibited poor channel mobilities of 0.61 cm²/Vs and I_{on}/I_{off} ratios of 3×10^5 . Faber et al. also fabricated ZnO TFTs based on ZnO nanoparticles for the semiconductor and polyvinylphenol as the gate dielectric deposited by spin-coating at 100 °C [45]. They obtained μ_{eff} of 0.008 cm²/Vs for bottom-gate TFTs and 2.5 cm²/Vs for top-gate TFTs .

Although, the colloidal-base oxide TFTs can be fabricated by simple and low temperature process, the device performance is limited due to the inefficient carrier

transport at junctions between neighboring nano particles.

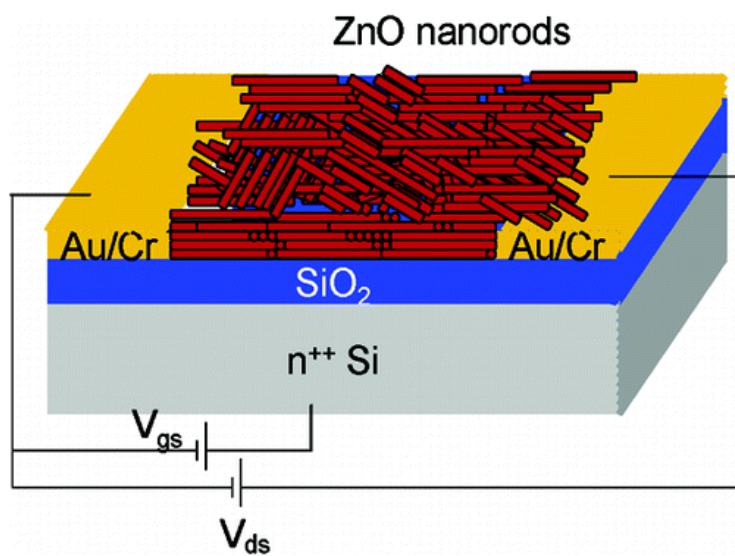


Fig. 2.10. Device structure of colloidal-based ZnO TFT [44].

2.3.3.2. Metal salt-based oxide TFTs

As mentioned before, the devices performance of nanoparticle based oxide TFTs usually show poor and some instability due to the large surface area and interfacial area between nanoparticles. On the other hand, the metal salt-based approach has the advantage of mixing different metal precursors in the same solution.

In metal salt-based sol-gel chemistry, the precursor solution is synthesized by dissolving metal salt precursors in solvents with stabilizing agents and H₂O. Metal cations form chemical complexes with water molecules, solvent molecules, and stabilizing agents. The resulting metal cations undergo a hydrolysis reaction through the loss of a proton by one or more of the water molecules that surround the metal cation in the first solvation shell. As a consequence, the aquo ligand molecule, H₂O, bonded to the metal cation is transformed into either a hydroxo ligand, OH, or an oxo ligand, O₂. Subsequently, a condensation reaction occurs due to the oxolation generating an oxo-bridge, M-O-M, allowing the formation of a metal oxide skeleton framework with a dense microstructure [46].

The first reports on the possibility to deposit metal salt-based ZnO TFTs was by Ohya *et al.* [47]. They obtained the TFT mobility of 0.2 cm²/Vs and the I_{on}/I_{off} ratios of 10⁷ at annealed 900 °C. Li *et al.* fabricated ZnO TFTs using both spin coating and drop coating. ZnO TFTs annealed at 490 °C exhibited channel mobilities,

threshold voltages, and I_{on}/I_{off} ratios of 5-6 cm²/Vs, 20 V, and 10⁵, respectively [48].

Multi-component oxide TFTs using solution process have also been intensively investigated to achieve high electrical performance with an amorphous structure since amorphous InGaZnO (a-IGZO) by conventional vacuum processes exhibit excellent electrical performance and stability. In 2007, Lee *et al.* developed a general and low-cost process to fabricate metal oxide semiconductors for thin-film electronics using melt halide precursors dissolved in acetonitrile as a solvent. The fabricated zinc indium oxide (ZIO) TFTs by both of ink-jet printing and spin-coating method in ambient condition. The ZIO TFTs fabricated by spin coating exhibited channel mobilities of 16.1 cm²/Vs which is superior to that (7.4 cm²/Vs) of ink-jet printing [49]. Chang *et al.* demonstrated the zinc tin oxide TFTs with metal halide precursor using spin coating [50]. The ZTO thin films were highly transparent (~95 % in the visible portion of the electromagnetic spectrum) and amorphous. The ZTO TFTs annealed at 600 °C exhibited field effect mobility (μ_{eff}) of 16 cm²/Vs, turn on voltage of 2V, I_{on}/I_{off} ratios of 10⁵.

The solution processed IGZO TFTs have been reported since 2009. Kim *et al.* reported nano-crystalline IGZO solution TFTs annealed at 450 °C [51]. They fabricated IGZO TFTs using the solution of zinc acetate, indium nitrate, and gallium nitrate precursors. They reported the effect of indium incorporation into IGZO which enhances the field effect mobilities of the TFTs and decreases the

surface roughness of the films.

However, these methodologies generally require high temperatures annealing, usually higher than 400 °C to complete precursor decomposition and avoid undesirable contamination of the semiconductor. This high temperature process is incompatible with the use of plastic substrates. The variety of approach has been investigated. Banger *et al.* fabricated IZO and IGZO TFTs using a hydrolysis annealing technique from alkoxide-based sol-gel-on chip metal oxide semiconductors [52]. When metal alkoxides are exposed to a wet environment, hydrolysis and condensation occur, which involve proton transfer from the incoming water molecule to the bound alkoxide ligand and subsequent elimination of the protonated leaving group. These chemical reactions afford the M–O–M frameworks at low temperatures. They obtained the field effect mobility (μ_{eff}) of 7-12 cm²/Vs for IZO TFTs and 14 cm²/Vs for IGZO TFTs.

Another approach is tried to lower annealing temperature and get high performance. Jun *et al.* fabricated solution processed ZnO TFTs with an aqueous inorganic precursor and microwave-assisted annealing [53]. ZnO TFTs prepared at 140 °C by microwave irradiation exhibited channel mobility of 1.7 cm²/Vs and $I_{\text{on}}/I_{\text{off}}$ ratios of $\sim 10^7$ with good air stability.

As a result of this, several prototype display devices with solution processed oxide TFTs as a channel layer has been reported. Samsung Electronics have

intensively studied solution processes and reported the first solution-processed oxide TFT panels in the form of a 2.2-inch mono-QQVGA (Quarter Quarter Video Graphic, 128×160) AMOLED with a bottom-emission structure as shown in Figure 2.11 [54]. Taiwan TFT LCD Association (TTLA)/Inpria Corp./Oregon State University also reported a 4.1-inch QVGA AM-LCD panel.

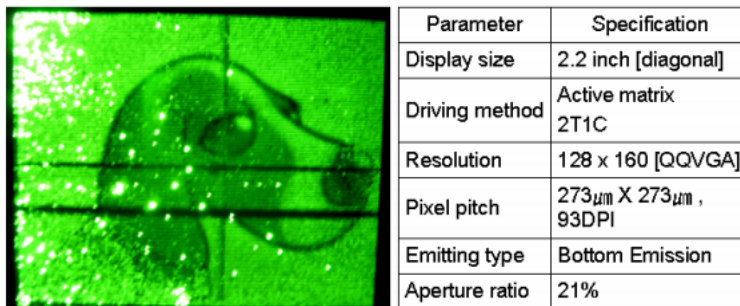


Fig. 2.11. Displayed image of 2.2 inch QQVGA mono AMOLED and panel specification [54].

2.4. Instability of oxide tin film transistors

2.4.1. Positive bias stress

The unit pixel circuit of an AMOLED consists of switching TFT and driving TFT. For switching TFT, the variation of V_{th} is less critical due to the margin of operation condition to be controlled by on- and off voltage. However, the V_{th} shift to the positive direction should be considered in AMOLED driving TFT. Because the brightness of each pixel is highly dependent on the drain current of the driving transistor, which imposes a stringent limitation on the time or temperature dependences of the μ_{FE} and V_{th} values [55]. It has been reported that a V_{th} shift of the driving transistor by 0.1 V induces variations in the resulting luminance of the OLED pixels by approximately 20%, which reflects the fact that the brightness of each pixel depends strongly on the drain current [56]. Therefore, the device instability of oxide TFTs under positive gate bias stress (PBS) should be improved for implementation of commercial AMOLED.

Figure 2.12. shows evolution of the transfer characteristics as a function of the positive bias stress time. The V_{th} has a parallel shift to the positive direction by positive bias stress without change in mobility and subthreshold slope value. This positive V_{th} shift under the application of PBS can be explained by negative charge

trapping at the gate insulator/channel interface or negative charge injection into the gate dielectric bulk region [57, 58], the creation of defects in the semiconductor material [59], and/or the ambient dynamics of un-encapsulated back channel region [60]. The charge injection model requires a larger de-trapping energy barrier and resulted in the degradation of mobility and SS value. In contrast to, the charge trapping model does not compared to the charge trapping model and showed only a parallel shift of V_{th} . Cross et al. reported the parallel shift of V_{th} to the positive direction with either little or no change of SS values [57]. They found that the positively shifted V_{th} recovered rapidly to their initial state after 15 min under the 12 V without any thermal annealing process. Similar results were reported in oxide TFTs with channel materials composed of an In_2O_3 and IGZO film [61, 62]. Hosino et al. found that constant voltage-bias stressing leads to the rigid positive $\log(I_D)$ - V_{GS} transfer curve shift under the positive gate bias over period of 10^5 s and recovery of the transfer curve toward the prestressed state was observed in the dark at room temperature. These results suggest that the positive V_{th} shift can be attributed to charge trapping rather than charge injection. The charge trapping model can be described using the following stretched-exponential equation [63]:

$$\Delta V_{th}(t) = V_0 \left\{ 1 - \exp \left[- \left(\frac{t}{\tau} \right)^\beta \right] \right\}, \quad V_0 = V_g - V_{th,0} \quad (\text{Eq.2.12})$$

where t is the time, τ is the relaxation time constant, β is the dispersion parameter, and $V_{th,0}$ is V_{th} before stress.

The positive V_{th} shift due to the charge trapping at the gate insulator/channel interface or negative charge injection into the gate dielectric bulk region can be suppressed by reducing the density of interfacial traps (N_{it}) or channel bulk trapping state. The O_2 plasma treatment of SiN_x gate insulator induced the formation of SiO_xN_x which resulted in the improvement of the PBS instability due to the reduction of the N_{it} of SiO_xN_x /IGZO [64]. Jeong et al. reported that the suitably passivated device did not exhibit any V_{th} shift while the device without any passivation layer showed a huge V_{th} degradation under PBS condition [60]. They found that electric-field-induced adsorption of oxygen from the ambient atmosphere is largely responsible for the increase of positive V_{th} shift due to the increased negatively charged-oxygen adsorption and charge trapping at the dielectric/channel layer (Fig. 2.13).

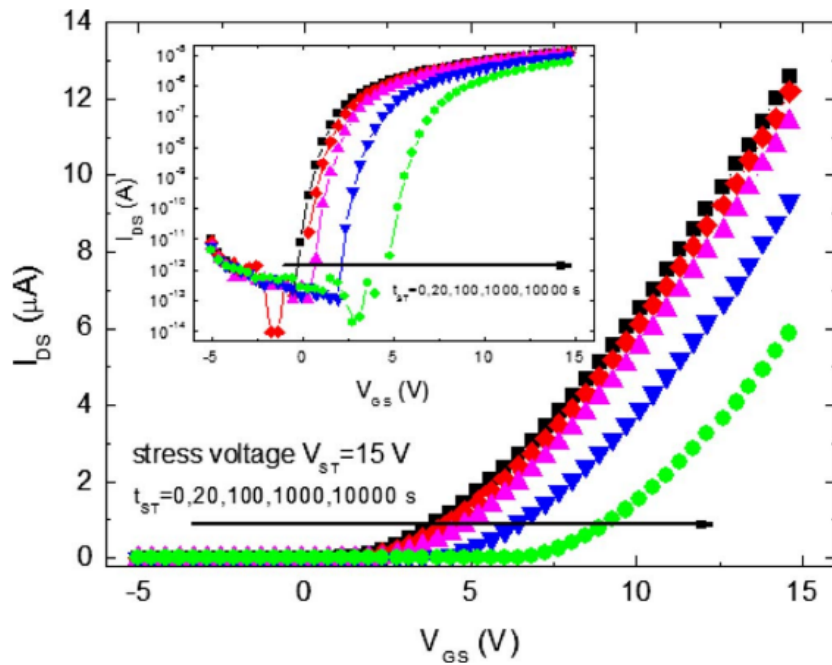


Fig. 2.12. Linear transfer I_{DS} - V_{GS} curve of a-IGZO TFTs as a function of stress time (t_{ST}). The inset shows the bias-stress-induced shift of $\log(I_{DS})$ - V_{GS} curve. The sweep was done at $V_{DS} = 0.5$ V in both curves [65].

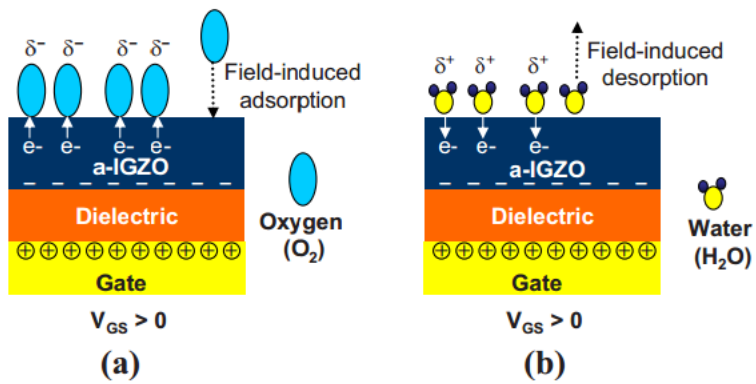


Fig. 2.13. (a) Schematic showing the electric-field-induced adsorption of oxygen molecules from the ambient atmosphere under the application of PGVS. (b) Schematic showing the electric-field-induced desorption of water molecules into the ambient atmosphere under positive V_{GS} stress [60].

2.4.2. Negative bias stress

All display devices including active matrix liquid crystal displays (AMLCD) and active matrix organic light emitting diodes (AMOLED) are exposed to light from a back light unit for AMLCD or self-emitting radiation for AMOLED. Even though the bottom-gate metal can be a shielding layer to block the most of light from back light unit in AMLCD, small portion of light can be illuminated by lateral refraction through the passivation layer and ITO layer as common electrode. In addition, the turn-on time of TFTs is $\sim 21 \mu\text{s}$, while turn-off time is 16.7 ms for the frame rate of 60 Hz. In other words, TFTs are placed in the negative bias condition for most operating time. Therefore, the negative bias thermal instability under illumination condition is more critical issue to be resolved before their implementation in commercial electronic products. Figure 2.14. shows the evolution of the transfer characteristics of ZnO TFTs under positive or negative gate bias stress with/without light [66]. The transfer curve showed almost no change under PBS with illumination, while the huge negative V_{th} shift was observed under NBIS condition. In the positive bias with illumination, the accumulated electrons in channel layer screen the electric field from the gate electrode under positive V_{GS} , which resulted the negligible electric field in the bulk oxide semiconductor region. Since the photo-generated electron-hole (e-h) pairs via the

band to band transition remain in the same channel region, these e-h pairs are recombined rapidly (Fig.2.15. (a)). In contrast, the channel layer is fully depleted by the negative gate bias, which results in the suppress of the recombination of photo-generated e-h pairs (Fig.2.15. (b)) [67].

The negative V_{th} shift in the NBIS condition can be considered as plausible origins; i) the photo-induced hole trapping [68, 69], ii) photo-induced ionization of pre-existed neutral oxygen vacancies (V_O) and trapping of positively doubly charged oxygen vacancies (V_O^{2+}) at oxide channel/gate insulator interface [70, 71], and iii) photo-induced desorption of O_2 on the back channel surface [72]. In the photo-induced hole trapping model, the photo-generated hole carriers drift toward the gate insulator by the negative electric field and are trapped at the gate dielectric/channel interfacial trap sites or gate dielectric bulk film, as shown in Fig. 2.16. Ji et al reported that the IGZO TFTs with SiN_x gate insulator exhibited inferior stability to that with SiO_2 gate dielectric layer, which was explained by the charge trapping mechanism. However, the negative displacement of the V_{th} of the SiN_x -gated IGZO TFTs in the NBIS condition was further accelerated compared to that of the SiO_2 -gated TFTs. This was attributed to the both injection of photo-created hole carriers into the gate dielectric bulk region and the hole trapping at the gate/channel interface [68]. Another instability mechanism under NBIS condition is the photo-induced ionization of V_O to V_O^{2+} . In this model, the two electrons can be

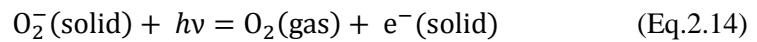
exited to the conduction band, according to the following equation:



Since there is an energy barrier (0.2-0.3 eV) between V_O^{2+} and V_O , the V_O^{2+} is hindered to return to V_O state, which resulted in the persistent photo-conductivity (PPC). Therefore, photo-ionized of V_O to V_O^{2+} can cause an increase the free electron carrier density, leading to a negative V_{th} shift . Furthermore, the V_O^{2+} can be attracted to the gate insulator by the negative electric field and are trapped at the gate dielectric/channel interfacial trap sites or gate dielectric bulk film accelerating NBIS degradation by acting positive fixed charge (Figure 2.17) [73].

On the other hand, the oxygen photo-desorption mechanism can be responsible for the negative V_{th} shift under NBIS. Yang et al. reported the photo-desorption of adsorbed oxygen ions on the back channel surface cause the light-enhanced V_{th} instability under light-illuminated negative stress conditions [74]. They fabricated the shot channel TFTs of Al-Sn-Zn-In-O (AT-ZIO) and passivation layer were deposited by photolithography and wet etching processes. The passivated AT-ZIO TFTs exhibited a much smaller negative V_{th} shift of 0.72 V under NBIS compared to that of TFTs without passivation layer. The unpassivated TFTs exhibited huge negative V_{th} shift of > 11.5 V after applying light-illuminated NBS for 10^4 . When

the oxygen molecules are adsorbed on the back channel surface of oxide TFTs, the desorption of oxygen species can be occurred by the applied photon exposure, resulted in the increase of free electrons into the metal oxide channel layer (Equation 2.14).



Because adsorbed or chemisorbed oxygen species have much lower bonding energy with the back channel surface than the applied photon energy. Figure 2.18 shows the oxygen desorption by light exposure and the subsequent donation of free electrons in the conduction band. Therefore, the increase of free carrier due to the photo-induced desorption of oxygen molecules enhance the deterioration of the negative V_{th} shift in metal oxide TFTs.

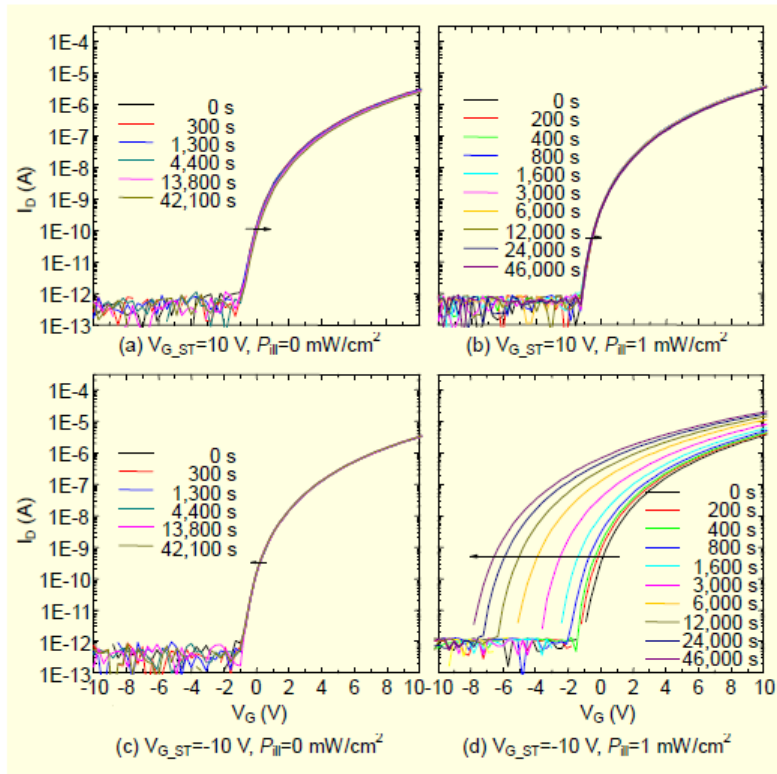


Fig. 2.14. Changes in the I_D - V_G characteristics of ZnO TFTs (a) under dark PBS conditions, (b) PBIS conditions with a photo-intensity of 1.0 mW/cm², (c) dark NBS condition, and (d) NBIS condition with photo-intensity of 1 mW/cm² [66].

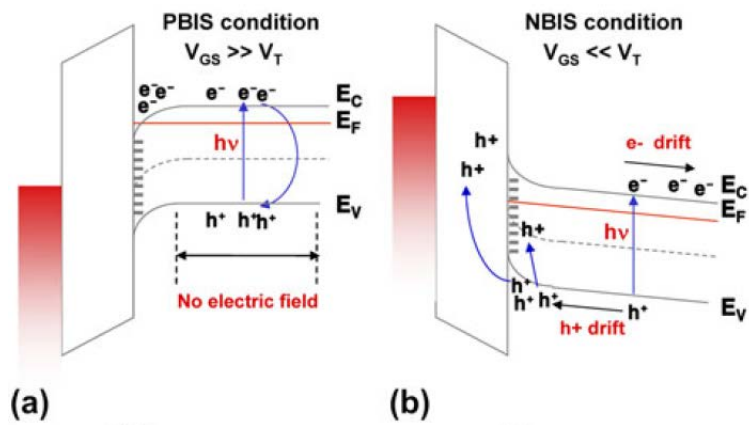


Fig. 2.15. Plausible energy band diagram of the MIS structure under (a) PBIS and (b) NBIS conditions [67].

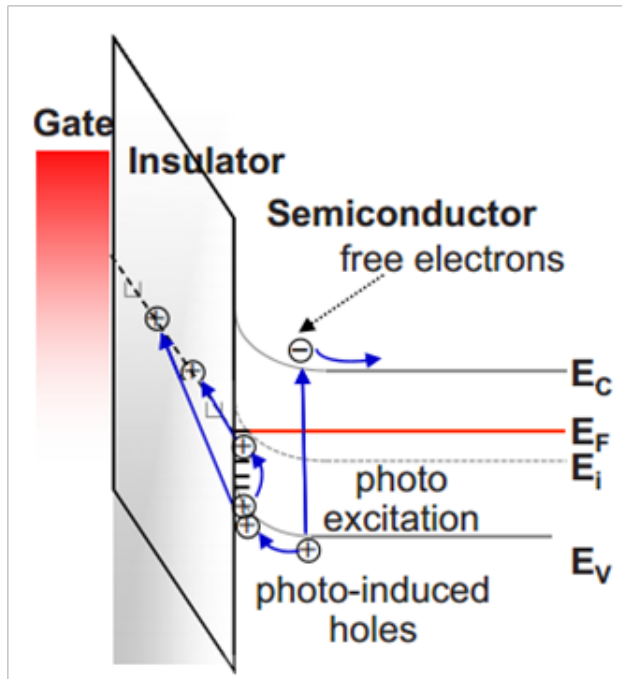


Fig. 2.16. Schematic band diagram, which is based on trapping or/and injection of a photo induced hole carrier [67].

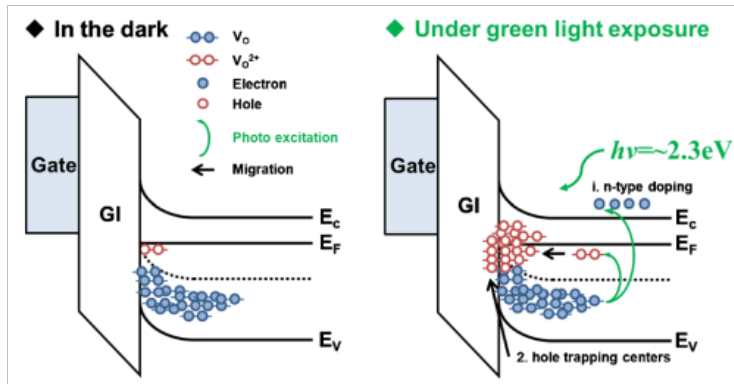


Fig. 2.17. The creation V_o^{2+} state and involved n-type doping mechanism [73].

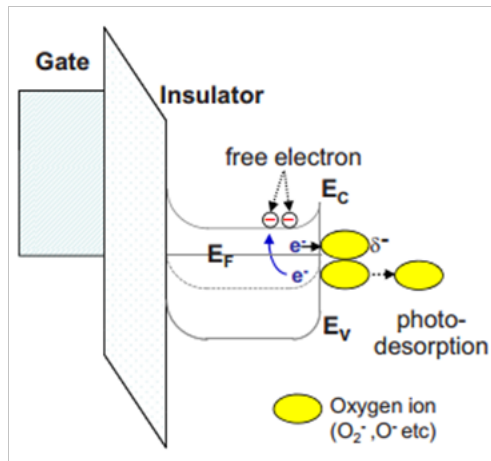


Fig. 2.18. Schematic energy band diagram showing the photodesorption of oxygen molecules into the ambient atmosphere for the unpassivated device under the application of NBS [74].

3. Experiments and Analyses

3.1. Experimental procedure

The experimental procedure is schematically depicted in Fig. 3.1. First, the precursor solution is prepared by dissolving metal salt in solvent. The dissolved solution stirred for 1 hour at 60 °C to form a homogeneous solution. Heavily-doped *p*-type Si and a 100-nm-thick thermally grown SiO₂ layer were used as a bottom gate electrode and a gate insulator, respectively. The substrate was cleaned sequentially with acetone, isopropanol and de-ionized water for 10 min, followed by exposure to ultraviolet light and ozone for 20 min to produce a hydrophilic surface. The homogeneous solution filtered through the 0.22 μm syringe filter and coated on SiO₂/Si substrate at 500 rpm for 5 s and then at 2000 rpm for 30 s. The resulting ZTO film was baked on hot plate at 150 °C for 10 min to evaporate the solvent and then annealed for 1 hr in air. The 100-nm-thick source/drain electrode composed of Tin-doped indium oxide (ITO) film (In₂O₃ : SnO₂ = 90 : 10 wt %) was deposited by dc magnetron sputtering at room temperature. Argon was used as the sputtering gas and dc power was fixed 100 W at the chamber pressure of 5 mTorr. The channel and source/drain electrodes were patterned using a shadow mask with a channel length of 300 μm and a width of 1000 μm, respectively. After the

deposition, the samples were annealed for 1 hour in air ambient. Finally, the fabricated device was encapsulated with poly methyl methacrylate (PMMA, MicroChem A4).

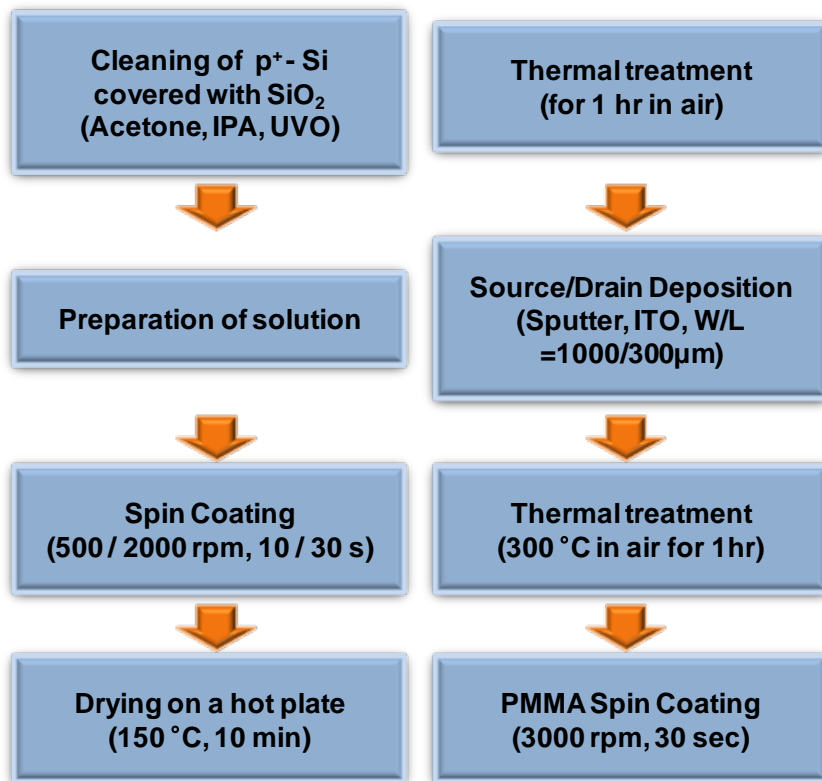


Fig. 3.1. Flow chart of solution processed ZTO thin film and TFT.

3.2. Analysis methods

In section 4.1, the surface morphology and roughness of the ZTO films were characterized by atomic force microscopy (AFM, JEOL, JSPM-5200) with tapping mode. The structural properties of spin-coated ZTO films were examined by glancing angle X-ray diffraction (GAXRD, PANalytical, X'pert-PRO MPD) and transmission electron microscopy (TEM, FEI, Tecnai F20). The electrical properties of the channel layers were obtained using a Keithley 4200 semiconductor characterization system at room temperature in air. The chemical structure of the ZTO films was evaluated by X-ray photoelectron spectroscopy (XPS, SIGMA PROBE, ThermoVG, U.K.). High-resolution X-ray reflectivity (XRR) was performed to evaluate the roughness, density, and thickness of the ZTO thin films (PANalytical, X'pert-PRO). The XRR data was fitted using the X'pert Reflectivity software package.

In section 4.2, the chemical compositions of the ZTO films were examined by X-ray fluorescence (XRF, Thermo scientific) spectroscopy, for which the atomic concentrations were calibrated by proton-induced X-ray emission. The structural properties of the ZTO films were evaluated by glancing angle x-ray diffraction (GAXRD, X'Pert PRO, PANalytical) using Cu k radiation and high-resolution transmission electron microscopy (HRTEM, FEI, Tecnai F20). The chemical state

of the ZTO films was examined by X-ray photoelectron spectroscopy (XPS, SIGMA PROBE, ThermoVG). The carrier density of the ZTO film was evaluated from Hall Effect measurements using the van der Pauw configuration. The electrical characteristics were measured using a HP 4155A semiconductor parameter analyzer at room temperature in air.

3.3. Electrical and Reliability Measurements

The electrical and Reliability characteristics were measured using HP 4145B and HP 4155A semiconductor parameter analyser at room temperature in air ambient. The V_{th} was determined by adjusting the gate voltage, which induces a drain current of $L/W \times 10$ nA at $V_{DS} = 10$ V [13]. To characterize the effects of negative bias illumination stress (NBIS) on the transfer characteristics of the ZTO-based FETs, the devices were stressed under the following conditions: a constant voltage (- 20 V) stress was applied to the gate of transistor, while the applied drain voltage was 10 V at room temperature, respectively, and the maximum stress duration was 12,000 s. The transfer curves were taken from one device, which means that the applied NBIS was interrupted in order to measure each IV curve as a function of the applied NBIS time. A white halogen lamp was employed as a light source and the photon wavelength was approximately 500 nm, which was selected through band-pass filters. The photo-intensity was ~ 2.0 mW/cm², as calibrated by photometry. The schematics of the illumination system were shown in Fig. 3. 2.

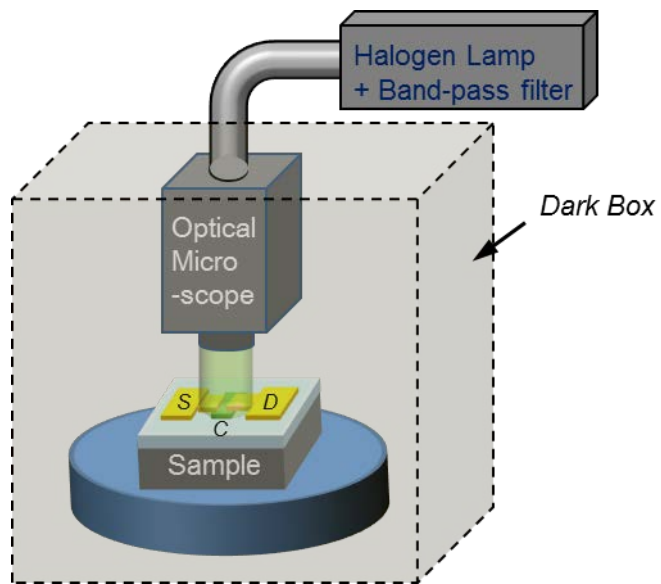


Fig. 3.2. Schematic diagram of the illumination system.

4. Results and Discussions

4.1. The effect of the annealing temperature on the device performance and photo-bias stability

4.1.1. Introduction

Zinc-based oxide thin film transistors (TFTs) have attracted considerable attention as a switching device for active matrix (AM) liquid crystal displays (LCDs) and Zinc-based oxide thin film transistors (TFTs) have attracted considerable attention as a switching device for active matrix (AM) liquid crystal displays (LCDs) and organic light-emitting diodes (OLEDs) owing to their high mobility, good transparency to visible light and low temperature capability compared to amorphous Si TFTs [1, 75]. High performance oxide channel layers have been prepared in general by vacuum-based deposition processes, such as sputtering, pulsed laser deposition (PLD), and atomic layer deposition (ALD), which comes with a high manufacturing cost [76-78]. In contrast, solution-processed formation of the oxide layer is a viable alternative, considering its process simplicity, low cost, high throughput. In addition, direct-writing capabilities of the solution process enables the realization of the low-cost printed electronics for

flexible displays and flat panel AM displays. For these reasons, the fabrication of high performance TFTs using solution-based oxide semiconductors, such as InGaZnO [79], InZnO [3], and InZnSnO [4], have been studied extensively. Although the use of indium in the active channel layer is believed to be essential for securing high channel mobility, its scarcity in the earth crust and the resulting high price is an obstacle to its widespread utilization in mass-produced printed electronics [7]. In this regard, ZnSnO (ZTO) has been highlighted recently as a desirable active layer owing to their elemental abundance and low cost.

Several studies have examined solution-based ZTO TFTs [80-85]. The device performance of the devices strongly depends on the annealing temperature and the chemistry of the precursors used. Jeong et al. reported the fabrication of ZTO TFTs using zinc acetate dehydrate [$\text{Zn}(\text{CH}_3\text{COO})_2 \cdot 2\text{H}_2\text{O}$] and tin acetate [$\text{Sn}(\text{CH}_3\text{COO})_2$] as Zn and Sn precursor, respectively [80]. The transistor performance with field-effect mobility (μ_{FE}) of $1.1 \text{ cm}^2/\text{Vs}$ was achieved when the channel layer experiences high-temperature annealing ($> 500 \text{ }^\circ\text{C}$). The formation of the channel layers using solution process involves the hydrolysis and condensation of molecular precursors, which results in the ionic network of metal-oxygen bonding. The required annealing temperature strongly depends on the precursor structure because the geometrical hindrance and interaction between ligands can affect the sol-gel process during heat treatment [86-89]. In addition, carbon atoms of the acetate-

based cation precursors can exist as a residue even after thermal annealing and it has an adverse effect on the device performance. Therefore, it is beneficial to use carbon-free molecules such as chlorides as metal precursors [81].

The switching TFTs in LCDs and OLEDs are operated under light from a back light unit and OLEDs. The device stability under the gate bias stress and light stress is an important issue for the implementation of oxide TFTs to the commercial electronic products. Although the effect of the annealing temperature, cation composition, and precursor chemistry on the device performance of solution processed ZTO TFTs have been investigated in detail, few studies have examined the fundamental relationship between their material properties (e.g. microstructure, density, and impurity) and the photo-bias instability of the soluble ZTO transistors.

In this paper, high performance solution-processed ZTO TFTs were fabricated using carbon-free ZnCl_2 and SnCl_2 precursors. The effect of the annealing temperature on the device performance, dark negative bias stress (NBS), and negative bias illumination stress (NBIS) instability was examined based on the structural and chemical characterization of the ZTO films. The relaxation time of V_{th} shift for various ZTO TFTs under NBS and NBIS conditions were also extracted by fitting to a stretched exponential equation, which was found to be strongly dependent on the structural and chemical properties of the soluble-processed ZTO films.

4.1.2. Experimental procedure

The precursor solution was prepared by dissolving 0.1 M ZnCl₂ (Aldrich) and SnCl₂ (Aldrich) in 10 mL of acetonitrile (CH₃CN, Aldrich). The Zn-to-Sn ratio of the precursors was 1:1. The precursor solution was stirred for 30 min at 60 °C. Heavily doped *p*-type Si with 100-nm-thick thermally grown SiO₂ gate oxide was used as a substrate for the fabrication of ZTO TFTs. The substrate was sonicated in acetone and isopropanol for 5 min, followed by ultraviolet ozone exposure for 20 min for generating hydrophilic surface. Spin coating of the ZTO layer was performed at 500 rpm for 5 s and then at 3000 rpm for 30 s. The resulting ZTO film was then dried at 200 °C for 10 min to evaporate the solvent and annealed at temperatures ranging from 300 to 600 °C for 1 hr in air. Tin-doped indium oxide (ITO) as source and drain electrodes (S/D) was deposited by dc magnetron sputtering and patterned by a metal shadow mask. The width (*W*) and length (*L*) of the fabricated device was 1000 and 300 μm, respectively. Finally, to prevent the dynamic interaction between the channel layer and ambient oxygen/moisture, the fabricated device was encapsulated with polymethyl methacrylate (PMMA, MicroChem A4).

4.1.3. Structural and chemical properties of ZTO thin films

Thermo-gravimetric analysis (TGA) was performed to monitor the thermal decomposition behavior of ZTO precursor solution, as shown Fig. 4.1. The weight loss observed below 150 °C was attributed to the evaporation of both solvent and organic molecule incorporated into the ZTO solution. The rapid weight loss above 200 °C was attributed to the decomposition of ZnCl₂ and SnCl₂, which completes at ~ 400 °C. Therefore, dense ZTO films form at annealing temperatures higher than 400 °C. Figure 4.2 shows the XRD patterns of the ZTO films annealed at 300 ~ 600 °C. No sharp peak is observed, except for the (311) plane at 54.5° from the Si substrate, indicating that all the annealed films are amorphous. As the annealing temperature increased, the broad hump near 34° emerges slightly. In ZTO systems, trigonal-ilmenite ZnSnO₃ was reported to form at relative low temperatures (< 600 °C), whereas cubic-spinel Zn₂SnO₄ is formed at high temperatures (> 1000 °C) [90]. Therefore, the broad peak at 34° was assigned to the (110) diffraction of ZnSnO₃, which is the characteristic of the amorphous phase reported previously [79]. The amorphous phase nature of spin-coated ZTO films was confirmed by TEM, as shown in Fig. 4.3(a). The amorphous hollow pattern for 300°C-annealed ZTO film is clearly observed in the selected area diffraction pattern (SADP), as shown in inset of Fig. 4.3(a).

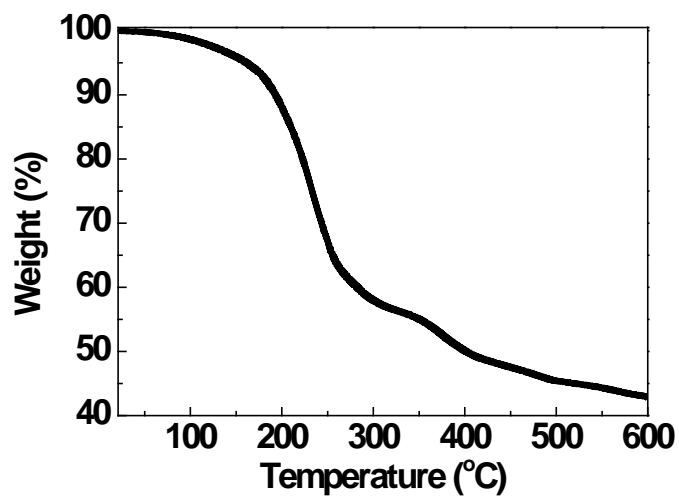


Fig. 4.1. TGA of the ZTO precursor solution at 5 °C min⁻¹ heating rate in air.

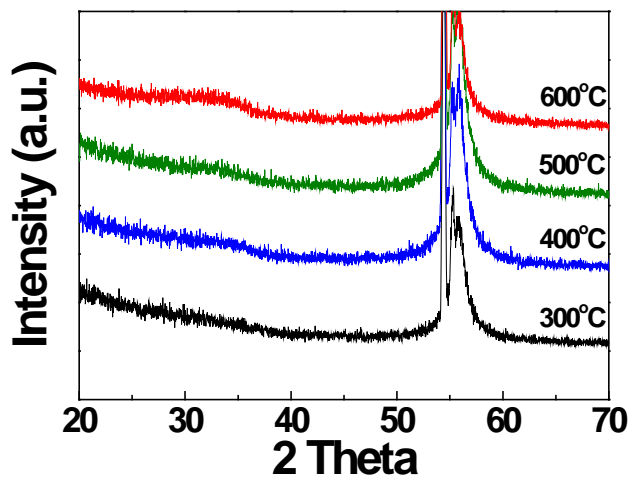


Fig. 4.2. XRD patterns of the ZTO thin films annealed at various Temperatures.

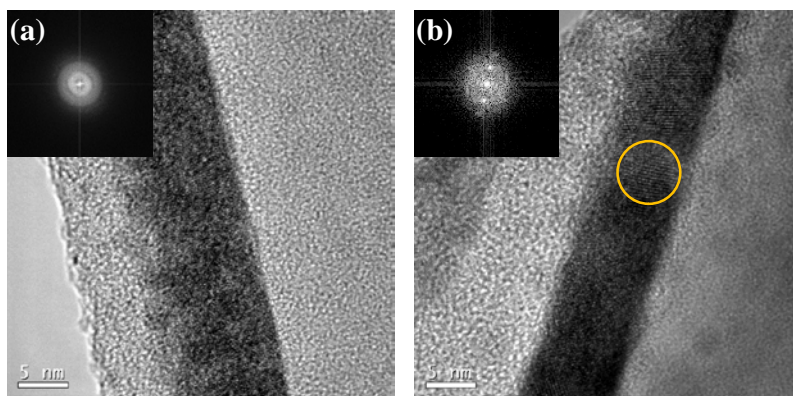


Fig. 4.3. High resolution TEM images of ZTO thin films annealed at (a) 300 and (b) 600 °C.

In contrast, the ZTO film annealed at 600 °C showed a locally crystallized portion in amorphous matrix, as shown in Fig. 4.3(b). The volume fraction of crystallized region to the amorphous ZTO matrix was estimated to be 30 ~ 40%. Figure 4.4 shows AFM images of the ZTO films at various annealing temperatures ranging from 300 to 600 °C. The surface morphology of the 300°C-annealed ZTO film is rather rough, but the ZTO film annealed at 400 °C is much smoother. The rms roughness of the 400°C-annealed ZTO film was 0.18 nm, which is much lower than 0.37 nm of the 300°C-annealed film. Because the film density of the channel layer plays an important role in affecting the device performance and reliability, the densities of various ZTO thin films were evaluated by high-resolution XRR [91]. Figure 4.5 shows the XRR data for the ZTO films prepared at different annealing temperatures. The critical angle for total external reflection for the 600°C-annealed ZTO film is higher than that for the 300°C-annealed sample, indicating that the ZTO film annealed at 600 °C is denser than 300°C-annealed one (inset of Figure 4.5). The density of the ZTO films increased monotonously with increasing annealing temperature. The 300°C-annealed sample had a density of 3.89 g/cm³, whereas the density of the ZTO films annealed at 400, 500, and 600 °C increased to 4.30, 4.55, and 5.38 g/cm³, respectively, as summarized in Table 4.1. The cation composition of the ZTO thin films remained unchanged with the annealing temperature (see Table 4.1).

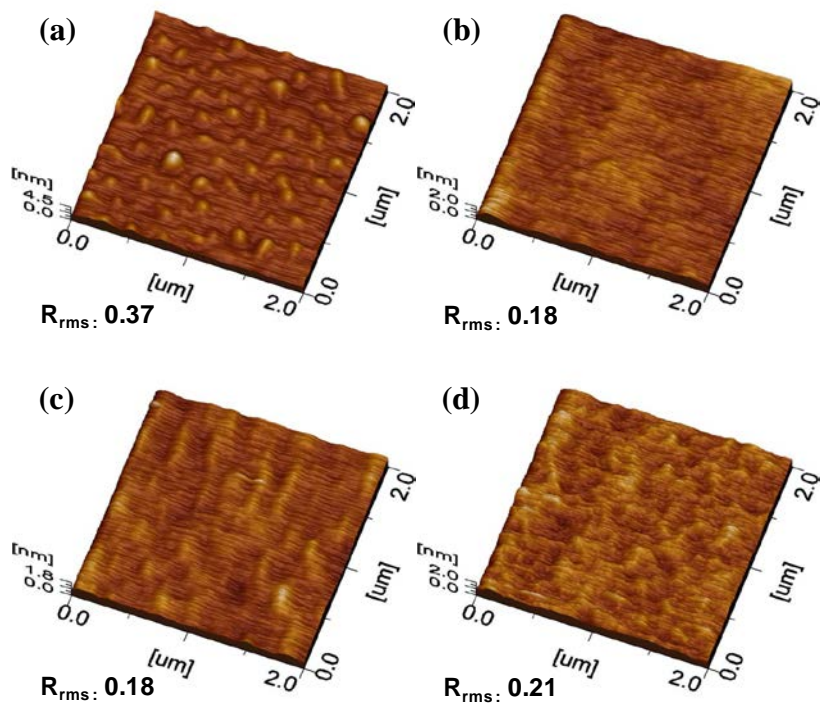


Fig. 4.4. AFM images of the ZTO annealed at (a) 300, (b) 400, (c) 500, and (d) 600 °C.

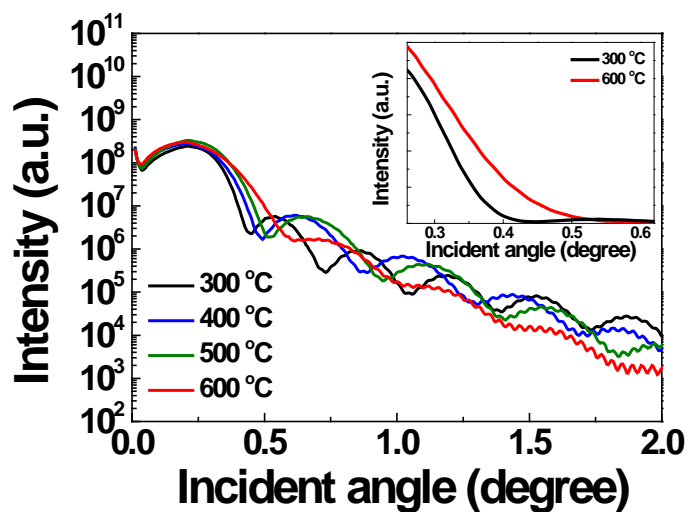


Fig. 4.5. XRR data for the ZTO films prepared at various annealing temperatures.

Table 4.1. Roughness, density, thickness and cation composition of a-ZTO thin films as a function of the annealing temperature.

Annealing temperature (°C)	Rms (nm)	Density (g/cm ³)	Thickness (nm)	Zn/(Zn+Sn)
300	0.37	3.89	8.83	0.49
400	0.18	4.30	6.84	0.51
500	0.18	4.55	6.30	0.51
600	0.20	5.38	6.65	0.51

Figure 4.6 shows the O 1s XPS spectra of the ZTO films annealed at 300 - 600 °C. The C 1s peak for C-C bonds was assigned to 284.5 eV to calibrate the photoelectron binding energy. The O 1s peak was deconvoluted into three peaks at 530.2, 531.2, and 531.9 eV. The O 1s peaks centered at 530.2 and 531.2 eV were assigned to oxygen atoms in the oxide lattice without and with oxygen vacancies, respectively. The peak at 531.9 eV was assigned to impurity-related oxygen, such as carbon and hydroxyl groups [92]. The area ratio of the peaks was used to estimate the relative quantities of the oxygen lattice, oxygen vacancy, and hydroxyl group, as summarized in Table 4.2. The relative areas of the hydroxyl group-related peak and the oxygen vacancy-related peak were reduced monotonically with increasing the annealing temperature, as shown in Figure 6 and summarized in Table 4.2. In contrast, the relative area of the oxygen lattice peak increased with increasing the annealing temperature.

Figure 4.7 shows the Cl 2p XPS spectra of the ZTO films at different annealing temperatures. The Cl 2p XPS spectra of all ZTO films show the coexistence of compounds, such as $ZnCl_n$ and $SnCl_n$. The concentration of Cl incorporated in the ZTO films decreased with increasing the annealing temperature. The 300°C-annealed ZTO film contained the largest concentrations of chlorine and hydroxyl groups (see Table 4.2). The incomplete decomposition of organic ligands and metal salts due to low annealing temperature is believed to cause the excessive

incorporation of Cl ions and OH groups. In addition, the 300°C-annealed ZTO films contain some pores or micro-voids, as inferred from the rough surface and the lowest film density (3.89 g/cm³). As the annealing temperature was increased, such impurities were reduced substantially with the enhanced decomposition and evaporation. Simultaneously, the hydroxyl groups (M-OH) were converted to oxides. As a result, the ZTO film became denser and the surface morphology improved with increasing annealing temperature.

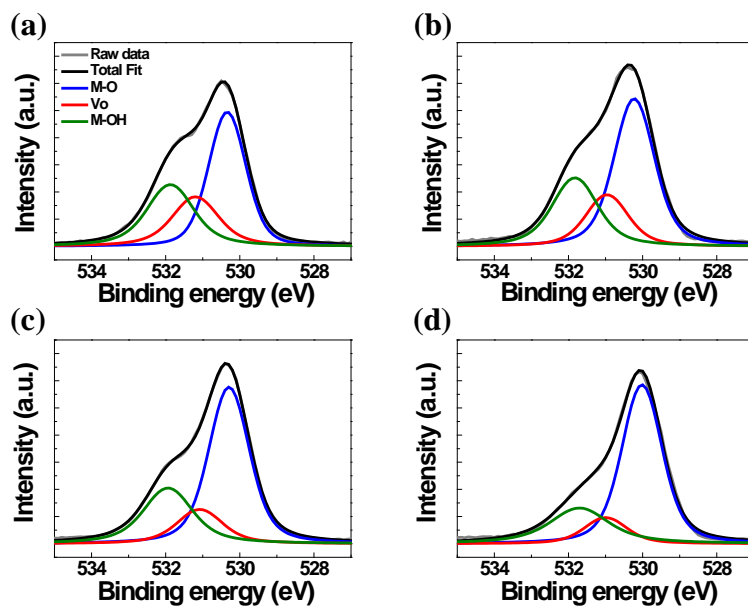


Fig. 4.6. O 1s XPS spectra of the ZTO films annealed at (a) 300, (b) 400, (c) 500, and (d) 600 °C.

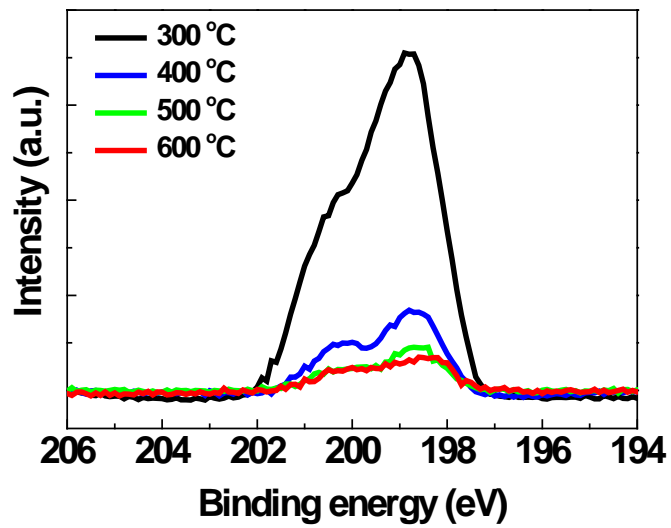


Fig. 4.7. Cl 2p XPS spectra of the ZTO films at various annealing temperatures.

Table 4.2. XPS O 1s result for the annealed ZTO thin films.

Annealing temperature (°C)	O 1s peak [eV]		
	Lattice oxygen [O _l] (530.2 ± 0.16)	Oxygen deficient [V _o] (531.2 ± 0.11)	Hydroxyl (531.9 ± 0.12)
300	0.475	0.233	0.292
400	0.530	0.188	0.282
500	0.587	0.150	0.263
600	0.654	0.116	0.229

4.1.4. Electrical properties of ZTO TFTs

The dependence of transfer characteristics ($I_{DS} - V_{GS}$) of the ZTO TFTs on the annealing temperature was examined. Figure 4.8 shows the representative transfer characteristics of the ZTO TFTs as a function of the annealing temperature. The field-effect mobility (μ_{FE}) was determined from the incremental slope of the $I_{DS}^{1/2}$ vs. V_{GS} plot in the saturation region using the following equation:

$$I_{DS} = (WC_i/2L)\mu_{FE}(V_{GS} - V_{th})^2V_{DS}, \quad (\text{Eq.4.1})$$

where L is the channel length, W is the width, and C_i is the gate capacitance per unit area. The V_{th} was defined as the gate voltage that induces a drain current of $L/W \times 10$ nA at $V_{DS} = 10.1$ V. The subthreshold gate swing ($SS = dV_{GS}/d\log I_{DS}$ [V/decade]) was extracted from the linear part of the $\log(I_{DS})$ vs. V_{GS} plot. The 300 °C-annealed ZTO TFTs showed marginal performance: the μ_{FE} , SS , and $I_{on/off}$ ratio were 0.1 cm²/Vs, 1.84 V/decade, and 3.1×10^5 , respectively. In contrast, the 400°C-annealed device exhibited reasonable transistor behavior. The μ_{FE} , V_{th} , SS , and $I_{on/off}$ ratio of the ZTO TFT annealed at 400 °C were 3.5 cm²/Vs, 1.1 V, 0.36 V/decade, and 1.4×10^7 , respectively, as listed in Table 3. Significant improvement in the device performance was observed for the ZTO TFTs annealed

at 500 °C. The μ_{FE} and SS values for the 500 °C-annealed device were improved to 6.0 cm²/Vs and 0.28 V/decade, respectively. Moreover, the V_{th} value was reduced to nearly zero voltage (0.6 V) and the $I_{on/off}$ ratio was increased to 4.0×10^7 , which is desirable for low power consumption of active matrix electronics. Further increase in the annealing temperature to 600 °C resulted in a higher μ_{FE} of 7.8 cm²/Vs and a lower SS of 0.25 V/decade. On the other hand, the V_{th} value deteriorated slightly to 0.11 V.

The SS value of a given TFT device is related to the total density of traps, including the bulk (N_{SS}) and semiconductor-insulator interfacial traps (D_{it}), according to the following equation [93]:

$$SS = \frac{qk_B T(N_{SS}t_{ch} + D_{it})}{C_i \log(e)} \quad (\text{Eq. 4.2})$$

where q is the electron charge, k_B is Boltzmann's constant, T is the absolute temperature, and t_{ch} is the channel layer thickness. N_{SS} and D_{it} in the ZTO TFTs were calculated by setting one of parameters to zero. In this study, the N_{SS} and D_{it} values correspond to the maximum trap density formed in a given system. The $N_{SS,max}$ values for the 300-, 400-, 500-, and 600 °C-annealed devices were 7.2×10^{18} , 1.8×10^{18} , 1.6×10^{18} , and 1.4×10^{18} cm⁻²eV⁻¹, respectively (see Table 4.3). This result suggests that higher annealing temperature can reduce the total trap density

of the ZTO semiconductor and interfaces significantly.

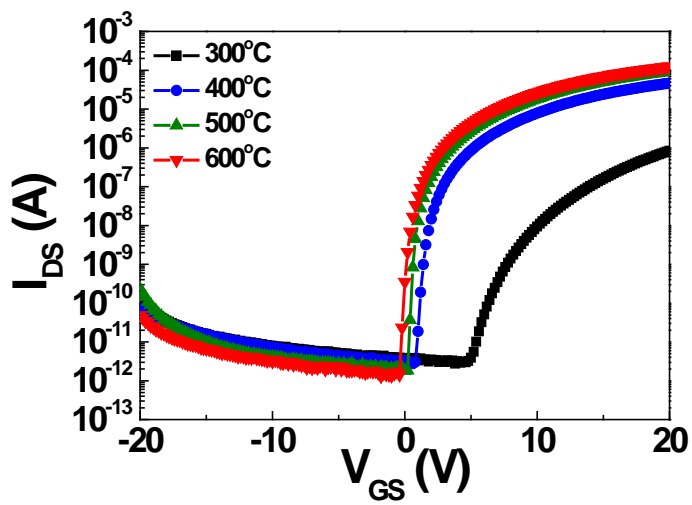


Fig. 4.8. Representative transfer characteristics of the ZTO TFTs annealed at various temperatures.

Table 4.3. Comparison of the device parameters including μ_{FE} , SS, V_{th} , $I_{on/off}$, $D_{it,max}$, and $N_{ss,max}$ of the various ZTO TFTs.

Annealing temperature (°C)	μ_{FE} (cm ² /Vs)	SS (V/decade)	V_{th} (V)	$I_{on/off}$	$D_{it,max}$ (eV ⁻¹ cm ⁻²)	$N_{ss,max}$ (eV ⁻¹ cm ⁻²)
300	0.1	1.84	7.34	3.1 x 10 ⁵	6.4 x 10 ¹²	7.2 x 10 ¹⁸
400	3.5	0.36	1.10	1.4 x 10 ⁷	1.2 x 10 ¹²	1.8 x 10 ¹⁸
500	6.0	0.28	0.58	4.0 x 10 ⁷	9.7 x 10 ¹¹	1.6 x 10 ¹⁸
600	7.8	0.25	0.11	1.0 x 10 ⁸	8.7 x 10 ¹¹	1.4 x 10 ¹⁸

4.1.5. NBS and NBIS instability of ZTO TFTs

The effects of annealing temperature on the dark NBS instability of the resulting ZTO transistors were investigated. The devices were stressed under the following conditions: V_{GS} and V_{DS} at -20 and 10.1 V, respectively at room temperature and stress duration of 4000 s. Figure 4.9 shows the evolution of the transfer characteristics of the various ZTO TFTs as a function of the NBS time. A parallel V_{th} shift by -1.8 V after NBS was observed for the 300°C-annealed device without a significant change in SS value, suggesting that V_{th} degradation originates from charge trapping rather than the creation of defects within the ZTO semiconductor. Higher temperature annealing of ZTO films improved the NBS stability of the resulting TFTs. The V_{th} shifts for 400, 500, and 600°C-annealed devices were reduced to -0.60, -0.45, and -0.21 V, respectively. For a better understanding of NBS induced charge trapping, the relaxation times for all devices were extracted using the following stretched-exponential formula [94]:

$$\Delta V_{th}(t) = V_0 \left\{ 1 - \exp \left[- \left(\frac{t}{\tau} \right)^\beta \right] \right\}, \quad V_0 = V_g - V_{th,0} \quad (\text{Eq.4.3})$$

where t is the time, τ is the relaxation time constant, β is the dispersion parameter, and $V_{th,0}$ is V_{th} before stress. Figure 10 shows the time dependence of

ΔV_{th} for all the devices, which were fitted to a stretched-exponential equation. For the 300°C-annealed device, τ and β were 4.3×10^5 s and 0.50, respectively, as shown in Fig. 4.10 and Table 4.4. The β values (0.50 ~ 0.55) of all devices were independent of the annealing temperature, suggesting that the charge trapping mechanism responsible for the negative V_{th} shift is identical. On the other hand, the τ values for the ZTO TFTs increased dramatically with increasing the annealing temperature, as shown in Fig. 4.10 and Table 4.4. For example, the relaxation time for the 500°C-annealed device was 9.0×10^6 s, which is one order of magnitude higher than that of the 300°C-annealed device. The light-enhanced NBS instability is a critical issue, as mentioned earlier, because the optoelectronic devices including the transparent display are inevitably exposed to light illumination. Therefore, the NBIS instability of the soluble ZTO TFTs was also examined. The ZTO channel was irradiated with light (~ 2.0 mW/cm²) at a wavelength of ~ 500 nm, which was filtered from a white-light halogen lamp. The applied V_{GS} and V_{DS} stress were identical to the dark NBS condition. Figure 4.11 shows the evolution of the transfer characteristics as a function of the NBIS time for various ZTO TFTs. Light illumination of the ZTO channel region further accelerates the NBS-induced V_{th} shift. The 300°C-annealed device suffered from a huge V_{th} shift of -10.5 V (Fig. 4.11(a)). A similar trend was observed in that the NBIS instability of the ZTO TFTs also decreased with increasing the annealing temperature.

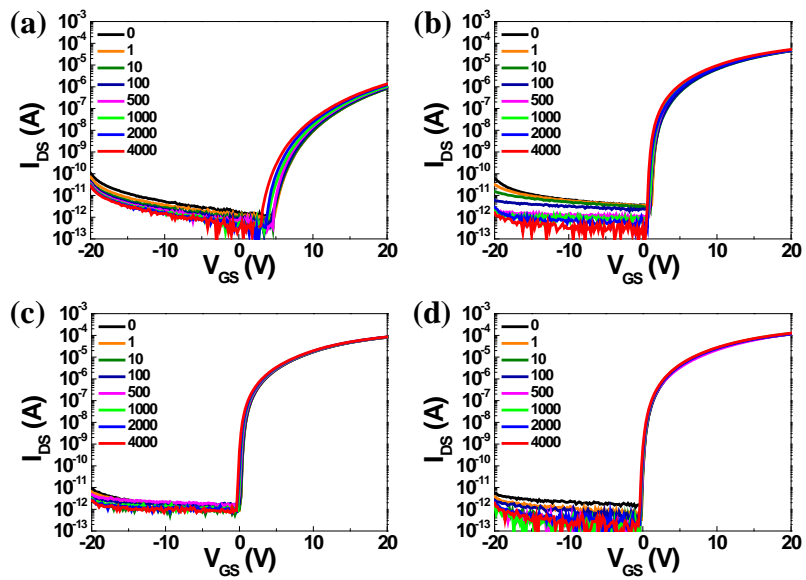


Fig. 4.9. Evolution of the transfer characteristics of ZTO annealed at (a) 300, (b) 400, (c) 500, and (d) 600 °C as a function of the dark NBS time.

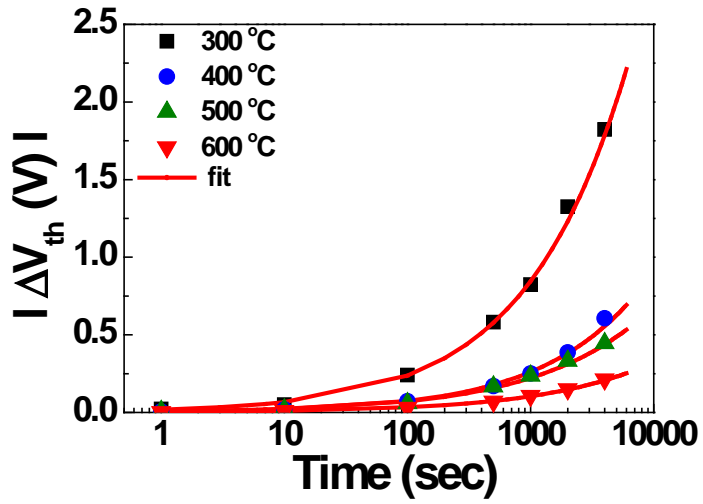


Fig. 4.10. Dark NBS time dependence of ΔV_{th} for the various ZTO TFTs. The measured data was fitted to a stretched-exponential equation with fitting parameter of τ and β .

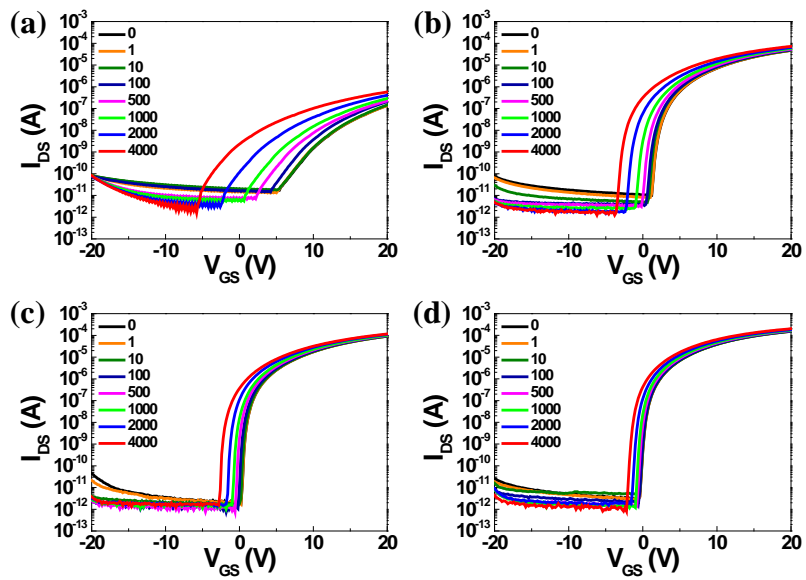


Fig. 4.11. Evolution of the transfer characteristics of ZTO annealed at (a) 300, (b) 400, (c) 500, and (d) 600 °C as a function of the NBIS time.

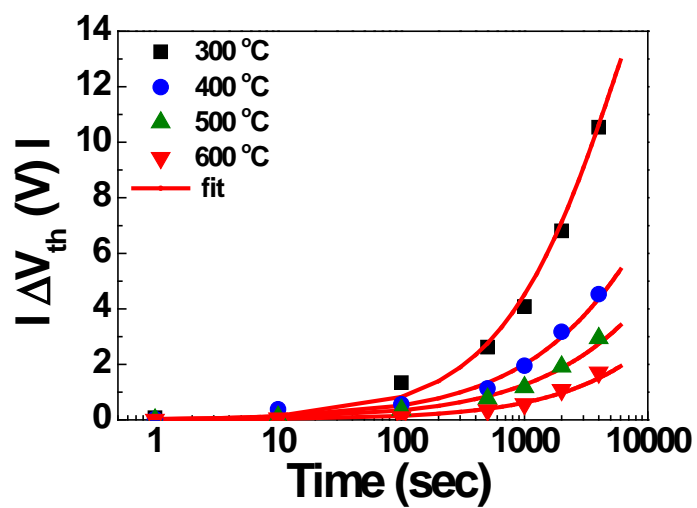


Fig. 4.12. NBIS time dependence of ΔV_{th} for the various ZTO TFTs.

Table 4.4. Comparison of the relaxation time (τ) and dispersion parameter (β) at room temperature for the various ZTO TFTs.

Stress condition	Annealing temperature (°C)	τ @ RT (s)	$\square\square\beta$
NBS	300	4.3×10^5	0.50
	400	2.6×10^6	0.55
	500	9.0×10^6	0.49
	600	4.1×10^7	0.49
NBIS	300	5.7×10^3	0.78
	400	4.0×10^4	0.61
	500	1.1×10^5	0.59
	600	2.0×10^5	0.65

Therefore, a negative V_{th} shift was diminished significantly to 4.5 V for the ZTO TFT annealed at 400 °C (Fig. 4.11(b)). The photo-bias stability was improved further by higher temperature annealing of 500 and 600 °C: the devices showed a negative V_{th} displacement of only 2.9 and 1.7 V shift, respectively (Fig. 4.11(c) and (d)). To obtain insight into the V_{th} degradation mechanism by NBIS, the τ and β values were extracted for the NBIS time-dependent V_{th} instability using the same stretched-exponential formula, as shown in Fig. 4.12. The β values (0.59 ~ 0.78) extracted for NBIS instability were higher than those for NBS instability and the relaxation times were reduced significantly to $5.6 \times 10^3 \sim 2.0 \times 10^5$ s, as summarized in Table 4.4. This suggests that the NBS and NBIS instability have different physical origins.

The negative V_{th} shift in the NBIS condition can be attributed to (1) photo-ionization of pre-existing neutral oxygen vacancy [71, 95], (2) trapping of photo-created hole carriers [68], and (3) ambient interaction [72]. The latter mechanism of (3) can be excluded because the ZTO channel layers were encapsulated by PMMA. In the oxygen vacancy model, the two electrons can be photo-excited from neutral oxygen vacancies in the conduction band [$V_O \rightarrow V_O^{2+} + 2e^-$], leading to a negative V_{th} shift [so-called persistent photo-conductivity (PPC)]. According to the electronic calculation, the V_O^{2+} state in ZnO-based materials is preferred to over V_O state due to its low formation energy when Fermi energy is near the valence band

maximum [96]. Therefore, the transition from V_O to V_O^{2+} can be also caused by lowering of the quasi Fermi energy, which corresponds to the application of NBS to TFTs. Or the migration of positively charged oxygen vacancy by negative bias applied to the gate electrode can induce negative free carriers in the channel, leading to the same negative V_{th} shift [73]. Therefore, the oxygen vacancy-related model is responsible for the dark NBS and NBIS induced degradation. Obviously, the V_{th} deterioration accelerated by NBIS originates from the additional photo-ionization process of neutral V_O defects.

The trapping of photo-created hole carriers also plays an important role in the NBIS condition. During the NBIS condition, electron-hole pairs in the channel region are generated by light. The photo-created hole carriers move toward the gate dielectric by the NBS and become trapped at the interfacial trap states, causing a negative V_{th} shift [68]. However, this is not the case for dark NBS condition because the number of existing hole carriers under dark NBS condition would be extremely small due to a huge sub-gap density of states (10^{20} cm^{-3}) near the valence band of ZnO-based material [10]. This disparity can result in different β values between NBS and NBIS instability. The strong annealing temperature dependence on the NBS and NBIS instability of the ZTO TFTs can be understood based on the mechanisms discussed. The inferior instability of the 300°C-annealed device is related to the concentration of largest V_O and impurities in the ZTO channel layer

(Figs. 4.6 and 4.7). The negative V_{th} shift is enhanced by the PPC effect because V_O defects are potential donors. Or hole carrier trapping can be also responsible for this deterioration. The V_{th} instability by the hole carrier trapping is proportional to the number of holes generated by the applied bias and the number of trapping sites. The 300°C-annealed ZTO channel showed the largest level of OH and Cl incorporation. This contamination may act as a generation center for hole carriers upon photon irradiation into the ZTO channel region. A similar adverse effect of Cl incorporation in the channel layer was also reported for vacuum-derived metal oxide TFTs [97]. Therefore, the inferior stability of the 300°C-annealed device is attributed to large amount of impurities and oxygen vacancy in the ZTO film as confirmed by XPS and XRR results. The improvement in the photo-bias stability of the ZTO TFTs annealed at 400 and 500 °C was attributed to the reduced oxygen vacancies and higher purity in the channel layer. Similar results were reported, which supports this observation [76, 98]. The 600°C-annealed device exhibited the best performance and reliability, which is consistent with its lowest V_O and impurity concentration. On the other hand, the partial crystallization of channel layer at 600 °C can be also partially responsible for this improvement because the crystalline ZTO film has the lower distribution of tail states in the forbidden band gap. For practical application, an annealing temperature less than 500 °C is desirable considering the softening point of the glass substrate.

Finally, it is important to discuss how the annealing temperature can be lowered ($< 250\text{ }^{\circ}\text{C}$) to make it compatible with plastic substrates. To obtain a high quality film at low temperature, advanced annealing processes, such as high pressure oxygen annealing [99] or photo annealing [92], can be viable approaches since they effectively reduce the structural impurities in the channel layer and facilitate film densification at low temperature.

4.1.6. Summary

The effect of the annealing temperature on the device performance and photo bias instability of solution-processed ZTO TFTs was studied. Device performance of the ZTO TFTs was improved by increasing the annealing temperature. The 500°C-annealed device exhibited a high μ_{FE} , low SS , V_{th} , and good $I_{on/off}$ ratio of 6.0 cm^2/Vs , 0.28 V/decade, 0.6 V, and 4.0×10^7 , respectively whereas the 300°C-annealed ZTO TFTs showed marginal performance: the μ_{FE} , SS , and $I_{on/off}$ ratio were 0.1 cm^2/Vs , 1.84 V/decade, and 3.1×10^5 , respectively. The dark NBS and NBIS instability for the ZTO TFTs depend strongly on the annealing temperature. The strong suppression of NBIS instability was also observed for the 500°C-annealed ZTO device. The ΔV_{th} of the 500°C-annealed ZTO device after the application of NBIS was reduced substantially from 10.5 V for the 300°C-annealed device to 2.9 V. The dynamics of V_{th} shift with NBS and NBIS time for all ZTO TFTs was analyzed based on the stretched exponential relaxation to improve the understanding of stress time-dependent charge trapping. The τ values extracted from the 300°C-annealed device under NBS and NBIS condition were 4.3×10^5 and 5.7×10^3 , respectively. In contrast, the 500°C-annealed device exhibited τ values of 9.0×10^6 and 1.1×10^5 , under NBS and NBIS condition, respectively. This improvement can be explained by the photo-created hole trapping model and

V_O transition model. In-depth analyses of the structural and chemical properties of ZTO films revealed that the purification and densification of the solution-processed ZTO channel layer are critical factors for high performance oxide TFTs with excellent photo-bias stability.

4.2 Impact of the cation composition on the electrical performance and photo-bias stability

4.2.1. Introduction

Metal-oxide (MO) thin-film transistors (TFTs) have attracted considerable interest as a strong candidate for realizing flexible, transparent, large-area, low-cost electronic devices including active-matrix liquid crystal displays (LCDs), organic-light emitting diodes (OLEDs), electron paper and smart identification cards. These emerging applications are enabled by the promising properties of oxide-based TFTs, including high mobility, good transparency, low processing temperature, and reasonable stability compared to amorphous silicon TFTs [1]. MO TFTs are fabricated mainly using vacuum-based deposition processes, such as magnetron sputtering [100], pulsed laser deposition (PLD) [101], and atomic layer deposition (ALD) [102]. Most vacuum-based processes, however, are expected to have some problems in obtaining the compatibility with very large flat panel displays because of the very high cost of fabrication. Solution-based processes have become a viable alternative to vacuum-based processes because they offer process simplicity, low manufacturing cost and potentially high throughput [103, 104].

The most researched thin film material for TFT applications is InGaZnO_4

(IGZO), which has a high carrier (electron) mobility (μ_e) ($> 10 \text{ cm}^2\text{V}^{-1}\text{s}^{-1}$), even in an amorphous material, which is generally not the case for other materials, such as amorphous Si ($\mu_e < 1 \text{ cm}^2\text{V}^{-1}\text{s}^{-1}$). In addition, high quality TFTs with amorphous IGZO can be prepared using a simple sputtering process, even at room temperature with a minimal post-deposition thermal budget [100]. According to these primary merits of IGZO, ultra-high-resolution LCDs and large-area OLED products adopting IGZO-TFTs are commercially available [67]. The high overlap of indium $5s$ orbitals, which mainly constitute the conduction band of the amorphous IGZO network, and their non-directionality are responsible for the high μ_e of in this material [1, 105]. In plays the role as a carrier concentration and mobility enhancer, whereas Ga generally plays the opposite role. This can be attributed to the weak and strong binding of In-O bonds and Ga-O bonds, respectively. Therefore, appropriate control of the In/Ga ratio is the most critical parameter for achieving the desired properties from the IGZO-TFTs [106, 107]. Nevertheless, the complicated composition of IGZO makes precise control of the composition and oxygen stoichiometry over a very large area difficult, which is further aggravated by the relatively high volatility of In. Zinc tin oxide ($\text{Zn}_x\text{Sn}_{1-x}\text{O}_{2-x}$) has recently gained attention for use as a channel layer in MO TFTs due to the almost identical μ_e level of amorphous ZTO films to that of IGZO films, which can be achieved routinely by sputtering [108], metal-organic chemical vapor deposition [109] and

ALD [77]. The Sn5s orbital in ZTO plays a similar role to that of the In5s orbital in IGZO [39]. Therefore, many studies have reported the effects of the chemical precursor, composition and annealing temperature of ZTO-based films. The transport properties of the resulting ZTO-based TFT devices have also been reported [75, 80, 110-114]. The solution-based process of ZTO films is desirable for the mass-production of large area devices. Jeong et al., reported the effects of the incorporated Sn-concentration on the transfer characteristics of solution-processed ZTO TFTs [80]. The μ_e and off-state current of the ZTO TFTs increased with increasing Sn-concentration, which was attributed to the donor-like behavior of Sn atoms in a semiconducting ZTO film. Kim et al. examined the effects of the Sn-concentration on the drain current – gate voltage ($I_{DS} - V_{GS}$) performance and electrical stability of solution-processed ZTO TFTs under dark conditions [112]. They reported that the dark condition stability of the TFTs degraded with decreasing Sn-concentration. This instability was attributed to the electric-field induced oxygen adsorption from the air ambient to the back surface of the ZTO film, which modifies the carrier concentration in the channel layer. Such oxygen adsorption was believed to be enhanced when the Zn-concentration was high (Sn-concentration was low) due to the higher oxidation potential of Zn than Sn. On the other hand, these studies did not provide any direct information on the donor-like behavior of Sn in the ZTO material. In addition, very little is known regarding the

influence of the Sn-concentration on the photo-bias instability of ZTO TFTs, even though the light-induced instability of MO TFTs is a technically important issue [67].

This study examined the effects of the Sn-concentration on the various physical properties of the ZTO films, as well as the accompanying transport properties and photo-bias instability of solution-processed ZTO TFTs. The structural and chemical properties of ZTO films were strongly dependent on the Sn-concentration. The ZTO films with Zn-rich and Sn-rich compositions crystallized with the wurtzite and rutile structures, respectively, after annealing at 450 °C for 1 hr in air, whereas the ZTO films with a Sn/Zn ratio ~ 1 maintained the amorphous structure. The Sn in a ZTO film with a Zn-rich composition was identified as a carrier generator (donor center). In contrast, the Zn atoms in the rutile-structured ZTO films with a Sn-rich composition work as an acceptor center. The optimal photo-bias stability of the ZTO TFTs was determined from the microstructure of the ZTO film rather than from the chemical defects of ZTO films.

4.2.2. Experimental procedure

The precursor solution was prepared by dissolving zinc acetate [$\text{Zn}(\text{CH}_3\text{COO})_2$, Aldrich] and tin (II) chloride dihydrate [$\text{SnCl}_2 \cdot 2\text{H}_2\text{O}$, Aldrich], respectively, in 2-methoxy ethanol solvent. The total concentration of the metal precursor in the solution was fixed to 0.3 M, and the molar ratio of $\text{Sn}/[\text{Zn}+\text{Sn}]$ was varied from 0.2 to 0.9. The precursor solution was stirred for 1 hour at 60°C and filtered through a $0.22\ \mu\text{m}$ syringe filter before spin coating. Heavily-doped *p*-type Si and a 100-nm-thick thermally grown SiO_2 layer were used as a substrate and a gate, respectively. The substrate was cleaned sequentially with acetone, isopropanol and de-ionized water for 10 min, followed by exposure to ultraviolet light and ozone for 20 min to produce a hydrophilic surface. The ZTO solutions were spin-coated at 500 rpm for 5 s and then at 2000 rpm for 30 s. The resulting ZTO precursor-film was dried at 150°C for 10 min to evaporate the solvent and then annealed at temperatures at 450°C for 1 hr in air. Tin-doped indium oxide (ITO), as the source and drain electrodes (S/D), was deposited by dc magnetron sputtering and patterned through a metal shadow mask. The width (W) and length (L) of the fabricated device was 1000 and $300\ \mu\text{m}$, respectively. Finally, the fabricated device was encapsulated with polymethyl methacrylate (PMMA, MicroChem A4) to prevent dynamic interactions between the channel layer and ambient oxygen/moisture.

4.2.3. Structural and chemical properties of ZTO thin films

Figure 4.13 shows the GIXRD patterns of the ZTO films with various Sn-concentrations. The ZTO film with an Sn/[Zn+Sn] ratio of 0.16 has a sharp peak at 2θ of 34.35° except for the (311) plane at 54.5° from the Si substrate, indicating that it has a polycrystalline structure with a preferential orientation. Crystalline ZnO has a wurtzite structure, which belongs to the hexagonal system ($P6_3mc$, number 186) [115]. In the case of pure ZnO, the (002) peak was expected to appear at 2θ of $\sim 34.44^\circ$. Therefore, the peak of the ZTO film at an Sn/[Zn+Sn] ratio of 0.16 was assigned to the (002) reflection of wurtzite ZnO. The $\sim 0.09^\circ$ smaller 2θ angle of the (002) reflection for this ZTO film can be explained by the substitutional doping of Sn atoms in ZnO. Sn^{4+} has a larger ionic radius (69 pm for a coordination number of 6) than Zn^{2+} (60 pm for a coordination number of 4). The (002) peak of the ZTO film became broader with increasing Sn-concentration, indicating that the film was either amorphous or partially nanocrystalline. Simultaneously, the position of the (002) peak shifted gradually toward a lower 2θ angle with increasing Sn/[Zn+Sn] ratio up to 0.39, which can also be understood from the higher doping concentration of Sn. At a Sn/[Zn+Sn] ratio of 0.48, the ZTO film showed a completely amorphous phase, which can be inferred from the very broad peaks at ~ 20.7 and 33.5° 2θ . In contrast, the Sn-rich ZTO films ($\text{Sn}/[\text{Zn}+\text{Sn}] \geq 0.59$) showed the

typical diffraction patterns from polycrystalline materials with no preferred growth direction. For example, the ZTO film with a Sn/[Zn+Sn] ratio of 0.88 had three diffraction peaks corresponding to the (110), (101) and (200) reflections of rutile SnO₂. In the Sn-rich region, the intensities of these diffraction peaks increased gradually and the full width at half-maximum (FWHM) decreased with increasing Sn-concentration in the ZTO films. This suggests that the effective grain size of the ZTO film increases with increasing Sn-concentration. The mean crystallite size (*d*) of these samples can be estimated using the FWHM of the (110) peak based on Scherrer's formula [116]:

$$d = \frac{0.9\lambda}{B \cos \theta_B}, \quad (\text{Eq. 4.4})$$

where λ is the X-ray wavelength (1.541 Å, CuK α radiation), θ_B is the Bragg diffraction angle and *B* is the FWHM of (110) peak. The mean crystallite size of the ZTO film increased from 1.64 to 4.59 nm with increasing Sn-concentration from 0.59 to 0.88.

The microstructural evolution of the ZTO thin films as a function of the Sn-concentration was investigated further by HRTEM. Figure 4.14 shows the cross-sectional TEM images of the ZTO films with Sn/[Zn+Sn] ratios of 0.16, 0.48 and 0.77. The ZTO films with a Sn/[Zn+Sn] ratio of 0.48 were amorphous, which can

be also confirmed by the amorphous hollow ring in the selected area diffraction pattern. In contrast, the ZTO films with Sn/[Zn+Sn] ratios of 0.16 and 0.77 showed lattice fringes and the presence of grain boundaries, which is consistent with the GIXRD data.

The chemical states of the ZTO films with different Sn-concentrations were examined by XPS. Figure 4.15 shows the O *1s* XP spectra of the ZTO films with Sn/[Zn+Sn] ratios ranging from 0.16 to 0.66. The photoelectron binding energies were calibrated to the C *1s* peak for the C-C bonds at 284.5 eV. The O *1s* peak was deconvoluted into three peaks at 530.1, 531.2, and 531.9 eV [92, 117]. The O *1s* peaks centered at 530.1 and 531.2 eV were assigned to the lattice oxygen peak without and with oxygen vacancies, respectively. The peak at 531.9 eV was assigned to impurity-related oxygen, such as hydroxyl groups. The relative areas of the oxygen vacancy (V_O)-related peak increased monotonically with increasing Sn/[Sn+Zn] ratio, as shown in Figure 4.15 and Table 4.5. The definition of V_O in amorphous material could be controversial. Therefore, V_O in this work corresponds to the broken bond with metal ions (or less coordinated metal ions) and related local structural distortion. The area of the V_O -related peak area ratio for the ZTO film increased from 11.5 % at a Sn/[Sn+Zn] ratio of 0.16 to 28.4% at a Sn/[Sn+Zn] ratio of 0.77. The figure in Fig. 4.16 shows the variations in the relative area ratio of the V_O -related O *1s* as a function of the Sn-concentration. Because the Sn-O

bond is weaker than the Zn-O bond, V_O formation is enhanced with increasing Sn-concentration in the ZTO film [118, 119]. The role of V_O in the electrical properties of the MO TFTs is controversial. V_O can act as either a shallow donor center or a deep level trap, which depends on the species and coordination number (CN) of cations near the V_O [119]. At a fixed Sn-concentration, the free electron density (n_e) of the ZTO film can be controlled experimentally by adjusting the oxygen ratio [72, 95, 120], suggesting that some of the V_O are indeed shallow donors. Therefore, it is expected that the n_e value of the ZTO film increases with increasing Sn-concentration.

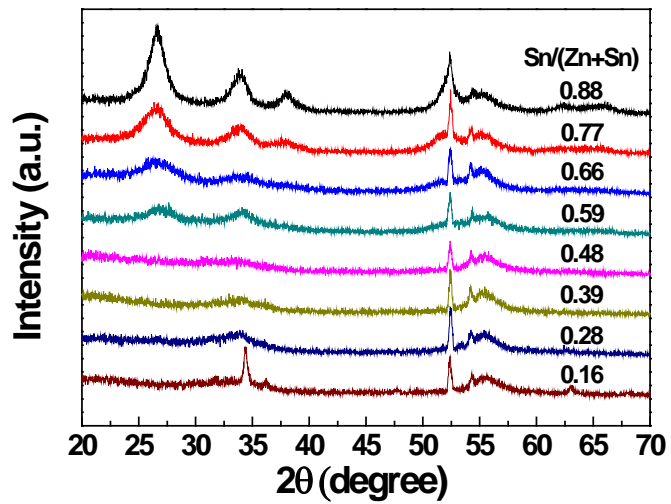


Fig. 4.13. XRD patterns of the ZTO thin films as a function of the incorporated Sn-concentration.

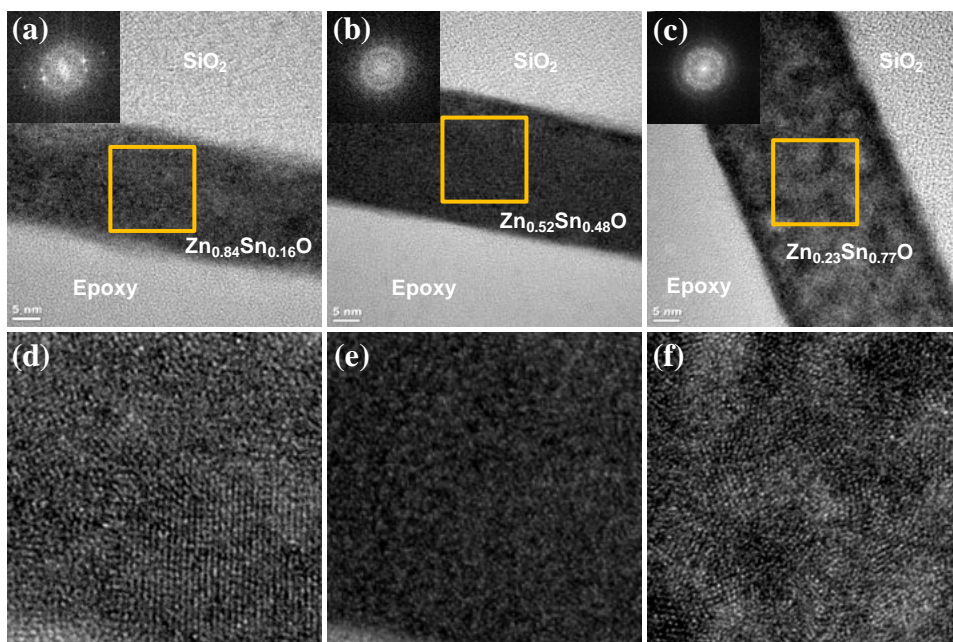


Fig. 4.14. (Upper panels) Cross-section TEM images of ZTO thin films with a Sn/[Zn+Sn] ratio of (a) 0.16, (b) 0.48 and (c) 0.77. Selected area diffraction pattern of each film is inserted in the inset in Fig. 4.14. (Lower panels) High resolution image of ZTO films with a Sn/[Zn+Sn] of (d) 0.16, (e) 0.48 and (f) 0.77.

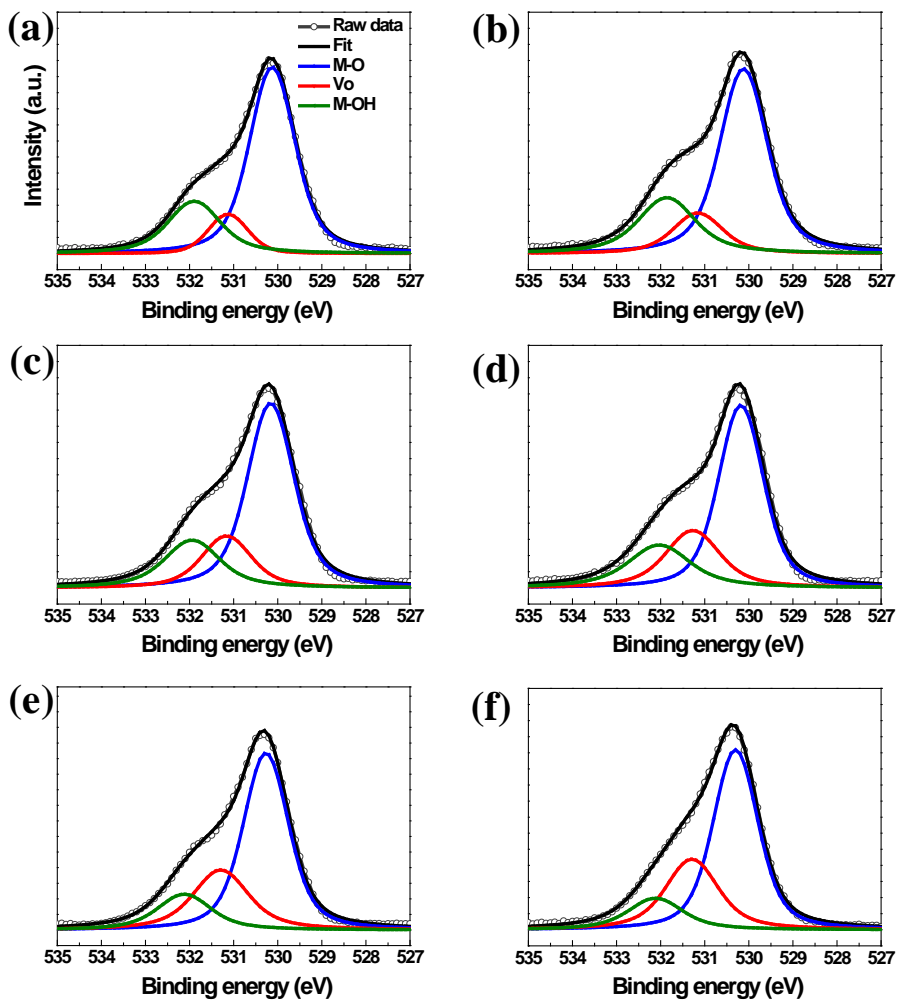


Fig. 4.15. O 1s XPS spectra and their deconvolution results of the ZTO films with a Sn/[Zn+Sn] ratio of (a) 0.16, (b) 0.28, (c) 0.39, (d) 0.48, (e) 0.59 and (f) 0.66. Inset in (a) shows the variation of V_O peak ratio as a function of Sn/[Zn+Sn].

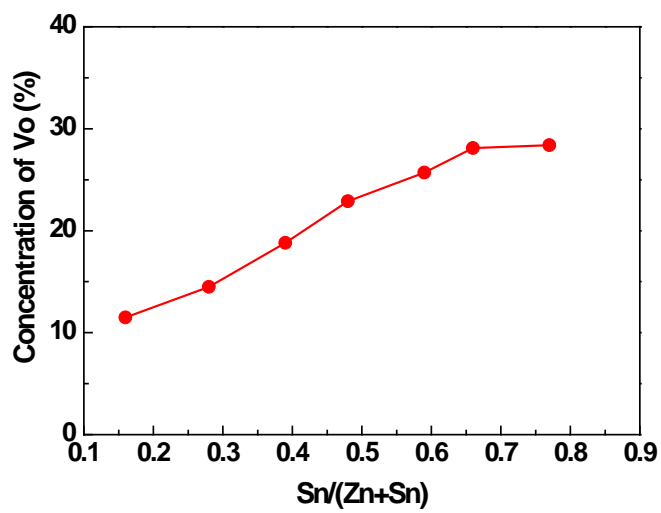


Fig. 4.16. The variation of V_O peak ratio as a function of Sn/[Zn+Sn].

Table 4.5. O 1s peaks deconvoluted from the XP spectra of the various ZTO films with different

Sn/(Zn+Sn) (at. %)	O 1s peak [eV]		
	Lattice oxygen [O _o] (530.1 ± 0.1)	Oxygen deficient [V _o] (531.2 ± 0.1)	Hydroxyl (531.9 ± 0.1)
0.77	0.577	0.284	0.139
0.66	0.588	0.281	0.131
0.59	0.595	0.257	0.148
0.48	0.574	0.229	0.197
0.39	0.616	0.188	0.196
0.28	0.621	0.145	0.234
0.16	0.664	0.115	0.221

4.2.4. Electrical properties of ZTO TFTs

Figure 4.17 shows the change in n_e estimated from the Hall measurements for the ZTO films as a function of the Sn-concentration. n_e increased with increasing Sn-concentration, which is consistent with the aforementioned simple hypothesis. On the other hand, the n_e value of the ZTO film increased ~400 fold (from 2.1×10^{15} to $8.5 \times 10^{17} \text{ cm}^{-3}$) with increasing Sn/[Sn+Zn] ratio from 0.28 to 0.77, whereas the V_O concentration of the ZTO film estimated by XPS increased approximately two fold. This suggests that the ratio of a shallow V_O to a deep V_O depends on the Sn composition. The several tens % of V_O detected by XPS corresponds to a vacancy density in order of $10^{21} - 10^{22} \text{ cm}^{-3}$. Such a high vacancy concentration does not represent the bulk of the film because XPS mostly probes the chemical structure of a defective film surface. Nevertheless, the consistent trend in V_O with the Sn/[Sn+Zn] ratio suggests that the variation in n_e has a relationship with the V_O states. The different energy levels of V_O within the band gap of the ZTO film for different Sn/[Sn+Zn] ratios, rather than its concentration itself, are more responsible for the variation in n_e . The higher V_O concentration, in the film with a high Sn/[Sn+Zn] ratio introduces abundant shallow levels, resulting in a higher n_e . The energy levels of the V_O in the band gap of ZTO could vary according to the chemical environment near V_O . V_O with a higher CN of Sn has a shallow level

compared to V_O with a higher CN of Zn [105, 121]. Therefore, with increasing Sn-concentration, the energy level of V_O in the ZTO film becomes shallower (lower trap depth), resulting in an exponential increase in carrier generation with increasing Sn-concentration, which corroborates the results shown in Fig. 4.13. On the other hand, this interpretation is valid only for the case where the host ZTO maintains an identical crystal (or amorphous) structure throughout the entire Sn-concentration range. As observed by GIXRD and HRTEM, the ZTO films have a ZnO-like wurtzite, amorphous, and SnO₂-like rutile structure, respectively, with increasing Sn-concentration. This suggests that the aforementioned explanation for a higher n_e with increasing Sn-concentration might be valid only for amorphous materials because the CN of an amorphous phase can vary almost linearly with the Sn-concentration. In crystalline materials, the CN of V_O must be restricted by the structure of the specific crystal. Therefore, in crystalline materials, the following explanation must be more reasonable for the variation of n_e with Sn-concentration.

In Sn-deficient ZTO films, the Sn cation can either substitute for the Zn site of wurtzite ZnO crystal or occupy the interstitial site. On the other hand, the interstitial incorporation of Sn would be less likely considering the larger ionic radius of Sn compared to Zn. The peak position shift to a lower 2θ direction with increasing Sn-concentration in Fig. 4.13 suggests that the Sn ions are incorporated mainly via the substitutional form in wurtzite ZTO films. Because a Sn atom has two more valence

electrons than a Zn atom, the substitutionally-doped $Sn_{Zn}^{\circ\circ}$ acts as a donor center in the wurtzite ZTO structure. Therefore, the substitutionally-incorporated Sn ($Sn_{Zn}^{\circ\circ}$) can be partly responsible for the increasing n_e value of the ZTO film with increasing Sn-concentration. Considering that the donor levels in crystalline materials generally have well-defined discrete levels within the band gap, the almost one order of magnitude increase in n_e when the Sn/[Sn+Zn] ratio is increased from 0.28 to 0.39 (Fig. 4.17) cannot be accounted for by substitutional Sn-doping in the mostly wurtzite-structured ZTO film. This suggests that the aforementioned arguments related to the V_O still play a major role in increasing n_e .

In contrast, the ZTO films with a high Sn-concentration had a rutile SnO_2 -like crystal structure, meaning that Zn atoms in this material are impurities. The Zn atom can substitute for the site of Sn in the rutile ZTO film or be present as interstitial ions. The substitutional Zn (Zn_{Sn}'') can act as an acceptor center. On the other hand, Hall measurements showed that these films also have an n-type nature, suggesting that the majority carriers are electrons, which must be produced mainly by V_O formation. The highest Sn-concentration in these ZTO films coincides with the highest tendency of V_O formation due to the weaker Sn-O bonds compared to Zn-O bonds. Therefore, Zn_{Sn}'' decreases the electron concentration by trapping them. Again, the larger decrease in carrier concentration (from 8.5×10^{17} to $3.9 \times 10^{17} \text{ cm}^{-3}$) when the Sn/[Sn+Zn] ratio is decreased from 0.77 to 0.66 (Fig. 4.17)

showed that the major contribution to the carrier concentration is the V_O concentration.

Figure 4.18 shows the representative transfer characteristic curves (I_{DS} vs. V_{GS}) of the ZTO TFTs with different Sn-concentrations when the drain voltage (V_{DS}) was set to 10 V. The field-effect carrier mobility (μ_{FE}) was determined from the slope of the $I_{DS}^{1/2}$ vs. V_{GS} plot using the following equation:

$$I_{DS} = (WC_i/2L)\mu_{FE}(V_{GS} - V_{th})^2, \quad (\text{Eq. 4.1})$$

where L is the channel length, W is the width, and C_i is the gate capacitance per unit area. The threshold voltage (V_{th}) was defined as the gate voltage (V_{GS}) that induces a drain current of $L/W \times 10$ nA at $V_{DS} = 10$ V. The subthreshold swing ($SS = dV_{GS}/d\log I_{DS}$ [V/decade]) was extracted from the linear part of the $\log(I_{DS})$ vs. V_{GS} plot. The fast bulk traps (N_{SS}) and semiconductor-insulator interfacial traps (D_{it}) were calculated using the following equation [93]:

$$SS = \frac{qk_B T(N_{SS}t_{ch} + D_{it})}{C_i \log(e)}, \quad (\text{Eq. 4.2})$$

where q is the electron charge, k_B is Boltzmann's constant, T is the absolute temperature, and t_{ch} is the channel layer thickness. N_{SS} and D_{it} in the ZTO TFTs

were calculated by setting one of parameters to zero. Therefore, the N_{SS} and D_{it} values must be considered the maximum trap density formed in a given system. The carrier transport properties and current modulation capability of the devices were strongly dependent on the Sn-concentration in the channel layer. The TFTs with Sn/[Sn+Zn] ratios of 0.16 and 0.28 commonly showed a low on current (I_{on}) in the highly positive V_{GS} region, whereas the off current (I_{off}) in the negative V_{GS} region was sufficiently low. This is related primarily to the very low carrier concentration (Fig. 4.17) for these cases. The I_{on}/I_{off} ratio was only 4.51×10^5 , μ_{FE} was 0.46 cm^2/Vs , and V_{th} was as high as 8.48 V in the case of Sn/[Sn+Zn] = 0.16 (see Fig. 4.18 and Table 4.6.). With increasing Sn/[Sn+Zn] ratio of up to 0.48, the μ_{FE} , V_{th} , SS and I_{on}/I_{off} ratio values of the device were improved substantially to 4.25 cm^2/Vs , -0.02 V, 0.42 V/decade, and 4.10×10^7 , respectively (Table 4.6.). Generally, the carrier transport in the conduction band of an amorphous ZTO film is dominated by the percolated path composed of Sn 5s orbitals, which must be improved by the higher Sn-concentration in the ZTO film. On the other hand, in amorphous materials, the lower edge of the conduction band is not as clearly defined as that of the crystalline material. The lower edge region of the conduction band in amorphous semiconductor oxides is largely due to localized states, which form a mobility edge [122]. Under this circumstance, the higher carrier concentration is beneficial for achieving a higher apparent μ_{FE} . This is because the localized states

with lower energy levels are filled with some of the carriers first, and the remaining carriers are transported via the states residing relatively far above the mobility edge [5, 106]. Therefore, the enhancement of the device parameters in the Sn-deficient composition range is a reflection of the increasing n_e with increasing Sn doping level, which originates from either the creation of a shallow V_O center or the substitutional n-type doping of Sn (Sn_{Zn}°). When the Sn-concentration was larger than a Sn/[Sn+Zn] ratio of 0.59, the μ_{FE} of the resulting device deteriorated again. For example, the device with a Sn/[Sn+Zn] ratio of 0.66 showed a low μ_{FE} of 3.14 cm^2/Vs , even though its channel layer had a higher n_e of $3.9 \times 10^{17} cm^{-3}$. The Sn-concentration-dependent mobility variation of the solution processed ZTO devices was also observed clearly in the output characteristics (Figs. 4.19 (a) – (f)). The microstructure transition of the ZTO film from the amorphous phase to the polycrystalline state is likely to be responsible for this adverse effect. The two dimensional defect states in the grain boundary of a polycrystalline rutile ZTO film can act as a tailing state below the conduction band minima, which cause the additional scattering of charge carriers, leading to a decrease in μ_{FE} . The TFT with a Sn/[Sn+Zn] ratio $> \sim 0.66$ generally showed high I_{off} in the negative V_{GS} region with highly negatively-shifted V_{th} values. The TFT with the highest Sn/[Sn+Zn] ratio of 0.77 could not be turned off, even with a high negative V_{GS} . This can be attributed to the excessively high carrier concentration and high defect density in these

channel materials.

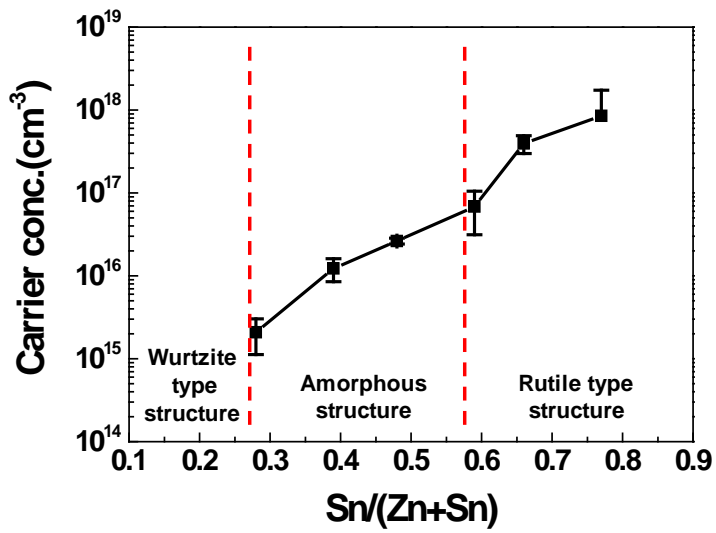


Fig. 4.17. Variation of the carrier density for the ZTO films as a function of the Sn-concentration.

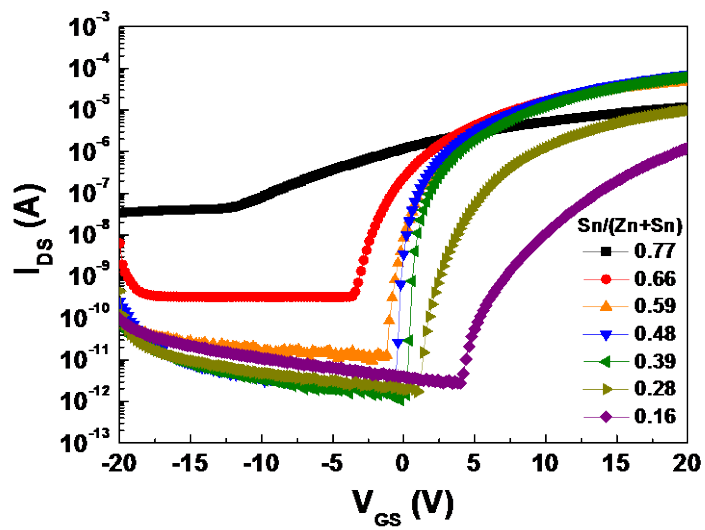


Fig. 4.18. Representative transfer characteristics of the ZTO TFTs for the different Sn-concentrations.

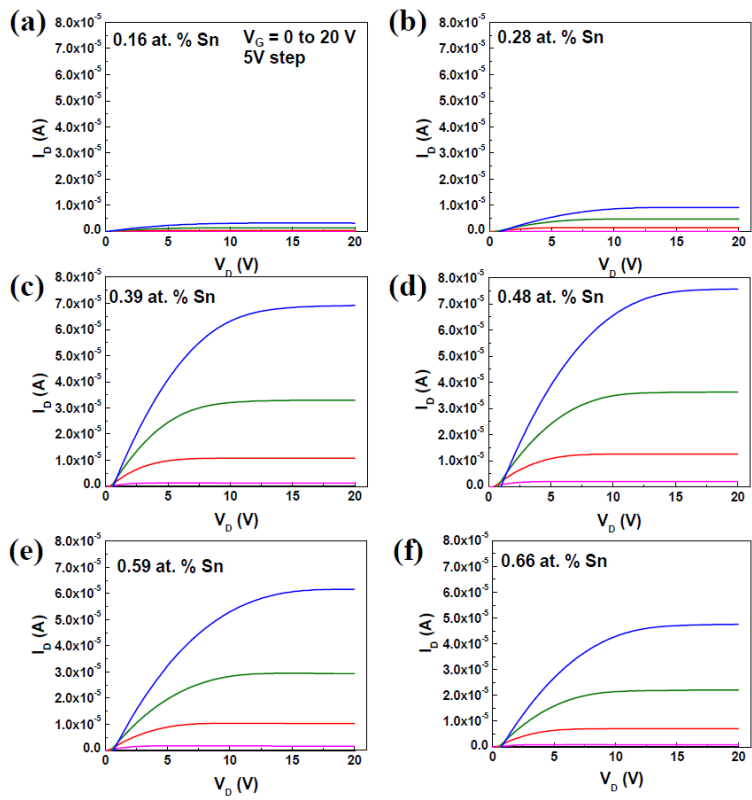


Fig. 4.19. Output characteristics of the ZTO TFTs at a Sn/[Zn+Sn] ratio of (a) 0.16, (b) 0.28, (c) 0.39, (d) 0.48, (e) 0.59 and (f) 0.66.

Table 4.6. Device parameters including μ_{FE} , SS , V_{th} , I_{on}/I_{off} , $D_{it,max}$, $N_{ss,max}$ and ΔV_{th} of the various ZTO TFTs.

Sn /(Zn+Sn)	μ_{FE}	SS	V_{th}	$I_{on/off}$	$D_{it,max}$	$N_{ss,max}$	ΔV_{th}
(at. %)	(cm^2/Vs)	(V/decade)	(V)	($\text{eV}^{-1}\text{cm}^{-2}$)		($\text{eV}^{-1}\text{cm}^{-3}$)	(V)
0.16	0.46	2.75	8.48	4.51×10^5	9.55×10^{12}	3.82×10^{18}	- 3.6
0.28	0.86	1.26	3.10	5.59×10^6	4.37×10^{12}	1.62×10^{18}	- 2.4
0.39	3.98	0.42	0.75	5.93×10^7	1.46×10^{12}	5.60×10^{17}	- 3.0
0.48	4.25	0.42	- 0.02	4.10×10^7	1.45×10^{12}	5.00×10^{17}	- 3.9
0.59	3.29	0.68	- 0.27	5.09×10^6	2.36×10^{12}	7.97×10^{17}	- 6.4
0.66	3.14	1.05	- 2.71	2.02×10^5	3.64×10^{12}	1.08×10^{18}	- 10.3

4.2.5. NBIS instability of ZTO TFTs

Finally, the negative bias illumination stress (NBIS) instability of the solution-processed ZTO TFTs with different Sn-concentrations was examined. The NBIS instability is an important performance measure because the application of MO TFTs in transparent electronics inevitably involves long exposure to light stress on the semiconducting oxide semiconductor films under the negative V_{GS} condition [67]. Figures 4.20 (a) – (f) show the evolution of the transfer curves for the various ZTO TFTs (Sn/[Sn+Zn] ratio from 0.16 to 0.66) for the different NBIS time up to 12,000 s under the following conditions: V_{GS} and V_{DS} of -20 and 10 V, respectively, at room temperature with an illumination power intensity of ~ 2.0 mW/cm² and a wavelength of ~ 500 nm, which was filtered from a white-light halogen lamp. The application of only a negative bias stress without light exposure did not cause substantial degradation. In contrast, the devices exhibited significant instability under the NBIS condition. The NBIS-induced V_{th} variation was dependent on the Sn-concentration in the ZTO film. Figure 4.21 summarizes the variations in V_{th} of the various TFTs as a function of the stress time, and Fig. 4.22 shows the maximum V_{th} variation at a stress time of 12,000 s.

The most desirable NBIS stability was achieved from the TFT with a Sn/[Sn+Zn] ratio of 0.28 (the V_{th} shift was 2.4 V after a 12,000 s stress time), whereas an

increasing or decreasing Sn-concentration degraded it. The degradation in the NBIS stability was considerably more severe when the Sn-concentration was higher (V_{th} shift was 10.3 V after a 12,000 s stress time).

The NBIS induced V_{th} instability of the MO TFTs was attributed to photo-created hole trapping [68], the photo-transition of V_O and subsequent drift of ionized V_O [71], or the photo-desorption of oxygen molecules on the back surface [72]. The latter mechanism can be excluded because the ZTO channel layer in this study was encapsulated by the PMMA film. The first hole trapping model is unlikely to be responsible for this observation. The creation of electron and hole pairs via a band-to-band transition was not expected because the energy of photon used as a light source (2.48 eV) is lower than the band-gap energy (3.2 – 3.8 eV) of the ZTO films. Therefore, the Sn-concentration-dependent NBIS instability of the ZTO TFTs appears to be strongly related to the V_O related mechanism. The deep V_O defect can be excited to the ionized V_O^{2+} by the light exposure, which donates two free electrons in the conduction band of oxide semiconductor materials. This causes a negative V_{th} shift in the resulting devices even when the measurement was performed under the no illumination condition because of the very long recombination time of such photo-induced carriers [70]. The photo-conversion of V_O to V_O^{2+} will be proportional to the concentration of pre-existing V_O . The potential migration of V_O^{2+} toward the semiconductor/insulator interface due to the

applied NBS in the gate electrode also results in a negative V_{th} shift. As mentioned previously, the concentration of V_O in the ZTO film increased monotonously with increasing Sn-concentration. Therefore, the amplification of NBIS instability in the ZTO TFTs with increasing Sn-concentration, except for the case of the ZTO TFT with Sn/[Sn+Zn] ratio of 0.16, is consistent with the variation in the V_O concentration. The unexpected NBIS degradation ($\Delta V_{th} = -3.6$ V) of the device with Sn/[Sn+Zn] = 0.16 compared to that ($\Delta V_{th} = -2.4$ V) with Sn/[Sn+Zn] = 0.28 cannot be reconciled with its lower V_O density. This suggests that another degradation path exists. This singularity is presumably due to the accelerated migration of V_O^{2+} via the grain boundaries. The (002) columnar polycrystalline structure of the ZTO film with Sn/[Sn+Zn] = 0.16 would provide an effective and easy path for the migration of V_O^{2+} defects because the diffusion of point defects in the grain boundary of a poly-crystalline material is generally much faster than that in an amorphous material [123, 124]. Indeed, the grain boundary-assisted V_O^{2+} migration and the accelerated NBIS-induced V_{th} degradation was also reported previously in indium zinc oxide TFTs [125, 126].

In the Sn-rich ZTO film with a Sn/[Sn+Zn] ratio of 0.66, the migration of V_O^{2+} defects is also enhanced by the grain boundaries of the poly-crystalline material, which resulted in a huge negative V_{th} shift of -10.3 V in addition to the high V_O concentration. The best transistor performance including the mobility, N_{SS} and

I_{on}/I_{off} ratio was obtained for the device with $\text{Sn}/[\text{Sn}+\text{Zn}] = 0.48$, whereas the device with $\text{Sn}/[\text{Sn}+\text{Zn}] = 0.28$ exhibited the most stable behavior in terms of the NBIS stability. Therefore, the oxygen vacancy concentration and net carrier density in the ZTO thin film are the important key parameters for the compromise between the performance and photo-bias stability of the resulting TFTs. In addition, the ZTO channel layer with a discernible polycrystalline structure is undesirable for a photo-bias stable device even when it has a lower oxygen vacancy concentration.

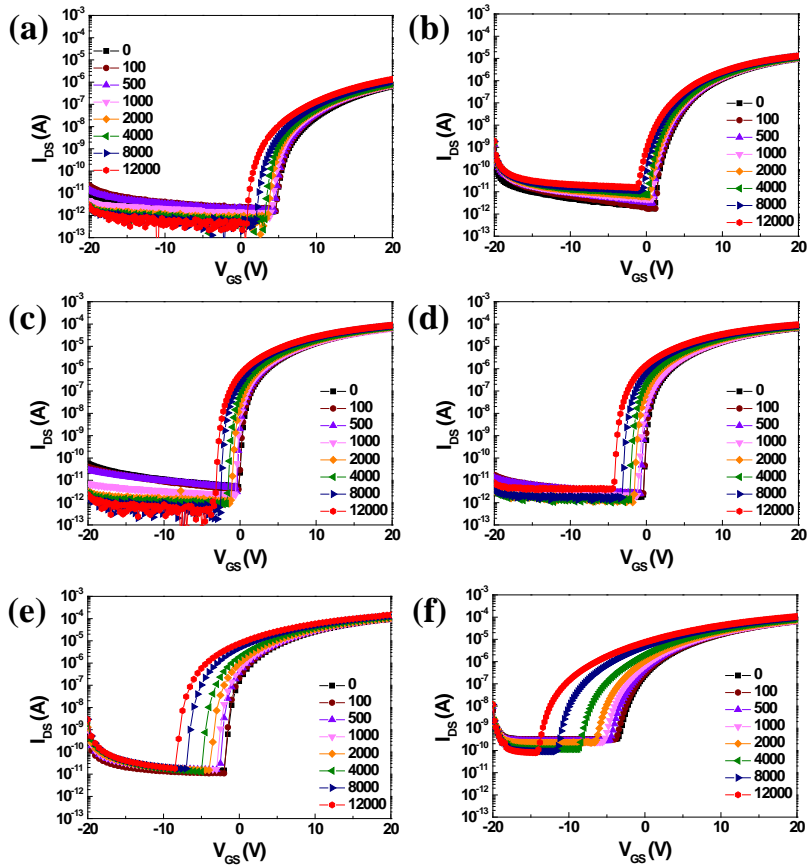


Fig. 4.20. Evolution of the transfer characteristics of ZTO TFTs with a Sn/[Zn+Sn] ratio of (a) 0.16, (b) 0.28, (c) 0.39, (d) 0.48, (e) 0.59 and (f) 0.66 as a function of the NBIS time.

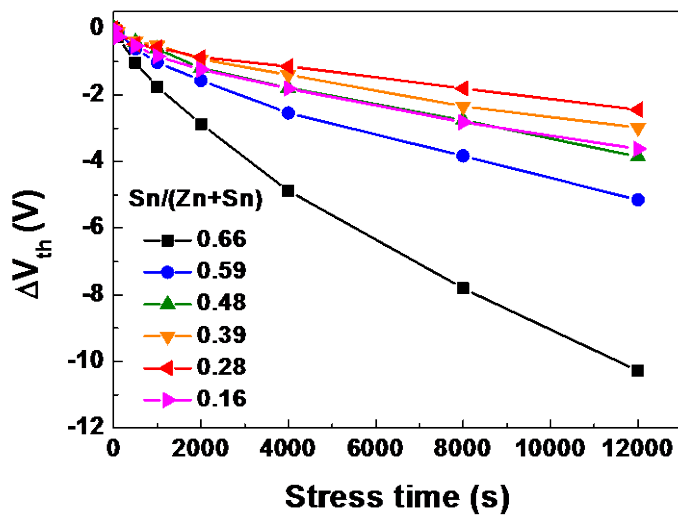


Fig. 4.21. Variation in V_{th} as a function of the NBIS time and (h) as a function of the incorporated Sn-concentration.

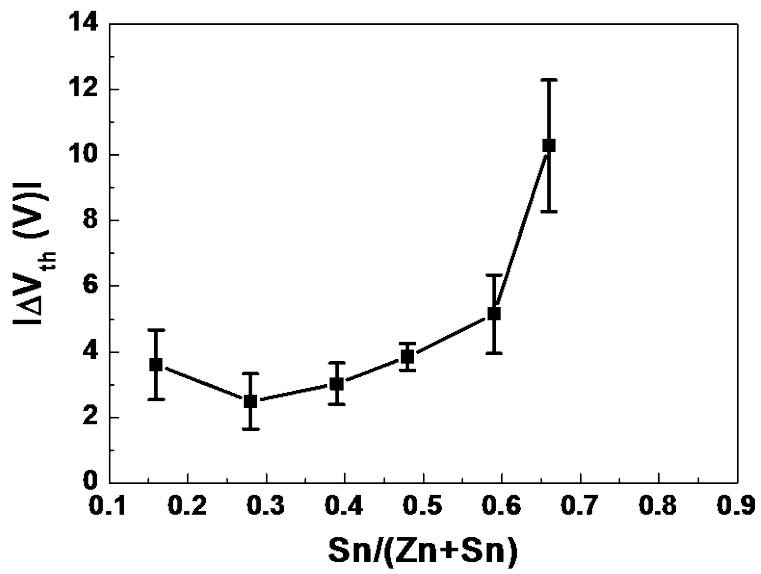


Fig. 4.22. Variation in V_{th} as a function of the incorporated Sn-concentration.

4.2.6. Summary

The structural, chemical and electrical properties of the solution-processed ZTO films were examined at different Sn-concentrations. The ZTO films with Sn/[Sn+Zn] ratios ranging from 0.28 to 0.48 exhibited an amorphous phase, whereas the Sn-deficient and excess ZTO films were in a polycrystalline phase with wurtzite and rutile structures, respectively. The V_O concentration and n_e values of the ZTO film increased monotonously with increasing Sn-concentration. The resulting carrier transport properties of the ZTO TFTs improved as the Sn/[Sn+Zn] ratio was increased to 0.48. The TFT with a Sn/[Sn+Zn] ratio of 0.48 exhibited a mobility, SS , V_{th} , and I_{on}/I_{off} of $4.25 \text{ cm}^2/\text{Vs}$, 0.42 V/decade , -0.02 V , and 4.10×10^7 , respectively. These values are generally inferior to the best performance reported for vacuum-processed TFTs with a ZTO channel layer and a similar Sn/[Sn+Zn] ratio, but still quite useful considering the inexpensive and simple process flow, which is critical for the economic production of large area flat panel displays. In addition, the trend of the variations in the device performance of solution-processed ZTO TFTs according to the Sn/[Sn+Zn] ratio is analogous to that of vacuum-processed devices, suggesting that the properties reported in this study are genuine to the material. The resistance under the NBIS condition was maximized for the device with Sn/[Sn+Zn] = 0.28, which was determined by both the lower V_O

concentration and amorphous phase of the ZTO films. The Sn-deficient and excess ZTO device suffered from a high negative V_{th} shift under NBIS conditions as well as inferior transport properties, which could be attributed to the large V_O concentration and/or polycrystalline phase nature.

5. Conclusions

The effect of the annealing temperature on the device performance and photo bias instability of solution-processed ZTO TFTs was studied. Device performance of the ZTO TFTs was improved by increasing the annealing temperature. The 500°C-annealed device exhibited a high μ_{FE} , low SS , V_{th} , and good $I_{on/off}$ ratio of 6.0 cm^2/Vs , 0.28 V/decade, 0.6 V, and 4.0×10^7 , respectively whereas the 300°C-annealed ZTO TFTs showed marginal performance: the μ_{FE} , SS , and $I_{on/off}$ ratio were 0.1 cm^2/Vs , 1.84 V/decade, and 3.1×10^5 , respectively. The dark NBS and NBIS instability for the ZTO TFTs depend strongly on the annealing temperature. The strong suppression of NBIS instability was also observed for the 500°C-annealed ZTO device. The ΔV_{th} of the 500°C-annealed ZTO device after the application of NBIS was reduced substantially from 10.5 V for the 300°C-annealed device to 2.9 V. The dynamics of V_{th} shift with NBS and NBIS time for all ZTO TFTs was analyzed based on the stretched exponential relaxation to improve the understanding of stress time-dependent charge trapping. The τ values extracted from the 300°C-annealed device under NBS and NBIS condition were 4.3×10^5 and 5.7×10^3 , respectively. In contrast, the 500°C-annealed device exhibited τ values of 9.0×10^6 and 1.1×10^5 , under NBS and NBIS condition, respectively. This improvement can be explained by the photo-created hole trapping model and

V_O transition model. In-depth analyses of the structural and chemical properties of ZTO films revealed that the purification and densification of the solution-processed ZTO channel layer are critical factors for high performance oxide TFTs with excellent photo-bias stability.

The structural, chemical and electrical properties of the solution-processed ZTO films were examined at different Sn-concentrations. The ZTO films with Sn/[Sn+Zn] ratios ranging from 0.28 to 0.48 exhibited an amorphous phase, whereas the Sn-deficient and excess ZTO films were in a polycrystalline phase with wurtzite and rutile structures, respectively. The V_O concentration and n_e values of the ZTO film increased monotonously with increasing Sn-concentration. The resulting carrier transport properties of the ZTO TFTs improved as the Sn/[Sn+Zn] ratio was increased to 0.48. The TFT with a Sn/[Sn+Zn] ratio of 0.48 exhibited a mobility, SS , V_{th} , and I_{on}/I_{off} of $4.25 \text{ cm}^2/\text{Vs}$, 0.42 V/decade , -0.02 V , and 4.10×10^7 , respectively. These values are generally inferior to the best performance reported for vacuum-processed TFTs with a ZTO channel layer and a similar Sn/[Sn+Zn] ratio, but still quite useful considering the inexpensive and simple process flow, which is critical for the economic production of large area flat panel displays. In addition, the trend of the variations in the device performance of solution-processed ZTO TFTs according to the Sn/[Sn+Zn] ratio is analogous to that of vacuum-processed devices, suggesting that the properties reported in this study are genuine

to the material. The resistance under the NBIS condition was maximized for the device with $\text{Sn}/[\text{Sn}+\text{Zn}] = 0.28$, which was determined by both the lower V_{O} concentration and amorphous phase of the ZTO films. The Sn-deficient and excess ZTO device suffered from a high negative V_{th} shift under NBIS conditions as well as inferior transport properties, which could be attributed to the large V_{O} concentration and/or polycrystalline phase nature.

From these results, the purification and densification of the solution-processed ZTO channel layer are critical factors for high performance oxide TFTs with excellent photo-bias stability. In addition, the optimal photo-bias stability of the ZTO TFTs was determined from the microstructure of the ZTO film rather than from the chemical defects of ZTO films.

Bibliography

- [1] K. Nomura, H. Ohta, A. Takagi, T. Kamiya, M. Hirano, H. Hosono, *Nature*, 432 488 (2004).
- [2] H. Chiang, J. Wager, R. Hoffman, J. Jeong, D.A. Keszler, *Appl. Phys. Lett.*, 86 013503 (2005).
- [3] C.G. Choi, S.J. Seo, B.S. Bae, *Electrochem. Solid-State Lett.*, 11 H7 (2008).
- [4] M.G. Kim, H.S. Kim, Y.G. Ha, J. He, M.G. Kanatzidis, A. Facchetti, T.J. Marks, *J. Am. Chem. Soc.*, 132 10352 (2010).
- [5] H. Hosono, *J. Non-Cryst. Solids*, 352 851 (2006).
- [6] H.Q. Chiang, PhD thesis, Oregon State University, (2007).
- [7] A. Chipman, *Nature*, 449 131 (2007).
- [8] E. Fortunato, P. Barquinha, R. Martins, *Adv. Mater.*, 24 2945 (2012).
- [9] D. Hong, G. Yerubandi, H. Chiang, M. Spiegelberg, J. Wager, *Crit. Rev. Solid State Mater. Sci.*, 33 101 (2008).
- [10] K. Nomura, T. Kamiya, H. Yanagi, E. Ikenaga, K. Yang, K. Kobayashi, M. Hirano, H. Hosono, *Appl. Phys. Lett.*, 92 202117 (2008).
- [11] D.K. Schroder, *Semiconductor material and device characterization*, John Wiley & Sons, 2006.
- [12] A. Ortiz-Conde, F.J. García-Sánchez, S. Malobabic, *Electron Devices*, IEEE

- Transactions on, 52 1669 (2005).
- [13] J.K. Jeong, J.H. Jeong, H.W. Yang, T.K. Ahn, M. Kim, K.S. Kim, B.S. Gu, H.J. Chung, J.S. Park, Y.G. Mo, *Journal of the Society for Information Display*, 17 95 (2009).
- [14] M. Ángeles Díaz-Díez, A. Macías-García, G. Silvero, R. Gordillo, R. Caruso, *Ceram. Int.*, 29 471 (2003).
- [15] C.J. Brinker, G.W. Scherer, *Sol-gel science: the physics and chemistry of sol-gel processing*, Gulf Professional Publishing, 1990.
- [16] C. Sanchez, J. Livage, M. Henry, F. Babonneau, *J. Non-Cryst. Solids*, 100 65 (1988).
- [17] C. Brinker, R. Sehgal, S. Hietala, R. Deshpande, D. Smith, D. Loy, C. Ashley, *Journal of Membrane Science*, 94 85 (1994).
- [18] J. Livage, M. Henry, C. Sanchez, *Prog. Solid State Chem.*, 18 259 (1988).
- [19] D. Mitzi, *Solution processing of inorganic materials*, John Wiley & Sons, 2008.
- [20] R.M. Pasquarelli, D.S. Ginley, R. O'Hayre, *Chem. Soc. Rev.*, 40 5406 (2011).
- [21] T. Kamiya, H. Hosono, *NPG Asia Materials*, 2 15 (2010).
- [22] K. Nomura, T. Kamiya, H. Ohta, K. Ueda, M. Hirano, H. Hosono, *Appl. Phys. Lett.*, 85 1993 (2004).
- [23] A. Takagi, K. Nomura, H. Ohta, H. Yanagi, T. Kamiya, M. Hirano, H. Hosono, *Thin Solid Films*, 486 38 (2005).

- [24] S. Masuda, K. Kitamura, Y. Okumura, S. Miyatake, H. Tabata, T. Kawai, J. Appl. Phys., 93 1624 (2003).
- [25] R. Hoffman, B.J. Norris, J. Wager, Appl. Phys. Lett., 82 733 (2003).
- [26] P. Carcia, R. McLean, M. Reilly, G. Nunes Jr, Appl. Phys. Lett., 82 1117 (2003).
- [27] E.M. Fortunato, P.M. Barquinha, A. Pimentel, A.M. Gonçalves, A.J. Marques, L.M. Pereira, R.F. Martins, Adv. Mater., 17 590 (2005).
- [28] L. Wang, M.-H. Yoon, G. Lu, Y. Yang, A. Facchetti, T.J. Marks, Nat. Mater., 5 893 (2006).
- [29] R. Presley, C. Munsee, C. Park, D. Hong, J. Wager, D. Keszler, J. Phys. D: Appl. Phys., 37 2810 (2004).
- [30] H. Yabuta, M. Sano, K. Abe, T. Aiba, T. Den, H. Kumomi, K. Nomura, T. Kamiya, H. Hosono, Appl. Phys. Lett., 89 (2006).
- [31] T. Iwasaki, N. Itagaki, T. Den, H. Kumomi, K. Nomura, T. Kamiya, H. Hosono, Appl. Phys. Lett., 90 242114 (2007).
- [32] N. Dehuff, E. Kettenring, D. Hong, H. Chiang, J. Wager, R. Hoffman, C.-H. Park, D. Keszler, J. Appl. Phys., 97 064505 (2005).
- [33] E. Fortunato, P. Barquinha, A. Pimentel, L. Pereira, G. Goncalves, R. Martins, *physica status solidi (RRL)*-Rapid Research Letters, 1 R34 (2007).
- [34] J.h. Lee, D.h. Kim, D.j. Yang, S.y. Hong, K.s. Yoon, P.s. Hong, C.o. Jeong, H.S.

- Park, S.Y. Kim, S.K. Lim, SID Symposium Digest of Technical Papers, Wiley Online Library, 2008, p. 625.
- [35] J.-S. Park, T.-W. Kim, D. Stryakhilev, J.-S. Lee, S.-G. An, Y.-S. Pyo, D.-B. Lee, Y.G. Mo, D.-U. Jin, H.K. Chung, *Appl. Phys. Lett.*, 95 013503 (2009).
- [36] S. Yu-Sheng, Z. Tian-Shu, *Sensors and Actuators B: Chemical*, 12 5 (1993).
- [37] D.L. Young, H. Moutinho, Y. Yan, T.J. Coutts, *J. Appl. Phys.*, 92 310 (2002).
- [38] T. Minami, T. Miyata, T. Yamamoto, *Surf. Coat. Technol.*, 108 583 (1998).
- [39] J. Lee, D.Y. Cho, J. Jung, U.K. Kim, S.H. Rha, C.S. Hwang, J.H. Choi, *Appl. Phys. Lett.*, 102 242111 (2013).
- [40] I. Kang, C.H. Park, E. Chong, S.Y. Lee, *Current Applied Physics*, 12 S12 (2012).
- [41] W. Jackson, R. Hoffman, G. Herman, *Appl. Phys. Lett.*, 87 193503 (2005).
- [42] D. Hong, H.Q. Chiang, R.E. Presley, N.L. Dehuff, J.P. Bender, C.-H. Park, J.F. Wager, D.A. Keszler, *Thin Solid Films*, 515 2717 (2006).
- [43] R. Hoffman, *Solid-state electronics*, 50 784 (2006).
- [44] B. Sun, H. Sirringhaus, *Nano Lett.*, 5 2408 (2005).
- [45] H. Faber, M. Burkhardt, A. Jedaa, D. Kälblein, H. Klauk, M. Halik, *Adv. Mater.*, 21 3099 (2009).
- [46] S. Jeong, J. Moon, *J. Mater. Chem.*, 22 1243 (2012).
- [47] Y. Ohya, T. Niwa, T. Ban, Y. Takahashi, *Japanese Journal of Applied Physics*,

- 40 297 (2001).
- [48] C.S. Li, Y.N. Li, Y.L. Wu, B.S. Ong, R.O. Loutfy, *J. Phys. D: Appl. Phys.*, 41 125102 (2008).
- [49] D.H. Lee, Y.J. Chang, G.S. Herman, C.H. Chang, *Adv. Mater.*, 19 843 (2007).
- [50] Y.-J. Chang, D.-H. Lee, G. Herman, C.-H. Chang, *Electrochem. Solid-State Lett.*, 10 H135 (2007).
- [51] G.H. Kim, B. Du Ahn, H.S. Shin, W.H. Jeong, H.J. Kim, H.J. Kim, *Appl. Phys. Lett.*, 94 (2009).
- [52] K.K. Banger, Y. Yamashita, K. Mori, R.L. Peterson, T. Leedham, J. Rickard, H. Sirringhaus, *Nat. Mater.*, 10 45 (2011).
- [53] T. Jun, K. Song, Y. Jeong, K. Woo, D. Kim, C. Bae, J. Moon, *J. Mater. Chem.*, 21 1102 (2011).
- [54] M.K. Ryu, K. Park, J.B. Seon, J. Park, I. Kee, Y. Lee, S.Y. Lee, *SID Symposium Digest of Technical Papers*, Wiley Online Library, 2009, p. 188.
- [55] J.K. Jeong, *Semicond. Sci. Technol.*, 26 034008 (2011).
- [56] J.S. Park, W.-J. Maeng, H.-S. Kim, J.-S. Park, *Thin Solid Films*, 520 1679 (2012).
- [57] R. Cross, M. De Souza, S. Deane, N. Young, *Electron Devices, IEEE Transactions on*, 55 1109 (2008).
- [58] A. Suresh, J. Muth, *Appl. Phys. Lett.*, 92 033502 (2008).

- [59] K. Nomura, T. Kamiya, M. Hirano, H. Hosono, *Appl. Phys. Lett.*, 95 013502 (2009).
- [60] J. Kyeong Jeong, H. Won Yang, J.H. Jeong, Y.-G. Mo, H.D. Kim, *Appl. Phys. Lett.*, 93 123508 (2008).
- [61] Y. Vygranenko, K. Wang, A. Nathan, *Appl. Phys. Lett.*, 91 263508 (2007).
- [62] K. Hoshino, D. Hong, H.Q. Chiang, J.F. Wager, *Electron Devices, IEEE Transactions on*, 56 1365 (2009).
- [63] S.G. Mathijssen, M. Cölle, H. Gomes, E.C. Smits, B. de Boer, I. McCulloch, P.A. Bobbert, D.M. de Leeuw, *Adv. Mater.*, 19 2785 (2007).
- [64] Y.-K. Moon, S. Lee, W.-S. Kim, B.-W. Kang, C.-O. Jeong, D.-H. Lee, J.-W. Park, *Appl. Phys. Lett.*, 95 013507 (2009).
- [65] J.-M. Lee, I.-T. Cho, J.-H. Lee, H.-I. Kwon, *Appl. Phys. Lett.*, 93 093504 (2008).
- [66] J.-H. Shin, J.-S. Lee, C.-S. Hwang, S.-H.K. Park, W.-S. Cheong, M. Ryu, C.-W. Byun, J.-I. Lee, H.Y. Chu, *Etri Journal*, 31 62 (2009).
- [67] J.K. Jeong, *J. Mater. Res.*, 28 2071 (2013).
- [68] K.H. Ji, J.I. Kim, Y.G. Mo, J.H. Jeong, S. Yang, C.S. Hwang, S.H.K. Park, M.K. Ryu, S.Y. Lee, J.K. Jeong, *IEEE Electron Device Lett.*, 31 1404 (2010).
- [69] J.H. Kim, U.K. Kim, Y.J. Chung, C.S. Hwang, *physica status solidi (RRL)-Rapid Research Letters*, 5 178 (2011).

- [70] K. Ghaffarzadeh, A. Nathan, J. Robertson, S. Kim, S. Jeon, C. Kim, U.-I. Chung, J.-H. Lee, *Appl. Phys. Lett.*, 97 143510 (2010).
- [71] M.D.H. Chowdhury, P. Migliorato, J. Jang, *Appl. Phys. Lett.*, 97 173506 (2010).
- [72] S. Yang, K.H. Ji, U.K. Kim, C.S. Hwang, S.H.K. Park, C.S. Hwang, J. Jang, J.K. Jeong, *Appl. Phys. Lett.*, 99 102103 (2011).
- [73] H. Oh, S.M. Yoon, M.K. Ryu, C.S. Hwang, S. Yang, S.H.K. Park, *Appl. Phys. Lett.*, 97 183502 (2010).
- [74] S. Yang, D.H. Cho, M.K. Ryu, S.H.K. Park, C.S. Hwang, J. Jang, J.K. Jeong, *Appl. Phys. Lett.*, 96 213511 (2010).
- [75] H.Q. Chiang, J.F. Wager, R.L. Hoffman, J. Jeong, D.A. Keszler, *Appl. Phys. Lett.*, 86 013503 (2005).
- [76] B.S. Yang, M.S. Huh, S. Oh, U.S. Lee, Y.J. Kim, M.S. Oh, J.K. Jeong, C.S. Hwang, H.J. Kim, *Appl. Phys. Lett.*, 98 122110 (2011).
- [77] J. Heo, S.B. Kim, R.G. Gordon, *Appl. Phys. Lett.*, 101 113507 (2012).
- [78] P. Gornn, P. Holzer, T. Riedl, W. Kowalsky, J. Wang, T. Weimann, P. Hinze, S. Kipp, *Appl. Phys. Lett.*, 90 063502 (2007).
- [79] K. Banger, Y. Yamashita, K. Mori, R. Peterson, T. Leedham, J. Rickard, H. Sirringhaus, *Nature materials*, 10 45 (2010).
- [80] S. Jeong, Y. Jeong, J. Moon, *J. Phys. Chem. C*, 112 11082 (2008).

- [81] Y.J. Chang, D.H. Lee, G.S. Herman, C.H. Chang, *Electrochem Solid St*, 10 H135 (2007).
- [82] S.J. Seo, C.G. Choi, Y.H. Hwang, B.S. Bae, *J. Phys. D: Appl. Phys.*, 42 035106 (2008).
- [83] S.K. Park, Y.H. Kim, H.S. Kim, J.I. Han, *Electrochem. Solid-State Lett.*, 12 H256 (2009).
- [84] Y. Jeong, K. Song, D. Kim, C.Y. Koo, J. Moon, *J Electrochem Soc*, 156 H808 (2009).
- [85] S.J. Seo, S. Yang, J.H. Ko, B.S. Bae, *Electrochem. Solid-State Lett.*, 14 H375 (2011).
- [86] S. Jeong, Y.G. Ha, J. Moon, A. Facchetti, T.J. Marks, *Adv. Mater.*, 22 1346 (2010).
- [87] S.T. Meyers, J.T. Anderson, C.M. Hung, J. Thompson, J.F. Wager, D.A. Keszler, *J. Am. Chem. Soc.*, 130 17603 (2008).
- [88] B.S. Ong, C. Li, Y. Li, Y. Wu, R. Loutfy, *J. Am. Chem. Soc.*, 129 2750 (2007).
- [89] Y. Zhao, L. Duan, G. Dong, D. Zhang, J. Qiao, L. Wang, Y. Qiu, *Langmuir*, 29 151 (2013).
- [90] D. Kovacheva, K. Petrov, *Solid State Ionics*, 109 327 (1998).
- [91] J.H. Jeong, H.W. Yang, J.S. Park, J.K. Jeong, Y.G. Mo, H.D. Kim, J. Song, C.S. Hwang, *Electrochem. Solid-State Lett.*, 11 H157 (2008).

- [92] Y.H. Kim, J.S. Heo, T.H. Kim, S. Park, M.H. Yoon, J. Kim, M.S. Oh, G.R. Yi, Y.Y. Noh, S.K. Park, *Nature*, 489 128 (2012).
- [93] D.W. Greve, *Field effect devices and applications : devices for portable, low-power, and imaging systems*, Prentice Hall, Upper Saddle River, NJ, 1998.
- [94] S.C. Deane, R.B. Wehrspohn, M.J. Powell, *Phys. Rev. B: Condens. Matter Mater. Phys.*, 58 12625 (1998).
- [95] K.H. Ji, J.I. Kim, H.Y. Jung, S.Y. Park, R. Choi, U.K. Kim, C.S. Hwang, D. Lee, H. Hwang, J.K. Jeong, *Appl. Phys. Lett.*, 98 103509 (2011).
- [96] A. Janotti, C.G. Van de Walle, *Rep. Prog. Phys.*, 72 126501 (2009).
- [97] J.Y. Kwon, K.S. Son, J.S. Jung, K.H. Lee, J.S. Park, T.S. Kim, K.H. Ji, R. Choi, J.K. Jeong, B. Koo, *Electrochem. Solid-State Lett.*, 13 H213 (2010).
- [98] Y. Jeong, C. Bae, D. Kim, K. Song, K. Woo, H. Shin, G. Cao, J. Moon, *ACS Appl. Mater. Interfaces*, 2 611 (2010).
- [99] Y.S. Rim, W.H. Jeong, D.L. Kim, H.S. Lim, K.M. Kim, H.J. Kim, *J. Mater. Chem.*, 22 12491 (2012).
- [100] H. Yabuta, M. Sano, K. Abe, T. Aiba, T. Den, H. Kumomi, K. Nomura, T. Kamiya, H. Hosono, *Appl. Phys. Lett.*, 89 112123 (2006).
- [101] A. Suresh, P. Wellenius, A. Dhawan, J. Muth, *Appl. Phys. Lett.*, 90 123512 (2007).
- [102] D.H. Levy, S.F. Nelson, D. Freeman, *J. Display Technol.*, 5 484 (2009).

- [103] K. Banger, Y. Yamashita, K. Mori, R. Peterson, T. Leedham, J. Rickard, H. Siringhaus, *Nat. Mater.*, 10 45 (2010).
- [104] M.G. Kim, M.G. Kanatzidis, A. Facchetti, T.J. Marks, *Nat. Mater.*, 10 382 (2011).
- [105] T. Kamiya, K. Nomura, H. Hosono, *Sci. Technol. Adv. Mater.*, 11 044305 (2010).
- [106] T. Kamiya, K. Nomura, H. Hosono, *J. Display Technol.*, 5 468 (2009).
- [107] D. Kim, C.Y. Koo, K. Song, Y. Jeong, J. Moon, *Appl. Phys. Lett.*, 95 103501 (2009).
- [108] B.S. Yang, M.S. Huh, S. Oh, U.S. Lee, Y.J. Kim, M.S. Oh, J.K. Jeong, C.S. Hwang, H.J. Kim, *Appl. Phys. Lett.*, 98 122110 (2011).
- [109] U.K. Kim, S.H. Rha, J.H. Kim, Y.J. Chung, J. Jung, E.S. Hwang, J. Lee, T.J. Park, J.-H. Choi, C.S. Hwang, *J. Mater. Chem. C*, 1 6695 (2013).
- [110] Y.J. Chang, D.H. Lee, G.S. Herman, C.H. Chang, *Electrochem. Solid-State Lett.*, 10 H135 (2007).
- [111] P. Görrn, P. Hölzer, T. Riedl, W. Kowalsky, J. Wang, T. Weimann, P. Hinze, S. Kipp, *Appl. Phys. Lett.*, 90 063502 (2007).
- [112] Y.-H. Kim, J.-I. Han, S.K. Park, *IEEE Electron Device Lett.*, 33 50 (2012).
- [113] S.K. Park, Y.-H. Kim, H.-S. Kim, J.-I. Han, *Electrochem. Solid-State Lett.*, 12 H256 (2009).

- [114] M.K. Ryu, S. Yang, S.H.K. Park, C.S. Hwang, J.K. Jeong, *Appl. Phys. Lett.*, 95 173508 (2009).
- [115] Ü. Özgür, Y.I. Alivov, C. Liu, A. Teke, M.A. Reshchikov, S. Doğan, V. Avrutin, S.-J. Cho, H. Morkoç, *J. Appl. Phys.*, 98 041301 (2005).
- [116] R. Jenkins, R. Snyder, *Introduction to X-ray Powder Diffractometry*, John Wiley & Sons, 2012.
- [117] M.G. Kim, H.S. Kim, Y.G. Ha, J. He, M.G. Kanatzidis, A. Facchetti, T.J. Marks, *J. Am. Chem. Soc.*, 132 10352 (2010).
- [118] C. Kilic, A. Zunger, *Phys. Rev. Lett.*, 88 095501 (2002).
- [119] J.Y. Noh, H. Kim, H.H. Nahm, Y.S. Kim, D.H. Kim, B.D. Ahn, J.H. Lim, G.H. Kim, J.H. Lee, J. Song, *J. Appl. Phys.*, 113 183706 (2013).
- [120] B.S. Yang, S. Park, S. Oh, Y.J. Kim, J.K. Jeong, C.S. Hwang, H.J. Kim, *J. Mater. Chem.*, 22 10994 (2012).
- [121] P. Ágoston, K. Albe, R.M. Nieminen, M.J. Puska, *Phys. Rev. Lett.*, 103 245501 (2009).
- [122] P. Anderson, *Phys. Rev. Lett.*, 34 953 (1975).
- [123] M. Cao, P.V. Voorde, M. Cox, W. Greene, *IEEE Electron Device Lett.*, 19 291 (1998).
- [124] B.L. Doyle, P.S. Peercy, J.D. Wiley, J.H. Perepezko, J.E. Nordman, *J. Appl. Phys.*, 53 6186 (1982).

- [125] S. Oh, B.S. Yang, Y.J. Kim, Y.J. Choi, U.K. Kim, S.J. Han, H.W. Lee, H.J. Kim, S. Kim, J.K. Jeong, *J. Phys. D: Appl. Phys.*, 47 165103 (2014).
- [126] S. Oh, B.S. Yang, Y.J. Kim, M.S. Oh, M. Jang, H. Yang, J.K. Jeong, C.S. Hwang, H.J. Kim, *Appl. Phys. Lett.*, 101 092107 (2012).

List of publication

1. Journals (SCI)

1. Bong Seob Yang, Myung Soo Huh, Seungha Oh, Ung Soo Lee, **Yoon Jang Kim**, Myeong Sook Oh, Jae Kyeong Jeong, Cheol Seong Hwang, and Hyeong Joon Kim, "Role of ZrO₂ incorporation in the suppression of negative bias illumination-induced instability in Zn-Sn-O thin film transistors", *Appl. Phys. Lett.* 98, 122110 (2011).
2. Myeong Sook Oh, Myung Soo Huh, Bong Seob Yang, Jong Ho Lee, Seong Ha Oh, Ung Soo Lee, **Yoon Jang Kim**, and Hyeong Joon Kim, "Improvement of electrical and optical properties of molybdenum oxide thin films by ultralow pressure sputtering method", *J. Vac. Sci. Technol. A* 30(3), 031501 (2012).
3. Bong Seob Yang, Sanghyun Park, Seungha Oh, **Yoon Jang Kim**, Jae Kyeong Jeong, Cheol Seong Hwang and Hyeong Joon Kim, "Improvement of the photo-bias stability of the Zn-Sn-O field effect transistors by an ozone treatment", *J. Mater. Chem.*, 22, 10994-10998 (2012).
4. Seungha Oh, Bong Seob Yang, **Yoon Jang Kim**, Myeong Sook Oh, Mi Jang, Hoichang Yang, Jae Kyeong Jeong, Cheol Seong Hwang, and Hyeong Joon Kim, "Anomalous behavior of negative bias illumination stress instability in an indium zinc oxide transistor: a cation combinatorial approach", *Appl. Phys. Lett.*, 101, 092107 (2012)
5. **Yoon Jang Kim**, Bong Seob Yang, Seungha Oh, Sang Jin Han, Hong Woo Lee, Jaeyeong Heo, Jae Kyeong Jeong, and Hyeong Joon Kim, "Photobias Instability

- of High Performance Solution Processed Amorphous Zinc Tin Oxide Transistors”, *ACS Appl. Mater. Interfaces*, 5, 3255–3261 (2013)
6. Bong Seob Yang, Seungha Oh, **Yoon Jang Kim**, Sang Jin Han, Hong Woo Lee, Hyuk Jin Kim, Hui Kyung Park, Jae Kyeong Jeong, Jaeyeong Heo, Cheol Seong Hwang, and Hyeong Joon Kim, “Effect of sputter power on the photobias stability of zinc-tin-oxide field-effect transistors”, *J. Vac. Sci. Technol.*, B 32, 011202 (2014)
 7. Seungha Oh, Bong Seob Yang, **Yoon Jang Kim**, Un Ki Kim, Sang Jin Han, Hong Woo Lee, Hyuk Jin Kim, Sung Min Kim, Jae Kyeong Jeong, and Hyeong Joon Kim, “Dynamics of negative bias thermal stress-induced threshold voltage shifts in indium zinc oxide transistors: impact of the crystalline structure on the activation energy barrier”, *J. Phys. D: Appl. Phys.*, 47 165103 (2014)
 8. Bong Seob Yang, Seungha Oh, **Yoon Jang Kim**, Sang Jin Han, Hong Woo Lee, Hyuk Jin Kim, Sungmin Kim, Hui Kyung Park, Jaeyeong Heo, Jae Kyeong Jeong, and Hyeong Joon Kim, “The Anomalous Effect of Oxygen Ratio on the Mobility and Photobias Stability of Sputtered Zinc–Tin–Oxide Transistors”, *IEEE Trans. Electron Devices*, 61 2071 (2014)
 9. **Yoon Jang Kim**, Seungha Oh, Bong Seob Yang, Sang Jin Han, Hong Woo Lee, Hyuk Jin Kim, Jae Kyeong Jeong, Cheol Seong Hwang, and Hyeong Joon Kim, “Impact of the cation composition on the electrical performance of solution-processed zinc tin oxide thin film transistors”, *ACS Appl. Mater. Interfaces*, (2014), (submitted)
 10. Hong Woo Lee, Bong Seob Yang, **Yoon Jang Kim**, Seungha Oh, Jong Hwan Lee, Jae Kyeong Jeong, and Hyeong Joon Kim, “Comprehensive studies on the

carrier transporting property and photo-bias instability of sputtered zinc tin oxide thin film transistors”, *IEEE Trans. Electron Devices*, (2014), (accepted)

2. Proceeding

1. Seungha Oh, Bong Seob Yang, **Yoon Jang Kim**, and Hyeong Joon Kim, “Composition Dependence of the Negative Bias Light Illumination Instability of Indium Zinc Oxide Transistors”, ECS 222nd Meeting, 7-12 October 2012, Honolulu, Hawaii.
2. Bong Seob Yang, Seungha Oh, **Yoon Jang Kim**, and Hyeong Joon Kim, “Improvement of the photo-bias stability of the Zn-Sn-O field effect transistors by an ozone treatment”, ECS 222nd Meeting, 7-12 October 2012, Honolulu, Hawaii.

3. Conferences

3.1 International

1. **Yoon Jang Kim**, Bong Seob Yang, Seungha Oh, Jae Kyeong Jeong, Hyeong Joon Kim, “Effect of Annealing Temperature on the Electrical Characteristics of Solution Processed Zinc Tin Oxide Thin Film Transistors” Electrochemical Society 221th Meeting, 6-11 May 2012, Seattle, USA.
2. Seungha Oh, Bong Seob Yang, **Yoon Jang Kim**, and Hyeong Joon Kim, “Composition Dependence of the Negative Bias Light Illumination Instability of Indium Zinc Oxide Transistors”, Electrochemical Society 222th Meeting, 7-12 October 2012, Honolulu, Hawaii.

3. Bong Seob Yang, Seungha Oh, **Yoon Jang Kim**, and Hyeong Joon Kim, “Improvement of the photo-bias stability of the Zn-Sn-O field effect transistors by an ozone treatment”, Electrochemical Society 222th Meeting, 7-12 October 2012, Honolulu, Hawaii.
4. **Yoon Jang Kim**, Bong Seob Yang, Jong Ho Lee, Seungha Oh, Sang Jin Han, Hong Woo Lee, Jae Kyeong Jeong and Hyeong Joon Kim, “Negative bias illumination stress instability of solution processed amorphous zinc tin oxide transistors”, Latin Display 2012/IDRC 2012, 26-30 November 2012, Sao Paulo, Brazil.
5. Seungha Oh, Bong Seob Yang, **Yoon Jang Kim**, Sang Jin Han, Hong Woo Lee, Hyuk Jin Kim, and Hyeong Joon Kim, “Analysis for the hole migration behavior in InZnO thin film transistors using a stretched exponential fitting method”, Material Research Society, 6-6 December 2012, Boston, USA.
6. **Yoon Jang Kim**, Bong Seob Yang, Seungha Oh, Hyuk Jin Kim, and Hyeong Joon Kim, “Photo-bias Instability of Solution Processed Zinc Tin Oxide Thin Film Transistors with Varying Zn:Sn Composition Ratio”, International Conference on Small Science, 15-18 December 2013, Las Vegas, USA.

3.2 Domestic

1. **Yoon Jang Kim**, Sang Jin Han, Seungha Oh, and Hyeong Joon Kim, “Effect of annealing temperature on the electrical characteristics of solution processed zinc tin oxide thin film transistors”, The 3rd Semiconductor and Display Jeju Forum, 10-11 May 2013, Jeju Nat’l Univ., Korea.

Abstract (in Korean)

ZnO를 기반으로 하는 산화물 반도체는 비정질 실리콘에 비해 높은 이동도와 투명도를 가지며, 저온 공정에서 제작이 가능하여 AMLCDs (active matrix liquid crystal displays) 또는 OLEDs (organic light-emitting diodes)와 같은 디스플레이 제품의 구동 소자로써 각광을 받고 있다. 최근에는 이러한 산화물 반도체를 제작하는 공정으로 기존에 사용되던 vacuum 기반의 공정을 대신하여 공정이 단순하고 낮은 비용과 높은 생산성을 갖는 용액공정을 이용하여 제작된 산화물 반도체도 보고되고 있다. 하지만, 빛과 gate 전압 stress에 의한 소자의 열화문제는 산화물 반도체의 상용화에 걸림돌로 작용하고 있으며 용액 공정을 이용한 Zinc Tin Oxide (ZTO) 박막트랜지스터의 경우 박막의 열처리 온도 및 Sn 조성이 광 전압 신뢰성에 미치는 영향에 대한 연구가 부족한 상황이다.

이 논문에서는 용액 공정을 이용하여 제작된 ZTO 박막의 열처리온도와 Sn 농도에 의한 다양한 물리적 특성들과 ZTO TFT의 이동특성 및 광 전압 신뢰성에 대한 영향에 대한 연구를 진행하였다.

첫째로, 용액 공정을 이용하여 우수한 특성을 나타내는 Zinc Tin Oxide 트랜지스터를 제작하였다. 제작된 ZTO 채널내의 산소 공공 결합의 밀도는 열처리 온도가 증가함에 따라 감소하였지만 박막의 밀도와 순

도는 증가하였다. 이러한 결과로, 용액 공정을 이용하여 제작된 ZTO 트랜지스터의 소자 특성은 열처리 온도가 증가함에 따라 향상되었다. Negative bias stress (NBS)와 negative bias illumination stress (NBIS)에서 V_{th} 의 변화는 열처리 온도에 크게 영향을 받았으며, 열처리 온도가 증가함에 따라 감소하였다. 전하 트랩의 메커니즘을 확인하기 위하여, stretched exponential relaxation을 의거하여 모든 ZTO 트랜지스터에 대한 NBS와 NBIS의 V_{th} 변화를 분석하였다. 각각의 트랜지스터의 V_{th} 이동은 NBS에 비해 NBIS에서 더욱 증가하였고, 그 결과 더 작은 relaxation 시간과 더 큰 dispersion parameter를 보였다. 이러한 특성의 향상은 열처리 온도가 증가함에 따라 산소 공공의 농도가 감소하였기 때문으로 산소 공공의 이동모델과 빛에 의해 생성된 정공의 trapping 모델로 설명될 수 있다. 이러한 결과로부터 용액 공정을 이용한 ZTO 채널의 순도와 치밀화가 우수한 광 신뢰성 특성을 가진 높은 성능의 산화물 반도체를 얻기 위한 중요한 인자임을 확인하였다.

다음으로 용액 공정을 이용한 ZTO 박막의 Sn/[Zn+ Sn] 비율에 따라 화학적 그리고 전기적 특성의 변화에 대하여 연구하였다. Zn의 비율이 높은 ZTO 박막의 경우 다결정질의 wurtzite 구조를 가지고 있으며, Sn은 shallow donor임을 확인하였다. 반면, Sn의 비율이 높은 ZTO 박막의 경우 rutile 결정구조를 가지고 있으며, Zn 원자가 Sn 자리를 치환하여 acceptor로 작용할 것으로 추정된다. Sn/[Zn+ Sn]의 비율이 0.28에서

0.48까지의 중간조성에서의 ZTO 박막의 경우 450도에서 열처리를 했음에도 비정질 구조를 가지고 있는 것이 확인되었다.

마지막으로, 다양한 Sn 조성비를 갖는 ZTO 트랜지스터의 전기적 특성과 광 전압 신뢰성을 평가하였다. Sn/[Zn+ Sn] 비율이 0.48인 조성의 ZTO 트랜지스터에서 최적의 이동특성을 확인하였다. 이와는 반대로, 이보다 더 높거나 낮은 Sn 의 농도를 가진 ZTO 트랜지스터의 경우 소자 특성은 낮은 이동도와 높은 off 전류특성을 나타내었다. ZTO 트랜지스터의 광 전압 신뢰성은 산소 공공의 농도가 감소할수록 향상되었으며 비정질 구조에서 가장 우수한 특성을 나타내었다. 이러한 결과로부터 빛에 의해 여기되어 +2의 전하를 갖는 산소 공공의 결정립계를 통한 이동이 ZTO 트랜지스터의 광 전압 신뢰성에 큰 영향을 끼치며 비정질 구조를 갖는 조성의 ZTO 트랜지스터가 더욱 우수한 광 전압 신뢰성 특성을 나타낼 수 있음을 확인하였다.

Keywords : Solution process, Zinc Tin Oxide (ZTO), thin film transistors (TFTs), annealing temperature, cation composition, photo-bias stability, Negative bias illumination stability (NBIS)

Student ID : 2010-30959

Yoon Jang Kim